STRUCTURE AND IN SITU STRESS ANALYSIS OF THE TAZHONG UPLIFT, NW CHINA: IMPLICATIONS FOR FAULT REACTIVATION

A Thesis

by

ELIZABETH DA SILVA RODRIGUEZ

Submitted to the Office of Graduate and Professional Studies of
Texas A&M University
in partial fulfillment of the requirements for the degree of

MASTER OF SCIENCE

Chair of Committee,	Frederick M. Chester
Committee Members,	Nicholas D. Perez
	Ding Zhu
Head of Department,	Michael Pope

August 2018

Major Subject: Geophysics

ABSTRACT

The Tarim Basin in northwest China is an intracratonic, poly-phase basin with a subsurface structure that records a protracted tectonic history associated with crustal accretion and amalgamation. Currently, the basin is bounded by actively deforming mountain belts but displays little evidence of active deformation within the basin. Here, detailed interpretation of 3D seismic reflection data and analysis of drilling-induced deformation in deep boreholes (e.g. borehole breakouts) are used to resolve uncertainties about the timing and distribution of past deformation, the effect of pre-existing structures on subsequent deformation, and the current in situ stress state in the Tazhong Uplift of the Central Tarim Basin. The geometry and kinematics of Ordovician thrust faults and folds, Silurian-Permian strike-slip faults, and Triassic igneous bodies and normal faults, along with stratigraphic relationships, suggest that creation of new faults, and reactivation of pre-existing faults occurred during tectonic events in the Paleozoic and Early Mesozoic; however, no evidence of faulting is observed in Late Mesozoic or Cenozoic strata in the Tazhong Uplift. The current in situ stress should favor extensional and strike-slip tectonics with maximum horizontal compression directed NE, which contrasts with past stress states in the basin inferred from Paleozoic and Mesozoic structures. In situ differential stress magnitude in the Tazhong Uplift (ranging from 94 to 170 MPa) is insufficient to reactivate the most optimally-oriented faults in the Central Tarim Basin, even though the basin is bounded by the active Tian Shan and Kunlun Shan thrust belts to the north- and south-west, and the left-lateral strike-slip Altyn Tagh fault to the south, all associated with the ongoing Himalayan-Tibetan orogeny. The low differential stress may be understood if the basin-bounding faults (particularly the Altyn Tagh fault) operate at low absolute shear stress, similar to continental transform faults such as the San Andreas fault, CA.

DEDICATION

To Lucy, Melita, and Rebe for their constant support, encouragement, and inspiration. You are my role model.

ACKNOWLEDGEMENTS

I would like to thank China National Petroleum Corporation for supporting my education and for providing the data set for this thesis.

Thanks to Dr. Chester for his constant guidance and support over the last two years. I would like to thank my committee members Dr. Zhu and Dr. Perez for their insights, recommendations, and guidance throughout the course of this research.

Thanks to all my professors in the Department of Geology and Geophysics.

Thanks to Wenyu Zhang, Charles Neal, Lennon Infante, Javier Tellez, and Shayna Quidas for their technical support and guidance.

Thanks to my dear friends, colleagues, and the department staff for making my time at Texas A&M University a great experience.

Finally, thanks to my family for their encouragement throughout the pursuit of my Master's degree.

CONTRIBUTORS AND FUNDING SOURCES

Contributors

This project was supervised by a thesis committee consisting of Dr. Frederick Chester, and Dr. Nicholas Perez of the Department of Geology and Geophysics and Dr. Ding Zhu of the Department of Petroleum Engineering. The data analyzed in this investigation was provided by China National Petroleum Corporation (CNPC). All work for the thesis was completed independently by the student.

Funding Sources

Graduate study was supported by CNPC and the Department of Geology and Geophysics at Texas A&M University.

NOMENCLATURE

MD	Measured Depth
TVDSS	True Vertical Depth Sub-Sea level
DITF	Drilling Induced Tensile Fracture
FMI	Formation MicroImager
UCS	Unconfined Compressive Strength

TABLE OF CONTENTS

Page

LIST OF FIGURES

LIST OF TABLES

Page

INTRODUCTION

Pre-existing structures play a fundamental role in shaping subsequent deformational events and it is critical to understand their influence on the tectonic evolution of a basin. Pre-existing structures influence the reactivation, location, and deformation style of the lithosphere in diverse tectonic settings especially intracontinental and continental margins, rift basins, and strike-slip settings (Rutter et al., 2001).

The nature, relevance, and mechanical drivers for tectonic reactivation have been widely studied in diverse tectonic settings. Studies have proposed that inherited structural geometry, lithological heterogeneity, stress magnitudes and orientations, and rock strength are controlling factors on both successive fault propagation and fault kinematics (Ghisetti and Vezzanni, 2005; Lunn, 2008). Fault scale, orientation, and interconnectivity as well as fluid influx, crustal depths, and intensity of localized strain in faults largely govern the distribution of later displacement (Rutter et al., 2001). Furthermore, pre-existing basin geometry and fault reactivation appear to have a long-term influence on lithospheric stability, sedimentation, mineralization, earthquake rupture, subsequent deformation style and distribution, and hydrocarbon migration and accumulation.

Within the seismogenic zone, intracontinental deformation is largely accommodated by the reactivation of existing faults (Sibson, 1980; Sibson, 1985). Structural reactivation is the modification of pre-existing features by a younger episode of deformation occurring in the proximity or along the same plane of the existing structure (Rutter et al., 2001). Frictional reactivation will occur when the ratio of the shear to effective normal stress exceeds the material

property μ, known as the coefficient of sliding friction, as presented by Amonton's Law (Jaeger et al., 2009):

$$\tau = \mu(\sigma_n - P_f) \quad (1)$$

Where τ is the shear stress, σ_n is the normal stress, and P_f is the pore fluid pressure. The conditions for frictional sliding suggest that seismogenic failure will likely occur when the shear stress increases (thereby reaching a critical value as a result of elastic strain accumulation), when the normal effective stress decreases, or by an increase in fluid pressure that results in a reduction of the normal effective stress (Sibson, 1985). The stability of pre-existing faults, governed by (1), depends on the interplay of the stress field and the orientation of existing planes of weakness (Sibson, 1980; Sibson, 1985).

Although it is recognized that intracontinental deformation via reactivation of existing structures is more common than the creation of new structures (Sibson, 1985), fault reactivation does not always occur (Rutter et al., 2001). Many authors have suggested that fault reactivation is a first order control on basin evolution (Ghisetti and Vezzanni, 2005; Pizzi and Galadini, 2009); however, others question the absolute presence and influence of tectonic inheritance (Butler, 1989). For example, the control of inherited Pre-Quaternary basin structures on the segmentation of Quaternary normal faults in the Apennines (Italy) has been widely studied (Pizzi and Galadini, 2009). A motivation of this investigation was to analyze large magnitude earthquake ruptures and the paleoseismological record in the area. Analysis of pre-existing structures observed in seismic data, in combination with seismological data, supports the hypothesis that the size of pre-existing cross-structures control fault reactivation and segmentation in the north-central Apennines (Pizzi and Galadini, 2009).

The inherited structural influence of normal faults in actively extending rifts has been studied in Pleistocene sedimentary cover structures in the Gulf of Corinth, Greece (Ghisetti and Vezzanni, 2005). The geometry and kinematic behavior of faults, distribution of detachment horizons, and plate motion rates, suggest that active basement faults control deformation in the sedimentary basin (Ghisetti and Vezzanni, 2005). Similarly, analysis of the nature and control of pre-existing normal faults on subsequent thrust systems in the Western Alps indicate limited reactivation of normal faults in the region (Butler et al., 1989). Fault reactivation continues to be a debated topic, and well-defined geological and geophysical evidence is needed to conclusively determine if reactivation of structures has occurred and if propensity for fault reactivation exists within a basin.

Although many studies have focused on understanding tectonic rejuvenation in a myriad of basins, further analysis is required to describe the interaction between the in situ stress states and the potential for fault reactivation in the Central Tarim Basin. Western China is composed of a series of distinctive intra-plate sedimentary basins that have experienced a discrete continental accretion and deformation history. In general, these basins are surrounded by actively deforming tectonic belts but their interiors are relatively undeformed (Carroll et al., 2010). Located between the Tian Shan mountain belt and the Tibetan Plateau, the Tarim Basin is a massive intracratonic poly-phase basin spanning more than 560,000 km^2 of northwest China (Figure 1). The Tarim Basin evolved into its present-day configuration after the Indo-Asian collision and is currently bounded by three active orogenic belts: The Altyn mountains to the southeast, the Kunlun fold belt to the southwest, and the Tian Shan mountain range to the north (Figure 1) (Jia et al., 1998; Li et al., 2012).

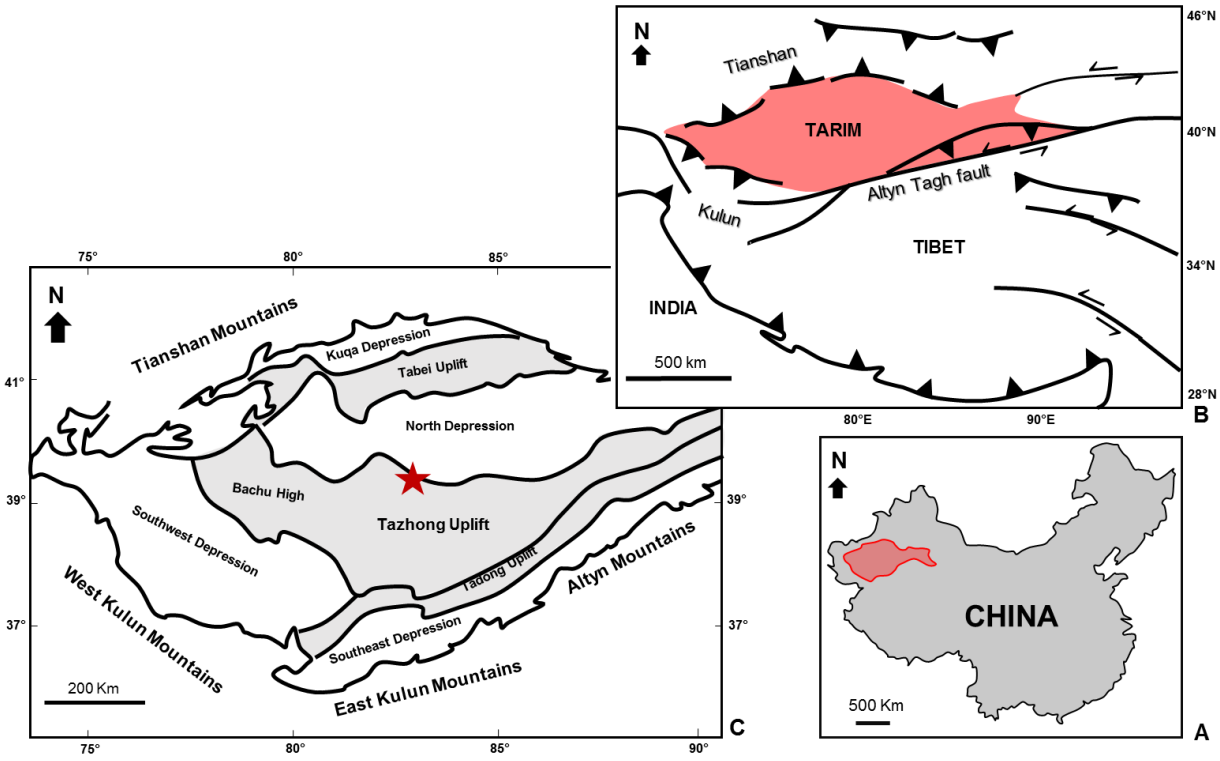

Figure 1: Location of the study area. **A**-Map of China showing the location of the Tarim Basin. **B**-Simplified map of the Tarim Basin and Tibetan Plateau showing active faults systems including the Altyn Tagh fault. areas. **C**- Tectonic map of the Tarim Basin showing main uplifts and depocenters. The red star indicates the location of the study area situated in the northern slope of the Tazhong Uplift.

In accordance with the current stress field, associated with Himalayan-Tibetean orogenesis, the peripheries of Tarim Basin are seismically active regions dominated by large intracontinental reverse and strike-slip fault zones such as the Altyn Tagh left-lateral strike-slip fault (Figure 2). Thus, it is expected that the current in situ stresses in the interior of the basin would also be controlled by regional contractional deformation; however, only minor deformation is occurring in the interior of the basin (Figure 2). Despite the presence of large Paleozoic and Triassic fault systems in the Central Tarim Basin and protracted tectonic activity along the basin's boundaries, there has not been significant reactivation or formation of new structures during the Cenozoic

(Allen et al., 1999; Yang and Liu, 2002; Carroll et al., 2010). This raises the question why the Central Tarim Basin remains tectonically stable despite the presence of major fault zones in the basin interior.

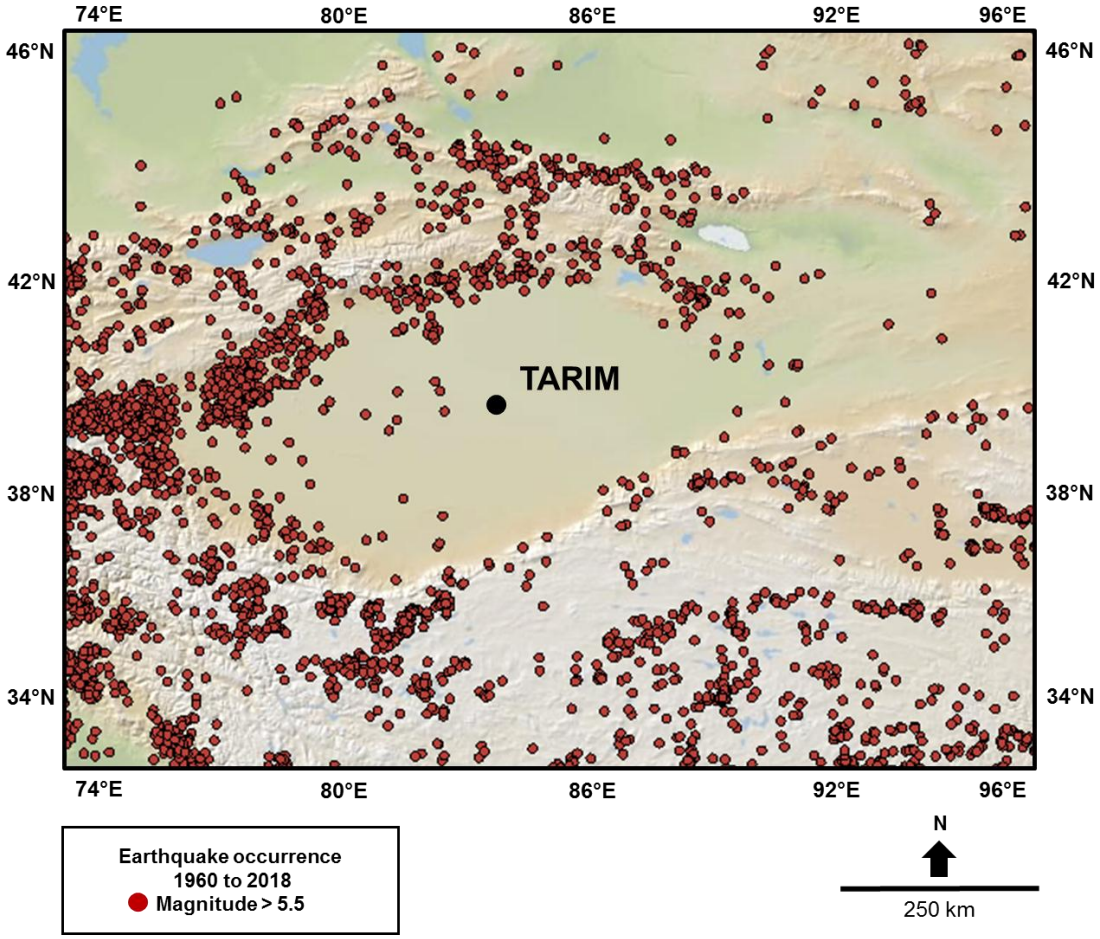

Figure 2: Seismicity map of northwest China spanning the Tarim Basin and marginal orogenic belts. The map displays earthquake epicenters and magnitudes (red circles) recorded from 1960 to 2018 (data base).

The Tarim Basin has experienced a multistage deformation history involving the formation and reactivation of crustal-scale fault systems associated with regional tectonic activity (Li et al.,

2012; Lan et al., 2014; Han et al., 2017). Four major deformation phases (Late Proterozoic to Early Ordovician, Middle to Late Ordovician, Silurian to Permian, Mesozoic to Cenozoic) influenced the depositional and structural evolution of the Tarim Basin since the Sinian (Neoproterozoic). Divergence during the Late Proterozoic and subsequent convergence in the Paleozoic and Cenozoic led to the formation of four depocenters: the Kuqa depression, the North Depression, and the Southwest and Southeast Depressions and three uplifts: the Kalpin Uplfit, the Tabei Uplift, and the Central Uplift, which can be further subdivided in the Bachu Uplift and the Tazhong Uplift (Figure 1; Li et al., 2012). These events represent the episodes of continent growth through subduction and collision with other plates, moving the Tarim block from a margin to a plate interior. The protracted collision between India and Asia began approximately 50-55 Ma ago, uplifted the Himalayan-Tibetan Plateau and developed thrust fault belts and marginal fault systems in the Tian Shan, Kunlun Shan, and Altyn Shan (DeCelles et al., 1998; Allen et al., 1999; Yang and Liu, 2002; Geherls et al., 2003). The Tarim Basin evolved into a complex arrangement of foreland basins where orogenic growth and rapid rates of shortening drove subsidence in the northern and southern boundaries of the Tarim Basin (Yang and Liu, 2002). Current tectonic activity along the margins of the Tarim Basin include seismicity, thin-skinned thrust belts, uplifted terraces and other geomorphological features, yet the central portion of the Tarim Basin is largely aseismic (Figure 2; Allen et al., 1999; Yang and Liu, 2002).

The Indo-Asia orogenic system is the representation of one of the largest collisional events on Earth, making it one of the most studied areas in the world (Allen, 1999). Although a broad scale tectonic history of Central Asia has been developed (Lin et al., 2012; Lin et al., 2013; Lan et al., 2015; Han et al. 2017), a synthesis of the interplay between tectonic stresses, sedimentation, and primary and secondary structures has not been performed in the Central Tarim Basin far from

the current boundaries of the basin. Stress propagation along the Himalayan collisional zones and into the Tarim basin is still controversial (Sun et al., 2017; Carroll et al., 2010; Yang and Liu, 2002). Therefore, further understanding of the current stress state and its relationship with the recent tectonic history and bounding fault mechanisms is needed.

The primary goals of this investigation are to determine the current in situ stress conditions in the Tazhong Uplift, located in the Central Tarim Basin, to examine the effect of pre-existing structures in subsequent deformational events since the Cambrian, and to expand our understanding of the current lack of reactivation of pre-existing structures. Seismic reflection data and well-log data are used to document the structure and reactivation history and determine the in situ stress conditions in the Tazhong Uplift. High resolution 3D seismic data allowed the interpretation of the geometric characteristics, deformation timing, vertical and horizontal displacements of faults throughout the area, and borehole image logs and rock strength data are used to constrain magnitude and orientations of in situ stress. Analysis of seismic and well-log data contribute to understanding the absence of modern fault reactivation in the Central Uplift and to reconciling the intrabasin quiescence with the high levels of tectonic activity at the basins margins, particularly along the Altyn Tagh fault which bounds the basin to the south.

GEOLOGIC BACKGROUND

Late Proterozoic to Early Ordovician

The Tarim block separated from the Kuruktag-Tian Shan plate (north) and Tekililtag-Altun plate (south) during the Late Proterozoic, and a crystalline basement dominated by diorite, amphibolite, and gneiss lithologies was established in the study area (Li et al., 2012; Yuzhu and Zhihong, 1996). Two oceans formed during the Late Proterozoic to Early Ordovician: The Kudi Ocean, between the Kunlun terrane and the Tarim block, and the South Tian Shan Ocean between the Tarim block and the Middle Tian Shan plate (Figure 3; Li et al., 2012; Han et al., 2017).

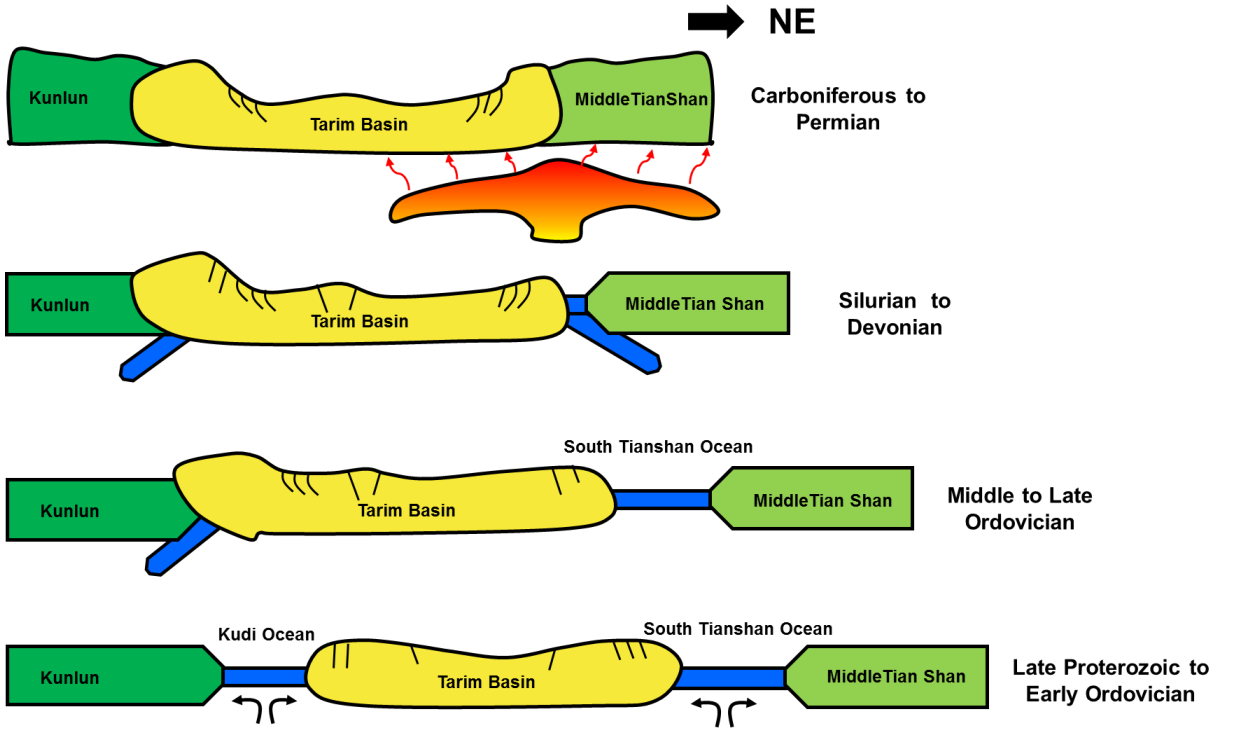

Figure 3: Simplified cross-section displaying the tectonic evolution of the Tarim Basin from the Late Proterozoic to Permian. Timing and relative plate motion information was synthesized from the literature (Reprinted from Su et al., 2011 and Li et al., 2012).

Extension of the crust generated an array of normal faults and initiated a period of protracted fault-controlled subsidence and sedimentation (Lin et al., 2015) characterized by deposition of limestone, dolomite, and evaporites (Figure 4; Li et al., 2012). Faults offsetting the basement are predominantly situated along the periphery, rather than the interior of the basin. Some intrabasinal extensional faults are present in the internal regions of the basin (Lin et. al 2015). The evolution of these basement faults in the central basin has been interpreted using aeromagnetic, gravitational, and seismic data. Two major normal faults striking S80°W mark the boundary between the Tazhong Uplift and the North Depression (Li et al., 2012; Lin et al., 2015). These extensional faulting appears to have influenced the structural framework of the region after the Early Ordovician (Lin et al., 2015).

Middle to Late Ordovician

During the Middle Ordovician, the Tarim oceanic crust subducted underneath the Kunlun block (Figure 3; Mattern and Schneider, 2000; Lan et. al, 2014; Han et. al 2017). In the Late Ordovician the Kunlun terrane collided with the Tarim block, causing northwest motion of Tarim, and forming a peripheral foreland basin in the southwest (Lan et al., 2015). Changes in the far-field stresses associated with oceanic-lithosphere and continent-continent collision resulted in the formation of paleo-uplifts and depocenters, including the Tazhong Uplift (Lan et. al, 2015). Crustal shortening characterized by a thick-skin tectonic style, created a series of reverse faults striking in the NW direction and with offsets of up to 800m, as well as folds, back thrusts, fault-bend folds, and fault-propagation folds (Li et al., 2013).

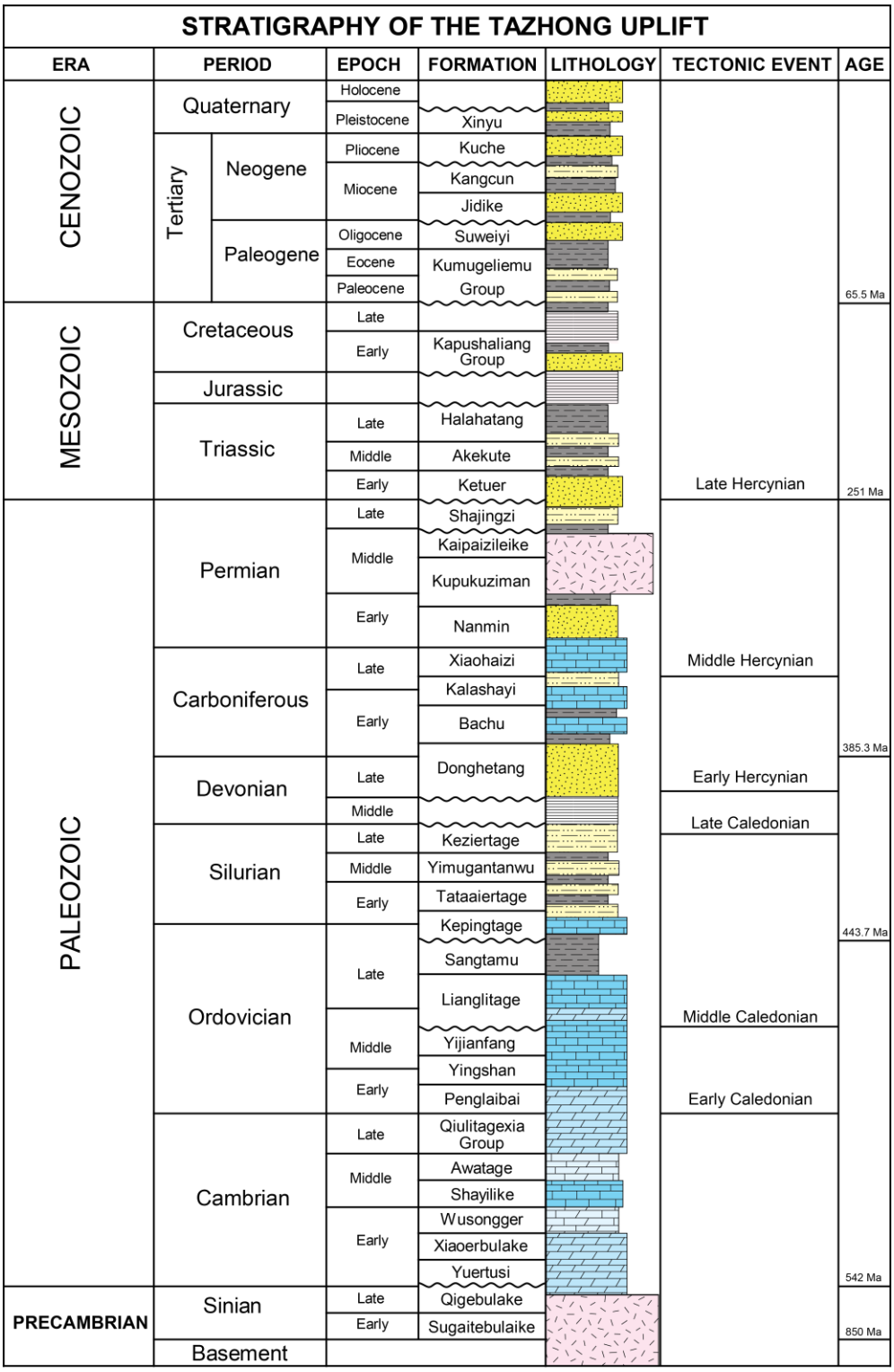

Figure 4: Stratigraphic column of the Tazhong Uplift showing formation names, lithologic units, and significant tectonic events.

Through the analysis of 3D seismic data and magnetic data, several authors, suggest that extensional faulting observed in Early Proterozoic to Early Ordovician sediments influenced Later Ordovician deformational events. (Li et al., 2012; Lin et al., 2015). Fault distribution, geometry, and scale, as well as thickness variation of strata within Precambrian and Ordovician units, indicates that existing normal faults were reactivated in reverse faults (Li et al.,2012 and Lin et al., 2015). Although the influence of paleo-stresses in the tectonic rejuvenation of the area is briefly described in the literature (Lin et al.,2015), a descriptive explanation on how stress magnitudes and orientations have influenced reactivation is not addressed. Two questions remain unresolved: is fault reactivation ubiquitous in the Tazhong Uplift? Why are faults not currently active?

In the Middle and Late Ordovician, thick sequences of calcareous mudstones, limestone, dolomite, and evaporates were deposited in the basin during the Ordovician, along with reef deposits that primarily deposited in structural highs (Figure 4; Li et al., 2012; Zhang et. al, 2014). The formation of the reverse fault system and uplift of the Tazhong anticline led to the local exhumation of Middle and Late Ordovician carbonate deposits and formed two unconformities during this period (Yu et. al, 2015). Ordovician carbonate facies were exposed for over 10 Ma resulting in diagenetic alterations, erosion of more than 1000 m of sediments, and karstification in a widespread area of the Tazhong Uplift (Yu et. al, 2015; Li et al, 2012). Although karstification was controlled primarily by exposure of Ordovician carbonate sediments, the presence of fault permeability could have favored fluid flow through damage zones promoting the dissolution of limestone and resulting in diagenetic alterations of the host rock (Lan et al., 2014).

Silurian to Permian

From Silurian to Carboniferous times, the Tian Shan Ocean (northwest) progressively closed east to west as a result of the Hercynian orogeny (Figure 3; Charvet et al., 2011; Lan et. al 2014). The Tian Shan island arc formed concurrently as a result of the northward subduction of the Tian Shan Oceanic plate (Lan et al., 2014). Closure of the Kudi and Tian Shan oceans and uplift of bounding orogens triggered deposition of interbedded tidal-flat deposits, sandstone, and mudstones in the Tarim Basin (Figure 4; Li et al., 2012; Li et al., 2013). Numerous steeply dipping NNE sinistral strike-slip faults that cut the older, NW striking dip slip faults, are characterized by flower structures and minor vertical offsets within the Silurian and Carbonifeorus strata are found in the Tazhong Uplift (Lan et al., 2014; Han et al., 2017). Due to the impact of strike-slip faults on the migration and accumulation of oil and gas, these faults have been widely studied, but interpretations of timing and formation processes of the strike-slip faults are inconsistent or poorly constrained (Li et al., 2013; Lan et al., 2015; Wu et al., 2016; Han et al., 2017).

Based on 3D seismic interpretation, some authors suggest the NNE oriented strike-slip faults developed during the collision of Tian Shan and Tarim blocks from Silurian to Carboniferous times, whereas others propose the faults are associated with the collision of Kunlun and Tarim blocks in the Ordovician (Lin et al., 2013; Lan et al., 2015; Han et al., 2017). More recent analysis of strike-slip faults in the Tazhong Uplift suggests that the faults developed in two stages. Han et al. proposed transpressional sinistral strike-slip faults (positive flower structures) formed during the Caledonian event while strike-slip associated with transtensional regimes (negative flower structures) could have formed later during the Hercyanian orogeny as a result of the closure of the Tian Shan Ocean. Although the geometry of the strike-slip faults has been described in detail (Lin et al., 2013; Lan et al., 2015; Han et al., 2017), the reasons for fault

reactivation and the control of strike-slip faults in subsequent deformation has not been clearly stated.

Continent-continent collision continued during the Carboniferous and Permian when the Tarim block collided with the Kazakhstan (northwest) and Siberian plates (north). In the Late Permian, the Tarim block continued to experience flexural subsidence as the Tian Shan and Kunlun orogenic belts uplifted. Carboniferous strata consist of limestone, shale, and sandstones (Figure 4) (Li et al., 2012; Li et al., 2013). Permian sediments are conformable with Carboniferous deposits and are dominated by volcanic rocks, sandstone, and mudstones (Figure 4; Yang et al., 2016).

Volcanic rocks are widely distributed within Carboniferous and Permian strata in the Tarim Basin. However, the provenance of the igneous activity is still poorly understood (Su et al., 2011; Yang et al., 2016). Geochemical data suggest that magmatic activity is associated with a mantle plume caused by a modification of the upper mantle (Figure 3; Su et al., 2011; Yang et al., 2016). This resulted in mantle upwelling into the Tarim lithosphere and generated extrusive igneous bodies over a wide region of the Tazhong anticline (Yang et al., 2007, 2016). Permian volcanic deposits are abundant the Tazhong Uplift and in other areas of the basin. Based on seismic data analysis some authors suggest that intrusion of magmatic plugs and the emplacement of magmatic extrusions preferentially occurred along pre-exiting strike-slip structures and promoted the reactivation of the faults (Li et al., 2012; Li et al., 2013). However, explanation regarding the preferential intrusion pathway of magma and the causes of fault reactivation due to volcanism are not extensively addressed in the literature (Li et al., 2013).

Even though most of the literature refer to the igneous edifices as Permian in age (Li et al., 2012, 2013; Yang et al., 2007, 2016), localized Triassic deformation adjacent to the intrusions

could indicate that volcanism did not cease until the Triassic. Further analysis of the geometry and timing of volcanic bodies is needed.

Mesozoic to Present

Minor deformation in the interior of the basin occurred during the Mesozoic. Mesozoic sediments consisting primarily of interbedded sandstones, mudstones, and conglomerates are conformable and laterally continuous (Figure 4; Lee, 1985). Although Mesozoic and Cenozoic sequences are relatively flat, Triassic faulting is present in the Tazhong Uplift. Triassic faults appear to be distributed adjacent to volcanic extrusions; however, the relationship between Triassic faulting and igneous remains poorly constrained.

The continental collision between the Indian and Euroasian plates initiated a period of convergence that resulted in the Uplift of the Tian Shan, Kunlun Shan, and Altyn Shan orogenic belts and stimulated subsidence of the basin foredeeps (Figure 5; Jia et al.,1998). The development of the Himalayan-Tibetan Plateau controlled the compressional stress regimes exerted in the Tarim basin and in the surrounding regions (Jia et al.,1998; Allen et al., 1999; Busby and Perez, 2012). The peripheries of the Tarim basin are seismically active zones and contain complex fault systems dominated by thrust belts and strike-slip faults (Figure 2; Allen et al., 1999; Sun et al., 2017). The western Kunlun Shan and the Tian Shan orogenic belts are characterized by active thrusting and have experienced up to 100 km to 35 km of shortening respectively (Allen et al., 1999; Yang and Liu 2002). The Altyn Tagh Fault is an active intraplate sinitral strike-slip fault that bounds the northern boundary of the Tibetan Plateau. The N70°E tending Altyn Tagh Fault is believed to have accommodated one third of the convergence caused by the Himalayan Orogeny (Figure 1; Yin et al., 2002; Taylor and Yin, 2009).

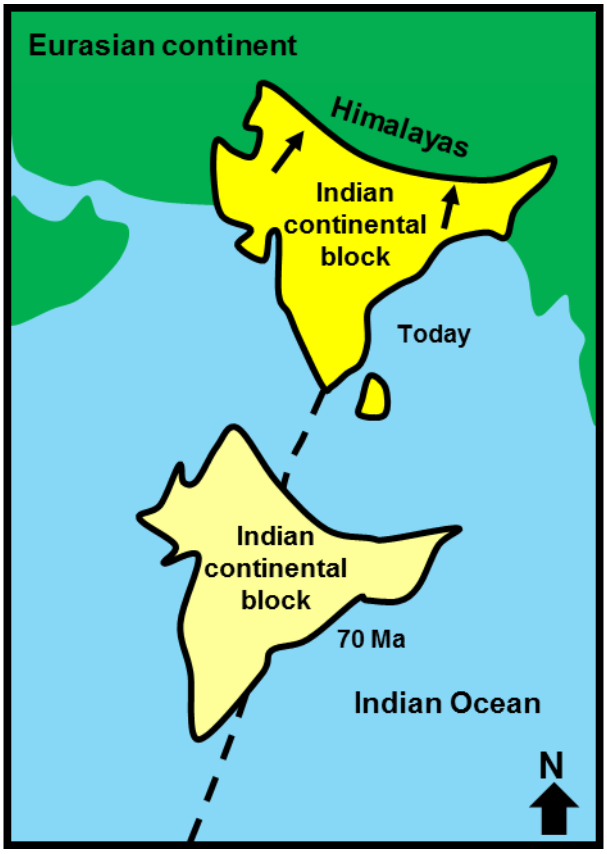

Figure 5: Schematic map of showing the location of the Indian continent prior and after its collision with Asia (Eurasian plate).

Based on limited seismic activity, the laterally continuous character of Cenozoic layers observed in seismic profiles, and geodetic data it is known that the interior of the Tarim Basin has experienced very limited deformation in the Cenozoic (Allen et al., 1999; Carroll et al., 2010; Sun et al. 2017). This conundrum has prompted inquiries into whether a change in stress-sate conditions has occurred, and if pre-exiting structures could be reactivated under a different stress regime in Central Tarim.

METHODOLOGY

Data Sources

A geophysical data set for a 4284 km^2 area of the northern slope of the Tazhong Uplift (Figure 6) consisting of three, 3D, post-stack depth-migrated, overlapping seismic data volumes (Survey TZ-45, Survey TZ-45 South, and Survey Z8-43) and data from nineteen wells including geophysical logs and associated drilling and geologic reports, was provided by China National Petroleum Corporation (CNPC). The processing of seismic data and intervals logged by the CNPC focused on resolving characteristics of the Paleozoic and Mesozoic section, and more specifically, the hydrocarbon-producing Ordovician carbonates at approximately 6000 m measured depth.

Seismic data

The zero phase seismic volumes consist of orthogonal inline and cross line profiles trending 036.8˚ and 143.2˚, respectively, with a horizontal resolution of 25 m (bin size: 25 m x 25 m). Acquisition parameters for surveys TZ45-, TZ45-South, and ZG8-43 are summarized in the tables below:

Table 1. Acquisition parameters for survey TZ-45.

Size	1546 km^2
Total number of inlines	1566
Total number of crosslines	1582

Table 2. Acquisition parameters for survey ZG8-43.

Size	1649 km^2
Total number of inlines	1661
Total number of crosslines	1591

Table 3. Acquisition parameters for survey TZ45-South.

Size	1089 km^2
Total number of inlines	1801
Total number of crosslines	9066

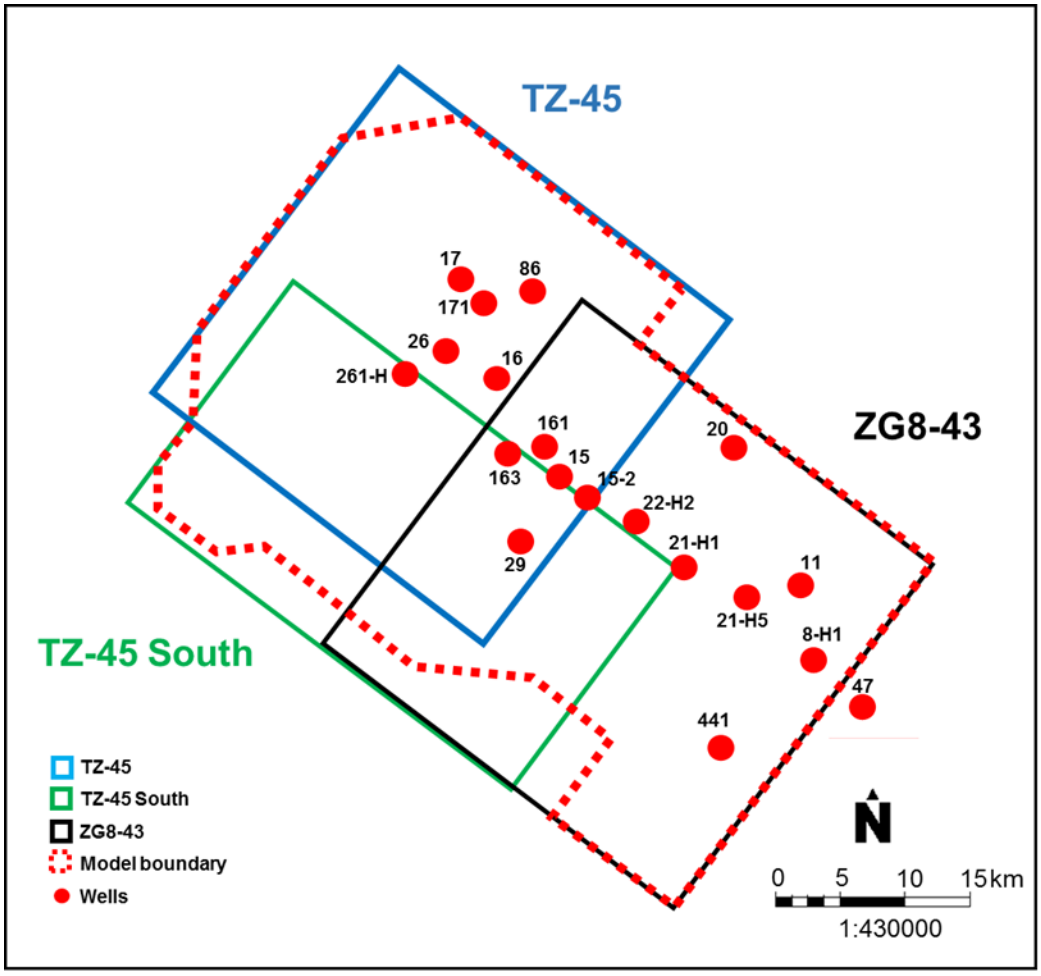

Figure 6: Outline of the three seismic surveys areas (TZ-45, TZ-45 South, and ZG8-43), well locations, and the model boundary used in this study.

The surveys TZ-45, TZ45-South, and ZG8-43 were interpreted independently because of a vertical mismatch between the volumes at depth. For instance, seismic surveys display a vertical

disparity of approximately 50-60 m in the top of the Ordovician unit. The inaccuracy is reflected in map view at the volume boundaries. The vertical incongruity between the surveys was taken in consideration for the stratigraphic and structural interpretation of the area.

Three-dimensional seismic attributes were applied in the seismic volumes to enhance the identification of geologic structures such as faults, igneous bodies, and unconformities. Geometric attributes of variance, curvature, strike and dip were determined for seismic volumes to facilitate the accurate interpretation of faults, the identification of piercing points via restoration of depth and stratal slices, and the identification of volcanic bodies. Attributes are displayed in cross section or map view (both depth and stratal slices) and computed from interpreted horizons and fault surfaces.

Well-log data

Eighteen of the nineteen wells are located within the seismic volume (Figure 6). Gamma ray, sonic, density, and resistivity are available for the majority of the wells. Density logs were only registered throughout Ordovician age strata while sonic and gamma ray logs cover Ordovician through Mesozoic strata. Borehole image logs cover only the Ordovician sequences in thirteen wells. The logs for each well are specified in Table 4.

Drilling and geologic reports contain relevant well information used in this investigation including: formation tops, core description of Paleozoic units, formation fluid pressure, formation temperature, and density gradients.

Table 4. Available well logs in the study area.

Well name	Caliper	Density	Gamma Ray	Sonic	Resistivity	FMI
11	*	*	*	*	*	*
20	*	*	*	*	*	*
47	*	*	*	*	*	*
441	*	*	*	*	*	*
8-H1	*	*	*	*	*	
22-2H	*	*	*	*	*	
21-H5	*		*	*	*	
21-1H	*		*	*	*	
86	*	*	*	*	*	*
15	*	*	*	*	*	*
15-2	*	*	*	*	*	*
16	*	*	*	*	*	*
17	*	*	*	*	*	
26	*	*	*	*	*	*
29	*	*	*	*	*	*
161	*	*	*	*	*	*
163	*	*	*	*	*	*
171	*	*	*	*	*	*
261-H	*		*	*	*	

Due the lack of seismic data in the time domain and the velocity model used in the time to depth migration, synthetic seismograms were not generated. However, well-log acoustic impedance was compared with seismic reflection data in order to calibrate and correlate formation tops with seismic horizons.

The seismic resolution decreases with depth within each seismic volume causing a minor disparity between well tops and the corresponding seismic reflectors. The discrepancy between well formation tops and the conforming seismic horizon does not exceed 80 m, and considering seismic resolution limitations at depth, the calibration between well tops and seismic reflectors is acceptable.

Well-log data analysis

Paleozoic and Mesozoic stratigraphic units were identified based on petrophysical and core data from CNPC drilling and geologic reports. Gamma ray, sonic, density, and resistivity logs were used for correlation between the eighteen wells, but are not equally available for all wells (Figure 7; Table 4). Different facies were identified using well-log data and the boundary between representative formations were used as a constraint for seismic horizon interpretation (Figure 7). Density and sonic logs were used to create acoustic impedance logs to facilitate interpretation of the seismic reflection data.

Seismic Interpretation

The structural and stratigraphic relationships of Paleozoic and Mesozoic sedimentary sequences and unconformities were characterized by mapping particularly distinct and continuous reflectors throughout the study area. The interpreted reflectors result from significant changes in impedance (peaks and troughs) and correlate with the formation contacts mapped in well-log data (Figure 7).

On the basis of geometry, discontinuities, offsets, and disruptions of seismic reflectors and other attributes (e.g., variance), faults were mapped throughout the study area as resolution permitted. Mapping focused on documenting the fault geometry (e.g., strike and dip, segmentation, branching), and the magnitude and sense of separations in primary and secondary faults in cross-sectional profile and map views.

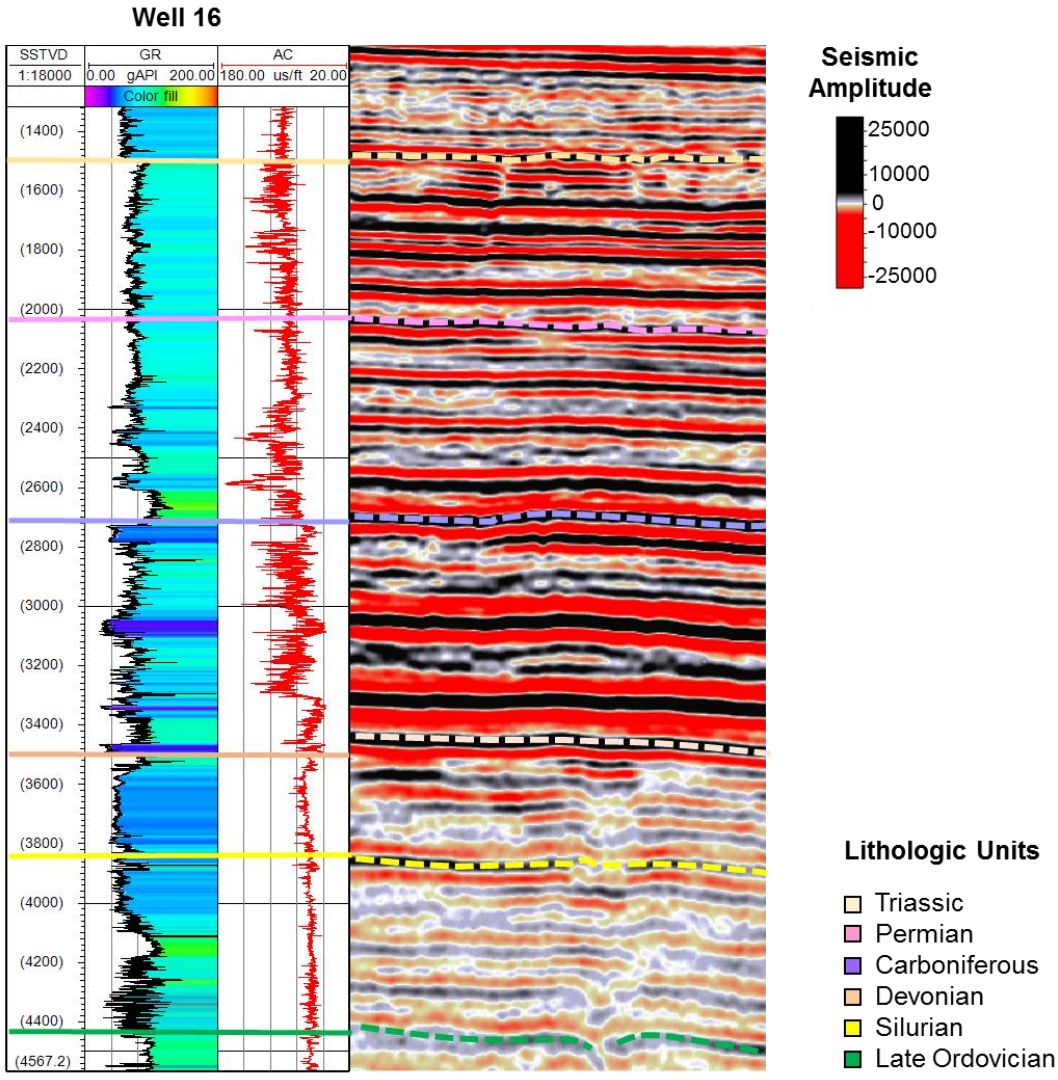

Figure 7: Example of well to seismic calibration using well 16. To the left, gamma ray and sonic logs with interpreted formation tops. To the right, amplitude seismic profile intersecting well 16 and displaying interpreted horizons. Note that seismic horizon is slightly offset from the correlative formation top by a determined value.

Faults with reverse and normal separation were identified by apparent offset of strata. Total fault displacement and throw was calculated by comparison to 3D models and their relevant lithological units and fault surfaces. Displacement and throw was measured at intersections between fault surfaces and horizons. Simple 2D restorations were performed to determine relative

sedimentation rates across faults. For identification of strike-slip faults in relatively horizontal strata, as the case herein, the following concepts were employed (after Christie-Blick and Biddle, 1985; Zalan, 1987).

- Strike-slip faults are often sub-vertical.
- Strike-slip faults tend to diverge in a series of secondary faults or "flower structures."
- Strike-slip faults display complex geometries such as horsetail splay and en-echelon fractures.
- Dip and fault throw change with depth.
- Strike-slip faults can exhibit different deformation intensities along the fault as well as changes in the lateral continuity of sedimentary facies.

Borehole image-log analysis

For this investigation, borehole image logs were analyzed in thirteen vertical wells (Table 4). The logs were created by processing resistivity data collected using the Formation MicroImager (FMI). The resulting images of the wall of the borehole, as a function of measured depth, show the local relative resistivity of the formation, where high conductivity is represented by darker shades and low conductivity by lighter shades. Spatial resolution is intrinsically governed by the size of the sensors on the tool. The images for a vertical borehole are oriented with respect to the geographic coordinate directions such that the orientation of planar features intersecting the borehole (bedding, fractures) and deformation of the borehole wall can be determined graphically.

To carry out in situ stress analysis, drilling-induced deformation of the borehole walls, specifically borehole breakouts and drilling induced tensile fractures (DITF), evident in image logs were characterized (Figure 8). Breakouts may be distinguished in images as two vertical linear

zones oriented 180° opposite, which typically are less resistive (darker) than the undeformed wall rock, and appear relatively less focused than the undeformed portions of the borehole wall (Figure 8; Tingay et al., 2008). Measurements of breakouts include the orientation (azimuth) and the average angular width. If apparent breakouts occur on only one side of the borehole, or are not diametrically opposed, or do not extend for more than 1 m length, then measurements were not collected. DITF appear as narrow, sharp, conductive features that also are diametrically opposed in opposite sides of the wellbore wall (Zoback, 2010). DITF are narrower than borehole breakouts and usually propagate as a single fracture, or as en-echelon array of fractures, parallel to the borehole axis (Figure 8; Tingay et al., 2008). When both DITF and breakouts occur in the same borehole they are generally orthogonal, i.e., the azimuths are 90˚ different. The azimuthal direction of the breakouts and DITF may be measured directly off image logs because the deviation of the wellbores (from vertical) did not exceed 5°-8°.

It is well understood that the orientation of borehole breakouts and DITF are a function of the orientation of the far-field principal stresses, and that occurrence of these induced deformation features depends on the concentration of the far-field stress at the borehole and rock strength (e.g., Zoback, 2010). In vertical boreholes, the concentration of the maximum and minimum far-field horizontal stresses, S_{Hmax} and S_{hmin}, produce local maximum and minimum circumferential compressive stress at the borehole walls that form breakouts and DITF, respectively (Figure 8). It follows that breakouts form in directions perpendicular to the direction of S_{Hmax}, and the DITF form in directions perpendicular to S_{hmin} (Figure 8; Zoback, 2010), such that the orientation measurements of breakouts and DITF give the orientation of S_{Hmax} and S_{hmin} directly. For each borehole, the orientation of S_{Hmax} and S_{hmin} was averaged using the breakout length (length weighted mean).

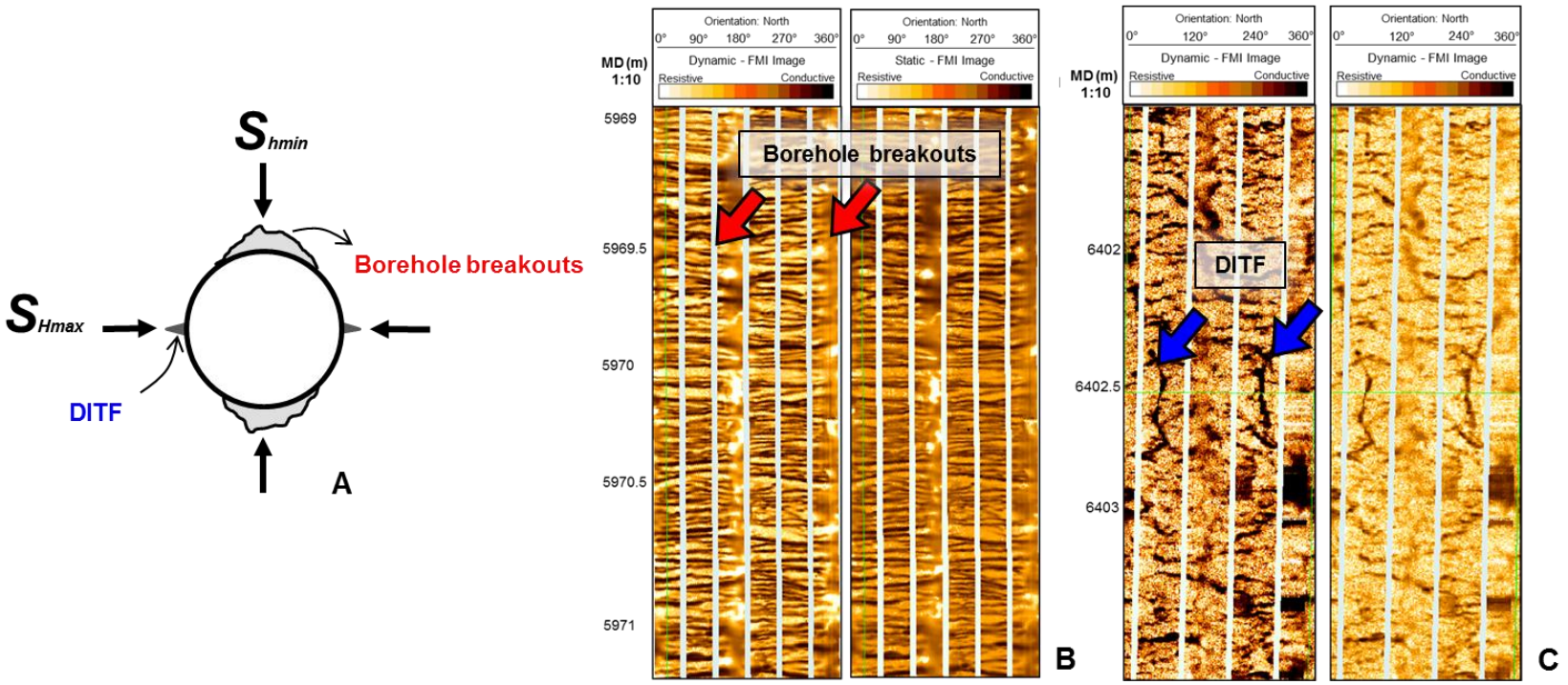

Figure 8: Occurrence of borehole breakouts and DITF in vertical wells. **A**- Schematic diagram showing the geometric relationship of maximum and minimum horizontal stress directions with position of drilling-induced deformation along a vertical borehole. The plane of projection is perpendicular to borehole axis with the thick black circle representing the borehole and the gray features representing deformation structures. Borehole breakouts occur at the azimuth of minimum horizontal stress while DITF occur at the azimuth of the maximum horizontal stress. **B**- Borehole image log displaying borehole breakouts. **C**- Borehole image displaying DITF. Note breakouts and DITF occur as diametrically-opposed paired features.

RESULTS

Geometry and kinematic of structures in the Tazhong Uplift

The Tazhong Uplift is comprised of Paleozoic to Cenozoic age sedimentary rock, with a total thickness of over ten thousand meters. The structure of the sedimentary rock is defined by 3D mapping of nine seismic reflectors that coincide or closely follow the upper formation contacts of the Middle Cambrian, Cambrian, Middle-Late Ordovician, Ordovician, Silurian, Devonian, Carboniferous, Permian, and Triassic. The formations are relatively horizontal and are regionally continuous, but locally are offset, tilted and disturbed by faults, folds and igneous bodies. The new kinematic model described here demonstrates the characteristic geometries, displacement magnitudes, and age of activity of different fault systems. In some cases, structural and stratigraphic relationships document more than one episode of deformation of distinct fault systems and tectonic reactivation.

Middle-Late Ordovician reverse faults

Attitude and geometry of Ordovician faults

From seismic data, two populations of faults are observed. The first consist of a NW-striking master reverse fault (often referred as T1 or Tazhong No.1; Li et al., 2011) that deforms Early Paleozoic units (Cambrian-Ordovician) and penetrates the basement (Figure 9). The second consists of a series of secondary (small scale) faults with similar strike (Figure 9).

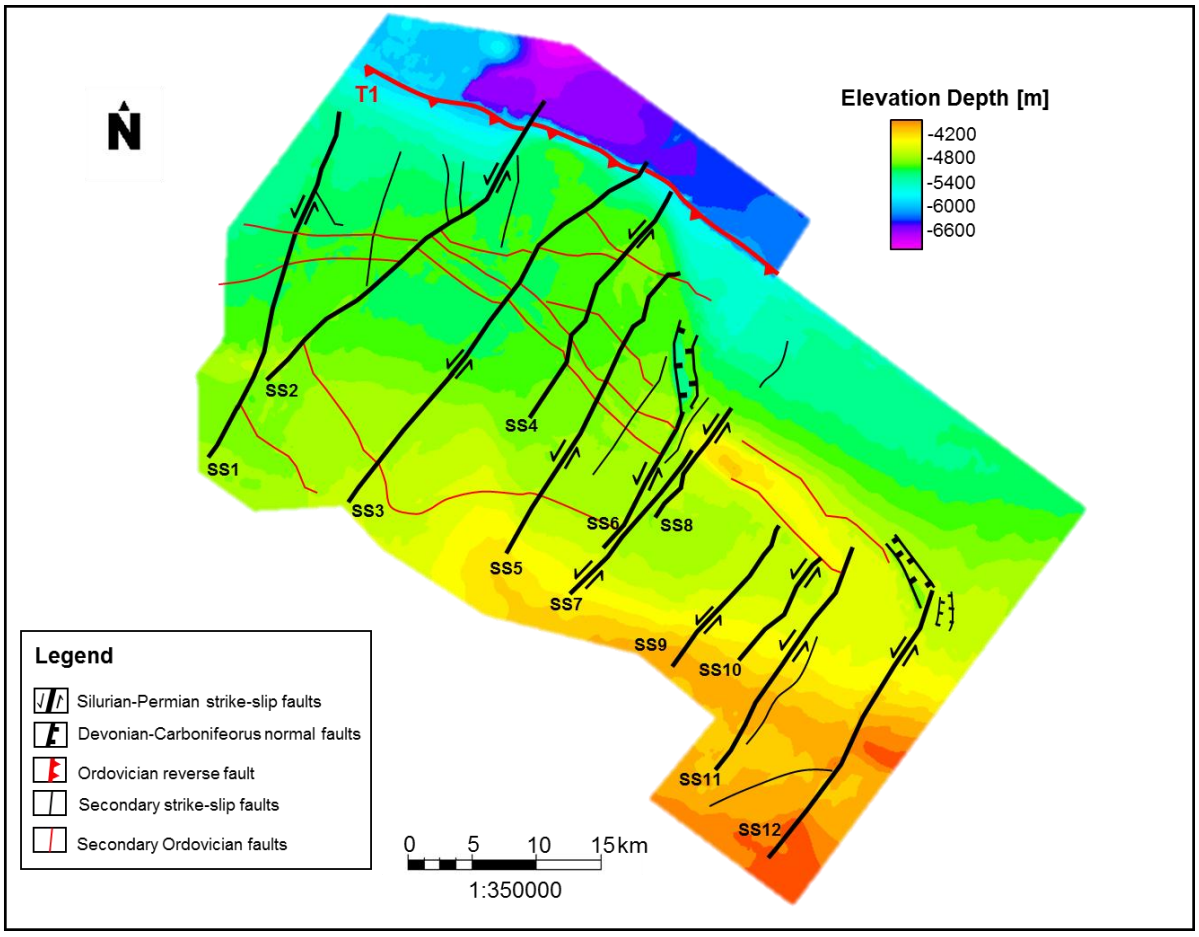

Figure 9: Structure map of the top of the Middle-Late Ordovician horizon (Lianglitage Formation). Structure map of the top of the Middle-Late Ordovician horizon (Lianglitage Formation). The map displays Silurian-Permian left-lateral strike-slip faults and Devonian-Carboniferous normal-faults in black, and Ordovician faults in red. The strike-slip faults are numbered for reference purposes.

The T1 fault strikes 320° ± 10°, dips toward the southwest, and displays reverse separations (Figure 10). There is a systematic loss of coherency in the seismic signal near the T1 fault in seismic amplitude and variance profiles (Figure 10). The T1 reverse fault penetrates Cambrian and Ordovician units and terminates upward against Middle-Late Ordovician units (Figure 10). Growth strata is observed above the tip of the fault within Late Ordovician units (Figure 10). T1 extends

along strike up to 41.7 km, and even though the extent of the fault cannot be detected in the northwest region, it is well documented that the fault extends towards the southeast and to the northwest (Li et al., 2012, 2013).

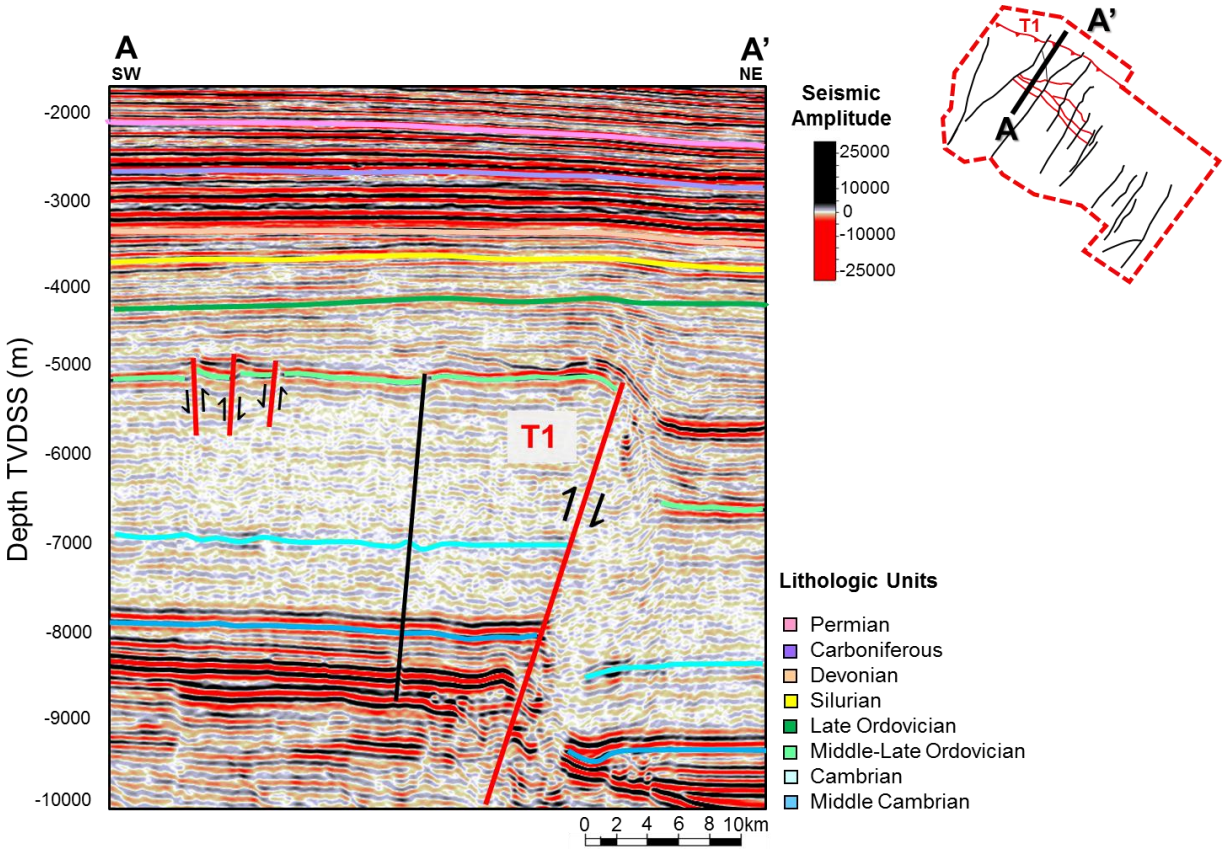

Figure 10: Interpreted seismic amplitude profile across the T1 structure along section A-A'. Ordovician faults are illustrated in red, and a secondary strike-slip fault in black. Note the clear evidence of growth strata associated with fault offset and folding.

It was not possible to directly determine whether or not the reverse fault T1 is a basement involved fault, because seismic reflection data set does not image the crystalline basement. Area-depth analysis and trishear forward modeling were conducted using StructureSolver©. The forward

model, which involves symmetric trishear modeling for fault-propagation fold, takes into account the geometry of the fault, trishear angle, axial shear angle at fault bends, magnitude of slip, and stratigraphic horizons at depth (Eichelberger et al., 2015;2017). Area-depth strain analysis and trishear fault-propagation fold modeling provides a computed solution for fault trajectory at depth based on the displaced fold area of pregrowth and growth seismic horizons, allowing the estimation of the fault dip, fault throw, and slip magnitude (Figure 11).

The results reveal the fault persists approximately 5700 to 6550 m below the hanging wall of the Middle Cambrian formation, suggesting T1 penetrates into the basement (Figure 11). The fault trajectory indicates the fault is not listric but dips with a constant angle of 42±5° SW and terminates upward into a fault-propagation fold that is overlain by nearly horizontal layers of Late Paleozoic age (Figure 11). The Cambrian units experienced the largest magnitude of slip, approximately 990 to 1285 m, which diminishes upwards into younger units. The maximum fault throw is around 1430 m in the vicinity of well 86. There are not thickness variations from the Middle Cambrian to the Middle-Late Ordovician units, suggesting that the fault formed or reactivated after the deposition of Cambrian and Middle-Late Ordovician strata. The presence of Late Ordovician growth strata (syntectonic strata) indicates that the T1 fault was active through the Late Ordovician (Figure 11).

Thickening in the hanging wall was observed within Middle Cambrian age units (at a depth of approximately -9500 m TVDSS). The thickening suggests the presence of a pre-existing normal fault and potential tectonic inversion (Figure 11). The structural model indicates that a pre-existing normal fault reactivated into a fault-propagation fold after the deposition of the Middle-Late Ordovician units, progressively developing and deforming Late Ordovician strata (Figure 11).

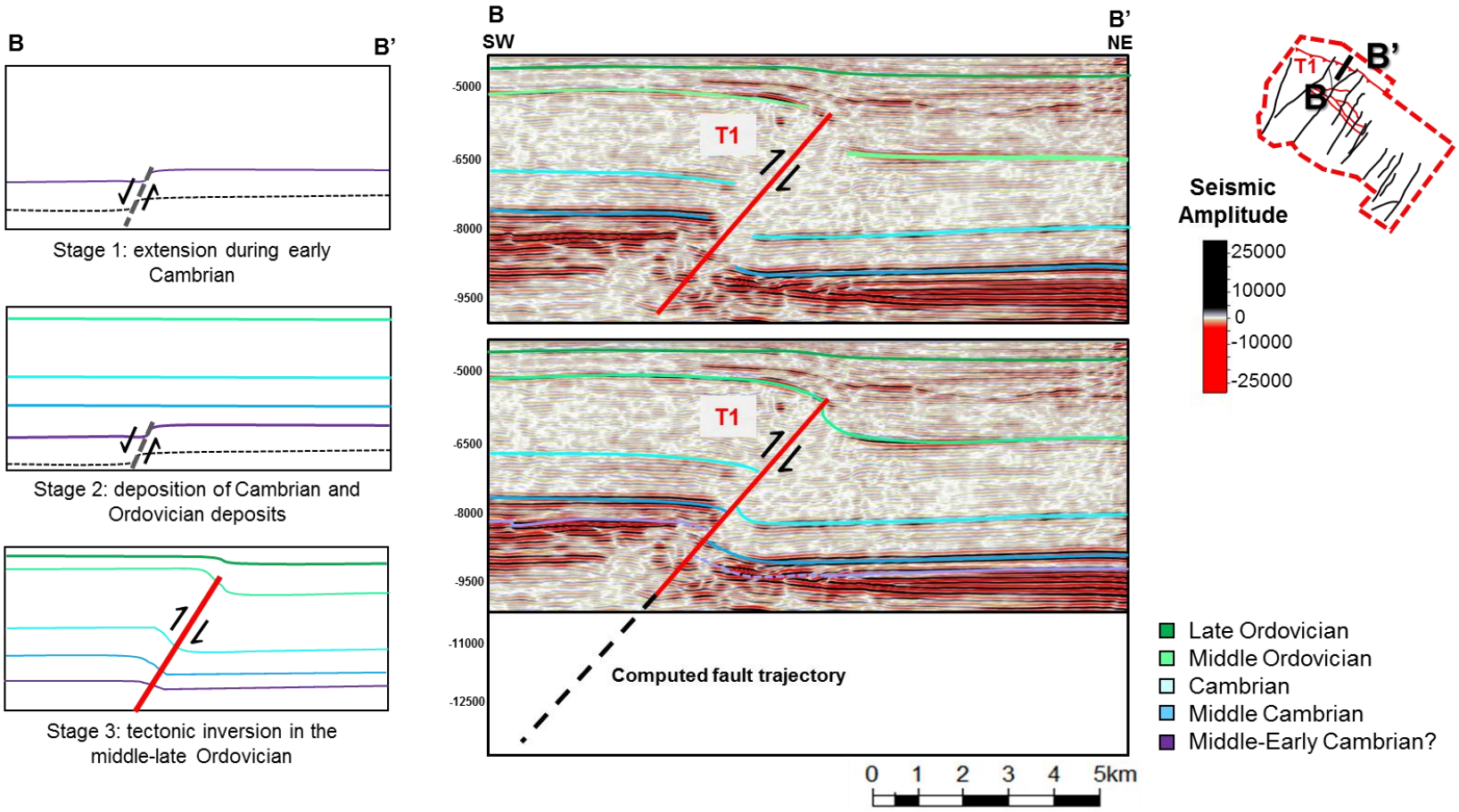

Figure 11: Kinematic model of the T1 reverse fault development over time constrained by offsets, folding, regional dips and growth strata. The left panel shows a simplified model of the evolution of the fault-propagation fold; the right panel provides the initial interpretation (top) and the final model interpretation (bottom) showing the T1 fault-propagation fold and computed fault trajectory. Ages of mapped horizons (formation tops) are identified by color.

Secondary Ordovician faults have an average strike of 308°±10° and an average dip of 85° ± 3° southwest or northeast (Figure 9). The secondary faults are significantly smaller than the T1 fault and display small normal and reverse separations of approximately 128±35 m. The faults tip out upward and cross-cut the Middle-Late Ordovician Lianglitage formation, but do not propgate downward into Early Ordovician or Cambrian units (Figure 10). The minor faults appear to be linked to a stratigraphic feature showing a characteristic depositional topography consisting of small domed structures with a relief of 200±100 m and a width of up to 650 m (Figure 10). The structures are likely associated to networks of coral-sediment ridges formed during reef growth. Coral sediment ridges, also known as "reticulate reefs" are a combination of calcareous and clastic sediments that evolved and are genetically related to karst topography (Schlager and Purkis, 2015).

The position and geometry of T1, along with the secondary faults are well represented by maps of the variance attribute in depth and stratal slices (Figure 12). Although the T1 reverse fault was mapped as a single fault surface, seismic variance and local deformation around the T1 fault suggest is a zone of deformation that possibly comprises localized shear zones within a damage zone of up to 1359±200 m thick (Figure 12). The variance depth slice at -5050 m (TVDSS) also shows the secondary faults associated with the morphological expression of coral-sediment ridges (Figure 12). The reticulate patterns formed parallel to T1, extend for distances of up to 40.3 km, and are bounded and genetically related with secondary faults (Figure 12).

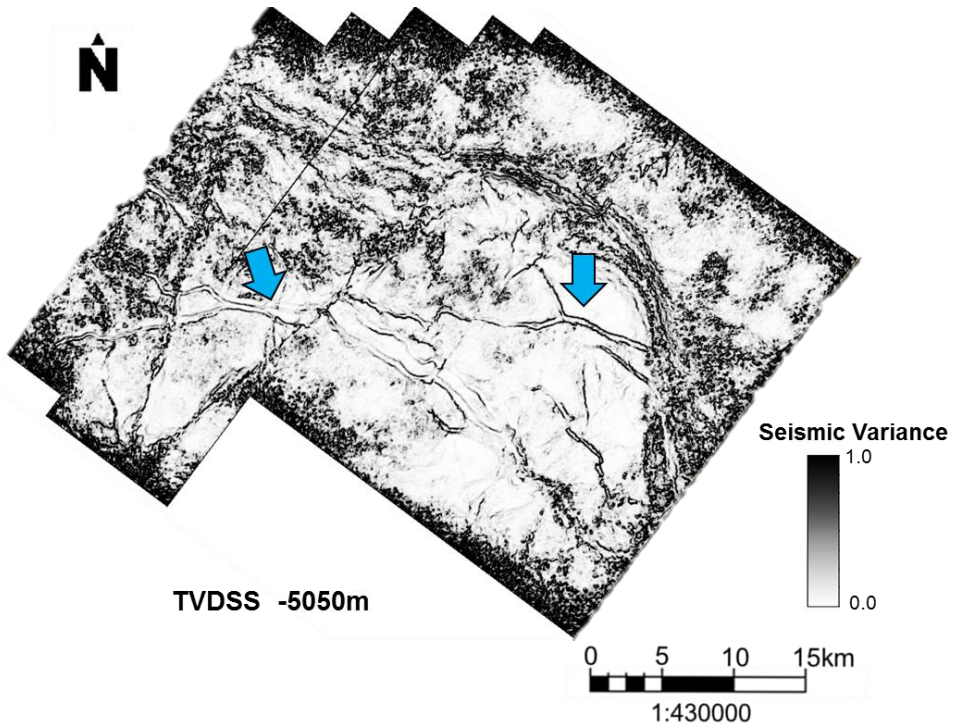

Figure 12: Variance depth slices extracted at -5050 m TVDSS displaying NW-striking Ordovician fault systems. Secondary faults and reticulate patterns are evident at this depth (blue arrows).

Silurian- Permian strike-slip faults

Attitude and geometry of strike-slip faults

Twelve NE striking faults sinistral strike-slip faults were mapped based or their characteristic vertical to sub-vertical geometries and the presence of flower structures. Strike-slip faults were named based on their location from west to east as: SS1, SS2, …, SS12 (Figure 9).

The strike-slip faults have an average strike of 036°±5° (best fit) and display steep dip angles of 86°± 3° (Figure 9 and 13). The dip direction is inconsistent along the faults. The magnitude and the left-lateral sense of slip of strike-slip faults has been determined from the restoration of seismic depth slices and the use of characteristic stratigraphic and structural features that served as piercing points.

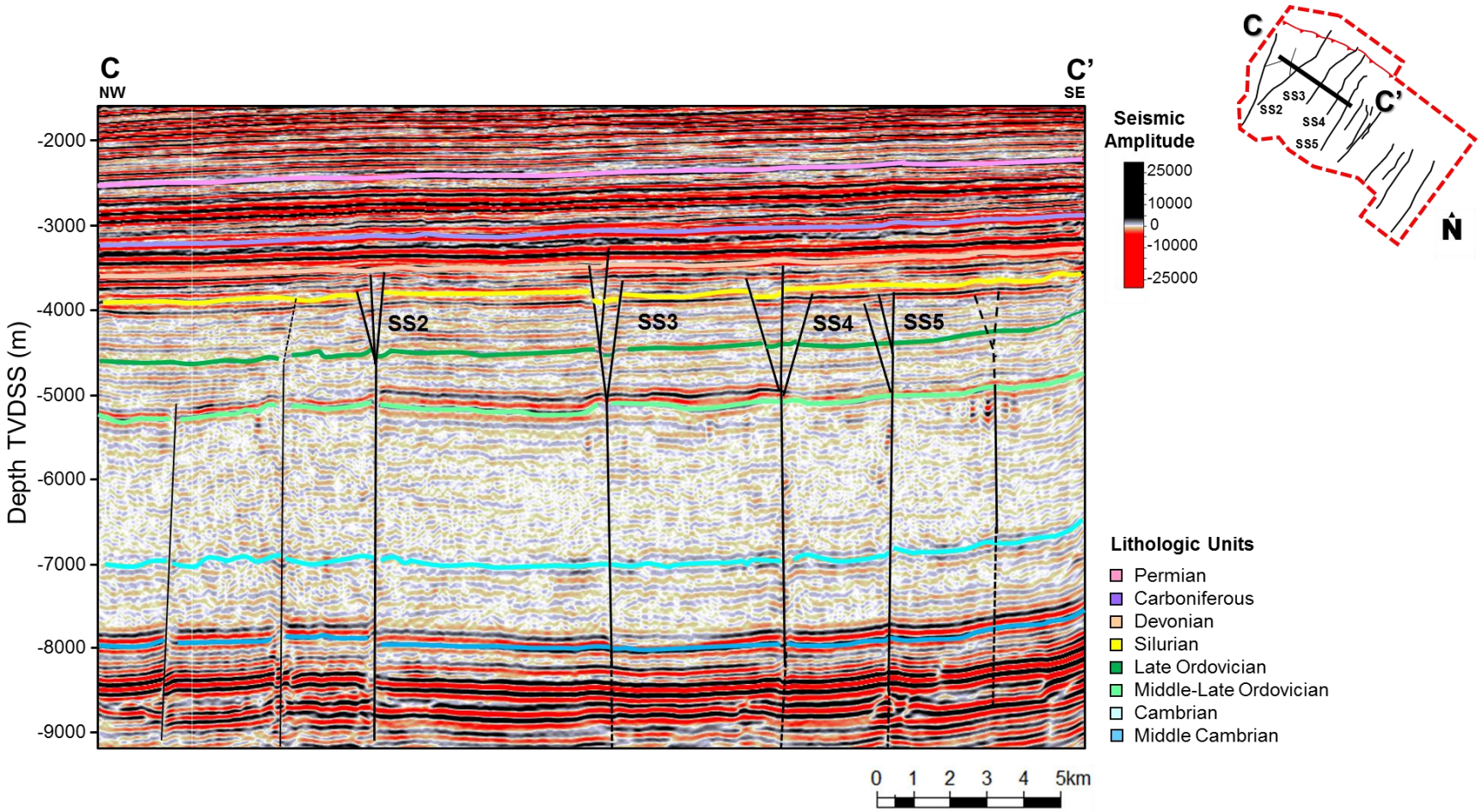

Figure 13: Interpreted seismic amplitude profile (C-C') through the TZ45 seismic volume. Silurian- Permians strike-slip faults are shown in black. The strike-slip faults exhibit subvertical planar structures in the Cambrian and Middle-Late Ordovician units and flower structures in Silurian to Carboniferous strata. Middle Cambrian to Permian formation tops are color coded.

The strike-slip faults are roughly perpendicular to the Tazhong low rise and cut both the Ordovician reverse fault T1 and minor Ordovician faults (Figure 9). Table 5 provides the attitudes and longitudinal extent of the strike-slip faults mapped in this study

Table 5. Location, attitude, and length of left-lateral strike-slip faults mapped in the seismic surveys.

Name	Location	Attitude	Length [km]	Type
SS1	TZ45	025°,85°	28.3	Left-Lateral strike-slip
SS2	TZ45	040°,87°	35	Left-Lateral strike-slip
SS3	TZ45	035°,83°	36.7	Left-Lateral strike-slip
SS4	TZ45	040°,85°	23	Left-Lateral strike-slip
SS5	ZG843	037°,83°	27.6	Left-Lateral strike-slip
SS6	ZG843	030°,85°	18.8	Left-Lateral strike-slip
SS7	ZG843	037°,87°	14.4	Left-Lateral strike-slip
SS8	ZG843	035°,86°	10.2	Left-Lateral strike-slip
SS9	ZG843	040°,88°	14.2	Left-Lateral strike-slip
SS10	ZG843	041°,87°	10.1	Left-Lateral strike-slip
SS11	ZG843	035°,84°	20.3	Left-Lateral strike-slip
SS12	ZG843	042°,89°	26.4	Left-Lateral strike-slip

Strike-slip faults show characteristic structural geometries at different stratal horizons. Overall, the steeply dipping faults display simple planar geometries within Cambrian and Middle-Late Ordovician age strata that open upward into a series of en-echelon secondary faults (flower structures) within the Late Ordovician, Silurian, Devonian, Carboniferous age sediments (Figures 13 and 14).

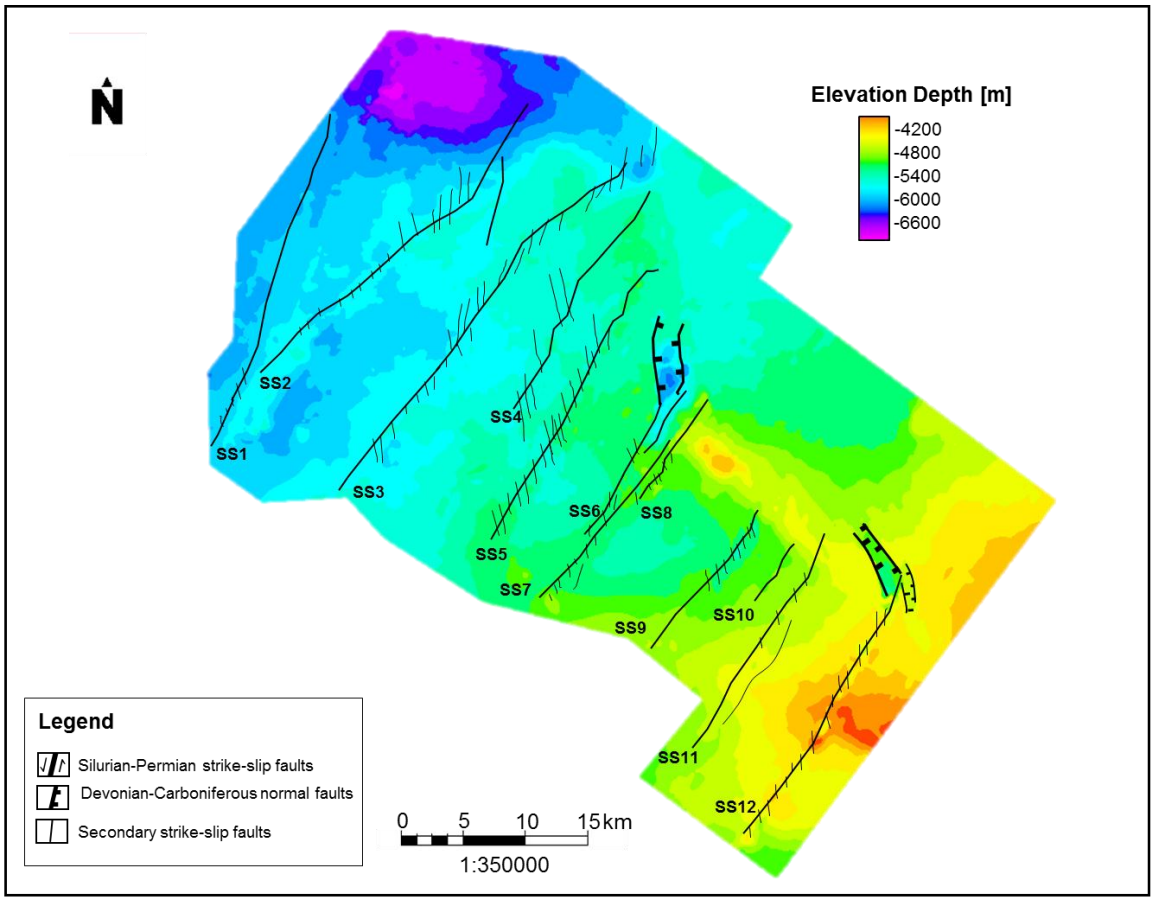

Figure 14: Structure map of the top of the Silurian horizon.The structure map displays the geometry of the older Silurian-Permian left-lateral strike-slip faults and Devonian-Carboniferous normal faults as thick black lines, and the overlying right-stepping en-echelon arrays as thin black lines.

Cambrian and Ordovician formations are, in some cases, vertically separated 50 to 250 m by the strike-slip faults. In younger strata (Silurian to Carboniferous), the strike-slip faults appear as right-stepping arrays of secondary faults centered directly above the principal displacement zone in older strata (Figure 14). The secondary faults display normal separations, generally associated with transtensional tectonic regimes and the formation of releasing bends and pull- apart

basins (Figure 14). The northern tips of fault SS6 and SS12 formed larger pull-apart basins that developed between two subparallel strike-slip faults (Figure 14).

The en-echelon normal faults are 500 to 3000 m long, relatively parallel to each other, and oblique to the planar zone (Figure 14). The distance between these faults is roughly constant ranging from 700 to 1000 m. The faults strike with angles of 045°±10° from the principal displacement zone and dip with angles of approximately 70°±15° (Figures 13 and 14). The en-echelon faults shorten downward and intersect all the deeper master faults but are evident in particular stratal horizons including: Late Ordovician, Silurian, Devonian, and Carboniferous.

Seismic variance was particularly useful to distinguish the presence of en-echelon arrays. At a depth of -7900 m TVDSS (a variance depth slice within the Cambrian age unit) faults display a relatively simple planar geometry (Figure 15). Similarly, a variance stratal slice extracted along the Middle-Late Ordovician age unit (Lianglitage Formation) faults appear as nearly parallel, discrete planar features that maintain a constant orientation (Figure 15). The right-stepping en-echelon faults are visible in variance at shallower depths (Figure 15). The right-stepping character of secondary faults and the presence of grabens is consistent with the left-lateral motion of the strike-slip faults (Figure 15).

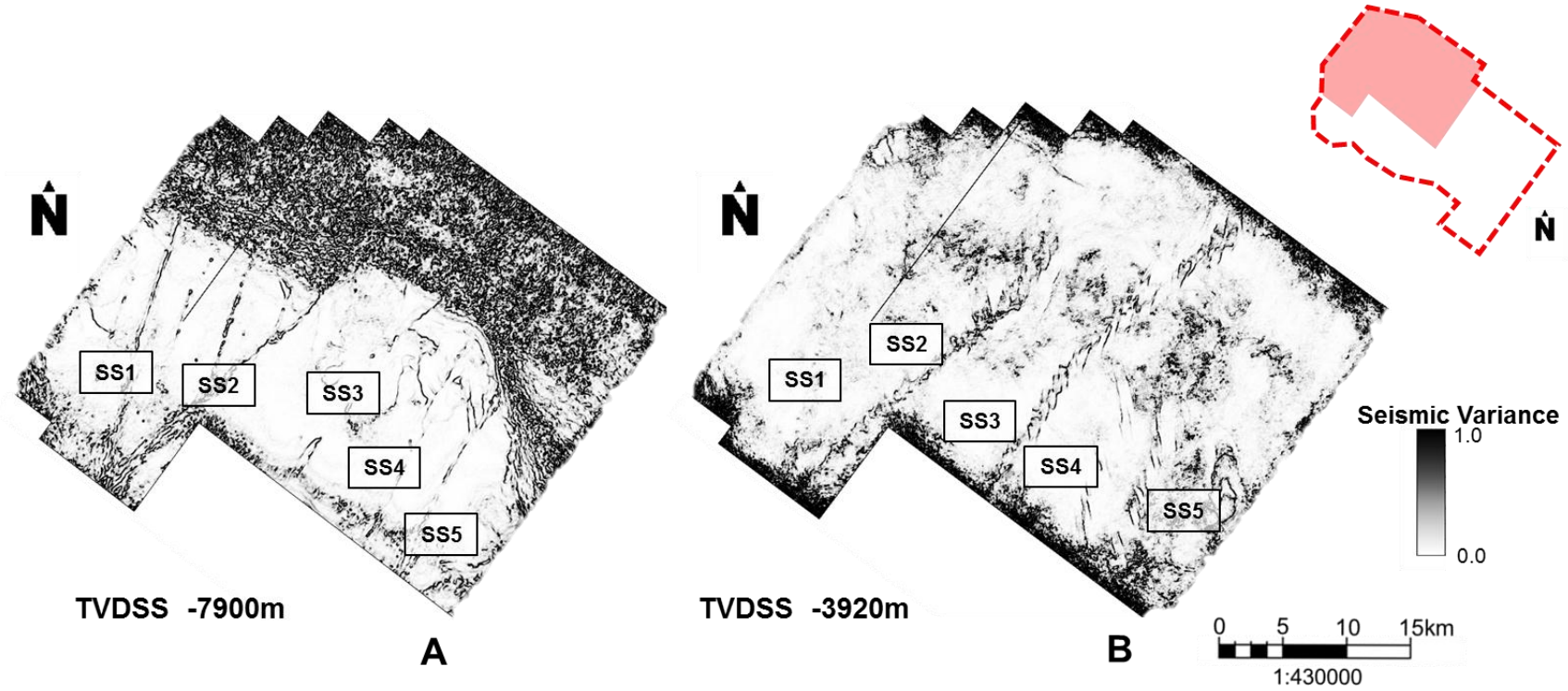

Figure 15: Variance depth slices extracted at different depths illustrating depth-dependent structure of left-lateral faults and strata. **A**- Variance depth slice at -7900 m TVDSS illustrating the planar geometry of strike-slip faults. **B**- Variance depth slice at -3920 m TVDSS showing arrays of en-echelon faults.

Lateral displacement of left-lateral strike-slip faults

Seismic amplitude and variance depth slices from -5300 to -4800 m TVDSS (Early to the Middle-Late Ordovician) show that strike-slip faults offset NW- striking Ordovician fault systems and reef deposits, revealing that strike-slip faults experienced left-lateral motion (Figure 12 and 16).

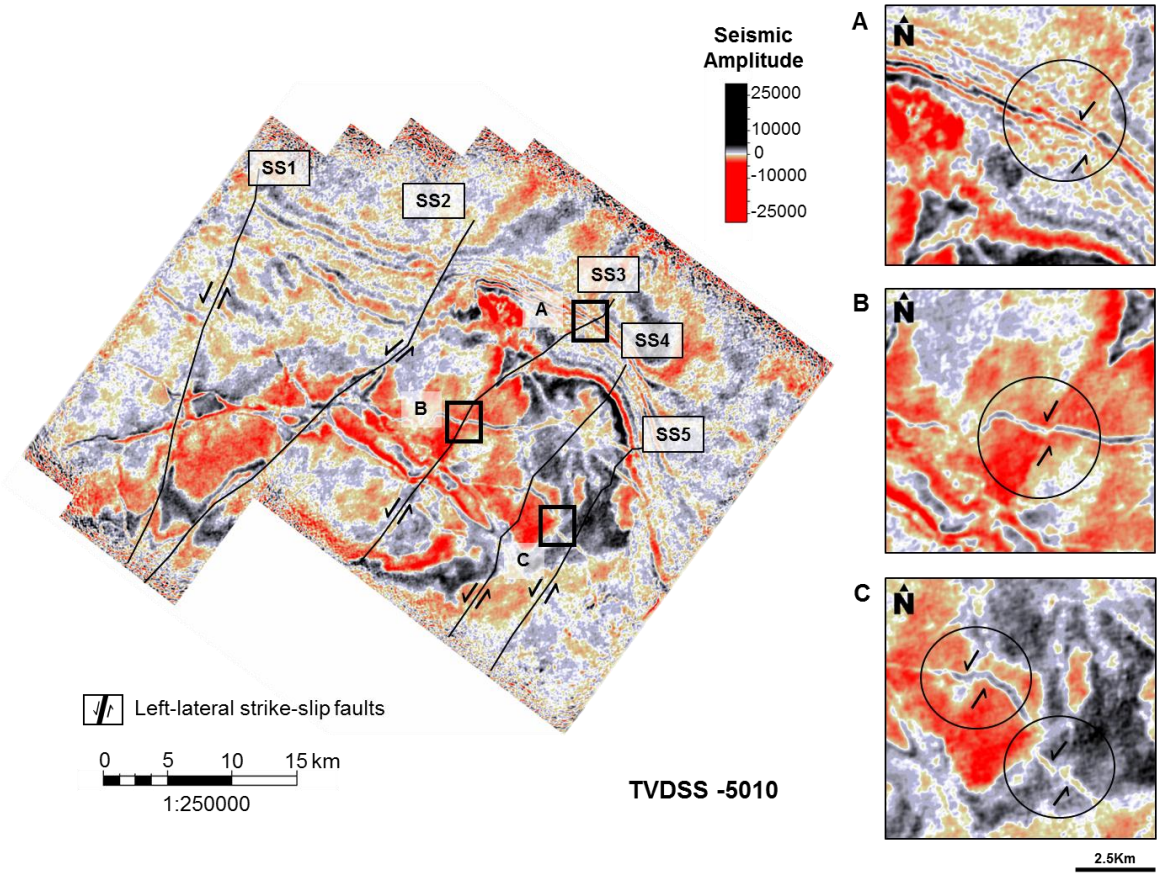

Figure 16: Seismic amplitude depth slice at -5010 m TVDSS illustrating the sense and magnitude of displacement of strike-slip faults. The lateral offset of seismic reflectors indicates the strike-slip faults experienced left-lateral separation. The magnitude of strike separation was directly estimated from the depth slices.

Strike-slip faults intersect T1 as well as numerous faulted reticulate reef deposits observed in Middle-Late Ordovician age strata (Figure 12), indicating that strike-slip faults potentially formed or reactivated after the development of Ordovician fault systems. The horizontal offset of stratigraphic and structural features (in map view) was particularly evident in faults SS3, SS4, and SS5 (Figure 16). The magnitude of lateral offset was directly estimated from the depth slices and ranges from 400 to 1720 m. The fault displacements are higher towards the south (continuing outside of the study area) and decrease towards the north.

Estimation of the formation time of strike-slip faults and evidence for reactivation of structures

The deeper, continuous portions of the strike-slip faults terminate above the Middle-Late Ordovician age strata and cross-cut stratigraphic features associated with reef growth, which indicates that strike-slip faults formed after the deposition of the Middle-Ordovician unit. Furthermore, even though some strike-slip faults are vertically displaced, there are not thickness variations within Cambrian and Ordovician strata which indicates the formation of the planar structures occurred after the Middle to Late Ordovician.

Shearing of preexisting fault planes and fractures can be accompanied secondary fracture propagation (Segall and Pollard, 1983; Martel and Boger, 1998). The shallower en-echelon arrays of faults that diverge from the principal displacement zone propagate near the boundary between the Late Ordovician and Silurian formations. In some cases, segments of the strike-slip faults extend to Carboniferous and Permian strata due to reactivation of the structure during sediment collapse or volcanic activity (Figure 17). Based on the geometric differences between the planar portion and the en-echelon arrays, as well as the different offset characteristics between the faults,

it is proposed that secondary faults likely formed to accommodate displacement of the strike-slip faults in a later period than the period of activity that formed the deeper, main displacement zones.

All the strike-slip faults zones observed in this region display consistent attitudes and the same geometric pattern of steeply dipping lower vertical strike-slip faults that open upward in a series of en-echelon faults. The different geometries of strike-slip faults result of markedly different tectonic regimes associated with pure strike-slip motion and a component of extension (Christie-Blick and Biddle, 1985; Sylvester, 1988), suggesting that formation time of the planar portion of the strike-slip faults could be different than the formation time of the upward diverging en-echelon faults.

Permian-Triassic normal faults

Seismic data were used to analyze the architecture and the temporal and spatial distribution of volcanic features formed in the Tazhong Uplift. Seismic data reveals that Carboniferous and Permian strata are substantially deformed as a result a variety of extrusive volcanic events and collapse structures associated with volcanism (Figure 17).

Geometry and seismic character of volcanic bodies

Volcanic bodies have been identified and characterized on the basis of seismic reflection data, and a suite of geometric attributes such as: coherency (variance), curvature, and dip azimuth and magnitude. Volcanic deposits were identified in seismic data on the basis of chaotic reflector geometries, variable amplitudes, and anomalous impedances (Hansen and Cartwright, 2006; Thomson, 2007; Infante- Paez and Marfurt, 2017; Infante-Paez, 2018).

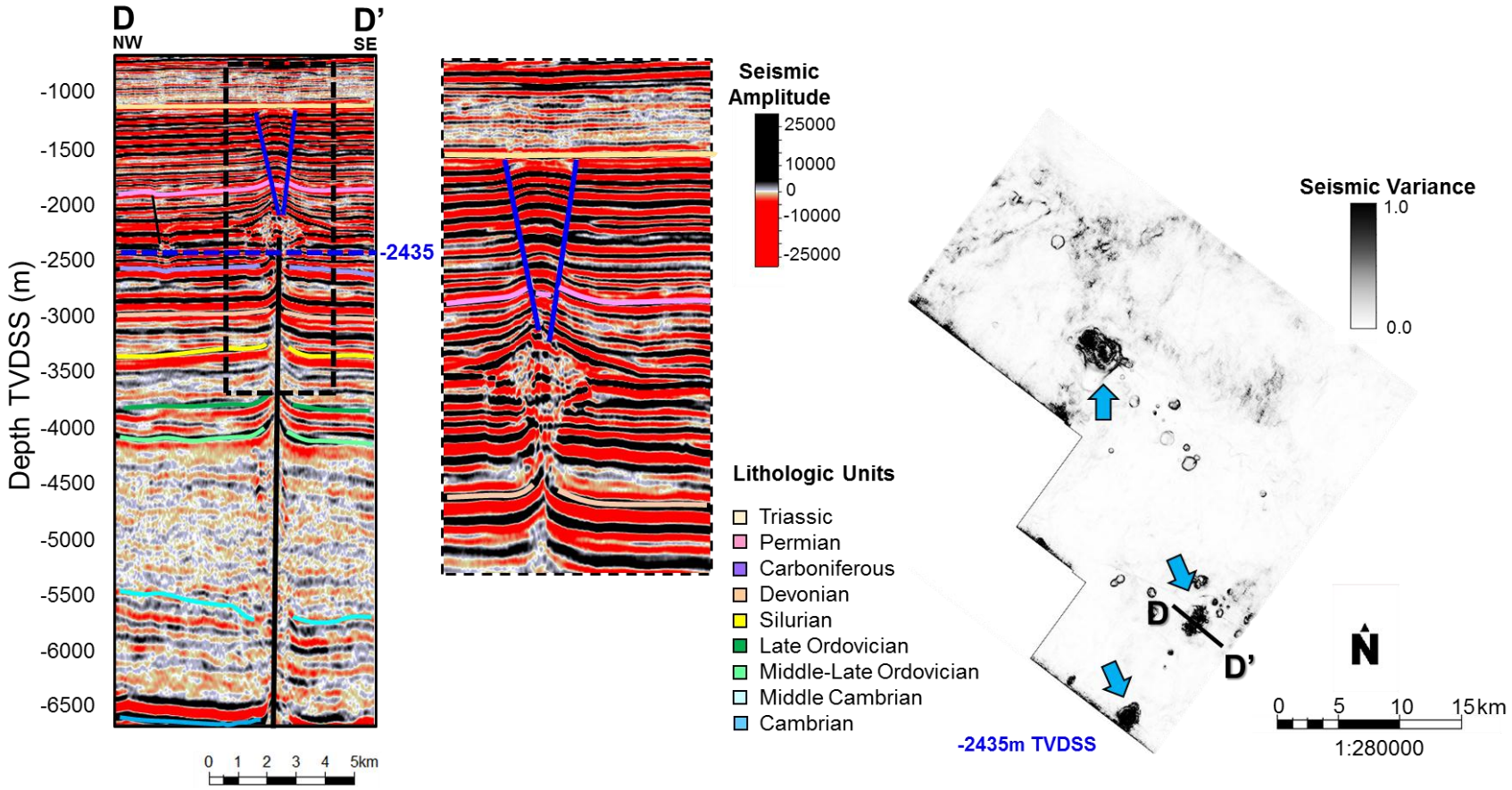

Figure 17: Structure of a volcanic bodies in seismic profile and map view. The left panel displays a seismic amplitude profile (D-D') showing a strike-slip fault SS12 (black line) directly below a volcanic extrusion and Triassic normal faults (blue lines) above the volcanic edifice. Note that the strike-slip fault served as a path of penetration for the igneous body. Middle Cambrian to Permian formation tops are color coded. The right panel is a depth slice of seismic variance at -2435 TVDSS that displays three of the Permian extrusions (indicated by the blue arrows) and numerous smaller collapse features adjacent to the volcanic bodies.

Six volcanoes with distinctive crater-type morphology were identified in this study (Figure 17). The volcanoes display an elliptical or sub-circular geometry in map view (Figures 17 and 18). The volcanic bodies exhibit diameters ranging from 2500 up to 4500 m and reliefs of 800 to 1300 m. In seismic profiles the igneous bodies are characterized by a dome shaped structure underlain by a wide (>1600 m) funnel-shaped vertical pipe that penetrates deep in the subsurface (>5000 m; Figures 17 and 18). Inside the extrusive body, amplitude reflections are chaotic showing complex networks of discordant and concordant amplitudes (Thomson, 2007; Infante and Marfurt, 2017; Infante,2018). Although the igneous bodies are present within Permian strata, the volcanic edifices have also disrupted and deformed pre-existing sediments along the inferred vertical flow path of melt (Figures 17 and 18).

There is a sharp contrast between the volcanic edifice geometry and the surrounding formations which display laterally continuous reflections. Seismic reflectors onlap or terminate against the volcanic edifice (Figure 18). Stratal wedges are found in the limbs of the volcano indicating extrusive activity rather than the emplacement of a magmatic intrusion (Figure 18). Based on seismic data observations, it is concluded that igneous extrusive bodies were deposited before late Permian and Triassic sedimentation took place. The strata above the volcanic bodies is folded and heavily faulted (Figure 17 and 18).

Concentric and radial normal faults displacing Permian and Triassic age sediments (50 to 250 m) are evident at the crest and the peripheries of the volcanoes (Figures 17). It is likely that these faults developed due to local stress perturbations.

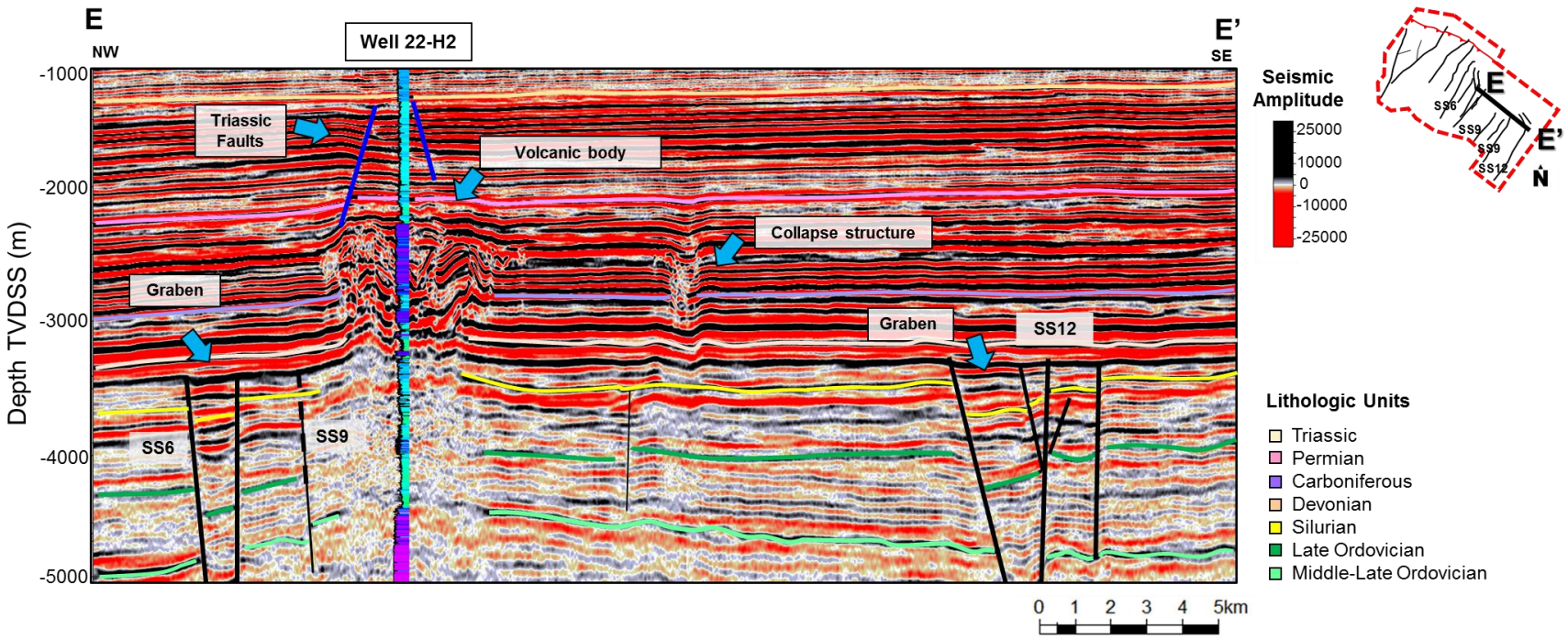

Figure 18: Interpreted seismic profile (E-E') illustrating the structure of a volcanic deposits and a collapse feature. The volcanic extrusion covers an area of approximately 4700 m^2. The sub-structure of the volcano appears as a series of disturbed and chaotic seismic reflectors above the penetration pathway characterized by low amplitude reflections. Collapse feature appears to the right of the volcanic body. Left-lateral strike-slip faults and grabens are marked with thick black lines and secondary faults with thin black lines. Middle Ordovician to Triassic formation-tops are color coded.

Geometry and character of collapse features

Carboniferous and Permian sediments are deformed by a series of collapse features that, due to their distribution and proximity, appear to be associated with volcanic activity (Figure 18). Collapse features are observed within Carboniferous and Permian deposits. However, these structures show a different seismic response than the volcanic edifices. Unlike volcanic deposits, these features reflect the structural collapse of the enclosed strata, are significantly smaller, do not display a disturbed path of penetration, and seismic amplitudes are not discordant (Figures 18). Faults associated with collapse features are circular in map view and also display normal separations of up to 250 m. In contrast with faulting associated with Permian volcanoes, structural collapse affects Carboniferous and Permian strata. Considering that the Carboniferous is a carbonate dominated unit, structural collapse could be generated as a result of dissolution driven by magmatic steam off gassing.

Spatial distribution of volcanic bodies and collapse structures and implications on fault reactivation

Six volcanic extrusions have been identified in this investigation. The igneous extrusions cover a significant portion of the south (ZG8-43 and TZ45 South) and are nearly absent towards the northeast region (TZ45). The distribution of the volcanic deposits suggests that the magma preferentially intruded into pre-existing faults (Figure 17). The Permian age volcanic bodies and collapse structures trend in two distinctive orientations: NW and NE, and they appear to be preferentially distributed along several strike-slip faults (Figure 17). In seismic profiles, it is observed that segments of certain strike-slip faults are vertically linked with volcanic features and collapse features, which indicates strike-slip faults served as magma flow conduits and were

potentially reactivated by the volcanic activity (Figure 17). Triassic normal faults associated with Permian igneous bodies and Carboniferous-Triassic structural collapse features are an example of the significance of pre-existing structures in the occurrence and distribution of subsequent deformation and igneous edifices.

Drilling induced deformation of wellbores

Observations of borehole wall failure and determination of stress orientation

FMI logs are limited to a portion of the Ordovician formation; most initiate at the top of the Lianglitage Formation and extend up to 500 m to the Yijianfang or Yingshan Formations, which are typically about 6000-6500 m MD. Even though borehole breakouts were detected in all thirteen wells, DITF are not as common and abundant as breakouts.

A significant portion of the image logs for each borehole are compromised by poor data quality, which prevented identification of breakouts and DITF. In general, there were six tracks present in each borehole image. However, one or more tracks appeared blank in certain wells and, in some cases, the artifacts constituted the majority of the log for some wells. For each well, the cumulative length of borehole breakouts is compared to the cumulative length of areas where no breakouts were present to areas were the image quality was poor and uninterpretable. A detailed analysis of borehole wall failures in three representative wells follows:

Well 15

Well 15 displayed both borehole breakouts and drilling induced tensile fractures (Figure 19). Borehole breakouts were detected almost continuously from 5950 to 6114 m (MD). This depth interval corresponds to the Middle-Late Ordovician Liangliatge formation. The breakouts are

continuous and extend up to 20 m long. There are significantly fewer and sporadic breakouts at depths greater than 6150 m (within the Yijianfang formation) (Figure 19). The orientation of breakouts is consistent over the length of the vertical hole, averaging 325° ± 4° and indicating that the maximum principal stress (S_{Hmax}) is directed 055° ± 4°. The widths of the breakouts did not change significantly with depth, averaging 43° ± 5°. In this well, DITF were observed at a depth of 6140 m (MD) and appeared as pairs of symmetrical, vertical, and continuous features (Figure 19). The orientation of the maximum horizontal stress (S_{Hmax}) obtained from DITF is 058° ± 5° indicating the orientation of the least principal horizontal stress (S_{hmin}) is 328 ± 5°. These results are consistent with the observations of borehole breakouts.

Well 11

Borehole breakouts in well 11 showed similar characteristics as those in well 15 (Figure 20). Most breakouts are concentrated within the Lianglitage Formation at depths ranging from 6150-6260 m and 6300-6350 m (MD). Significantly fewer breakouts are present within the Yijianfang and Yingshan formations. Borehole breakouts indicate that the minimum principal stress (S_{hmin}) orientation is 322° ± 2°, with no substantial variation in breakout orientation at depth. From borehole breakouts it is estimated that the orientation of the maximum principal stress (S_{Hmax}) is 052° ± 2°. The widths of the breakouts average 42° ±7°. The widths of the breakouts are relatively consistent. However, wider breakouts are more often present within the Lianglitage formation than those observed at lower units. No drilling induced tensile fractures were observed in well 11.

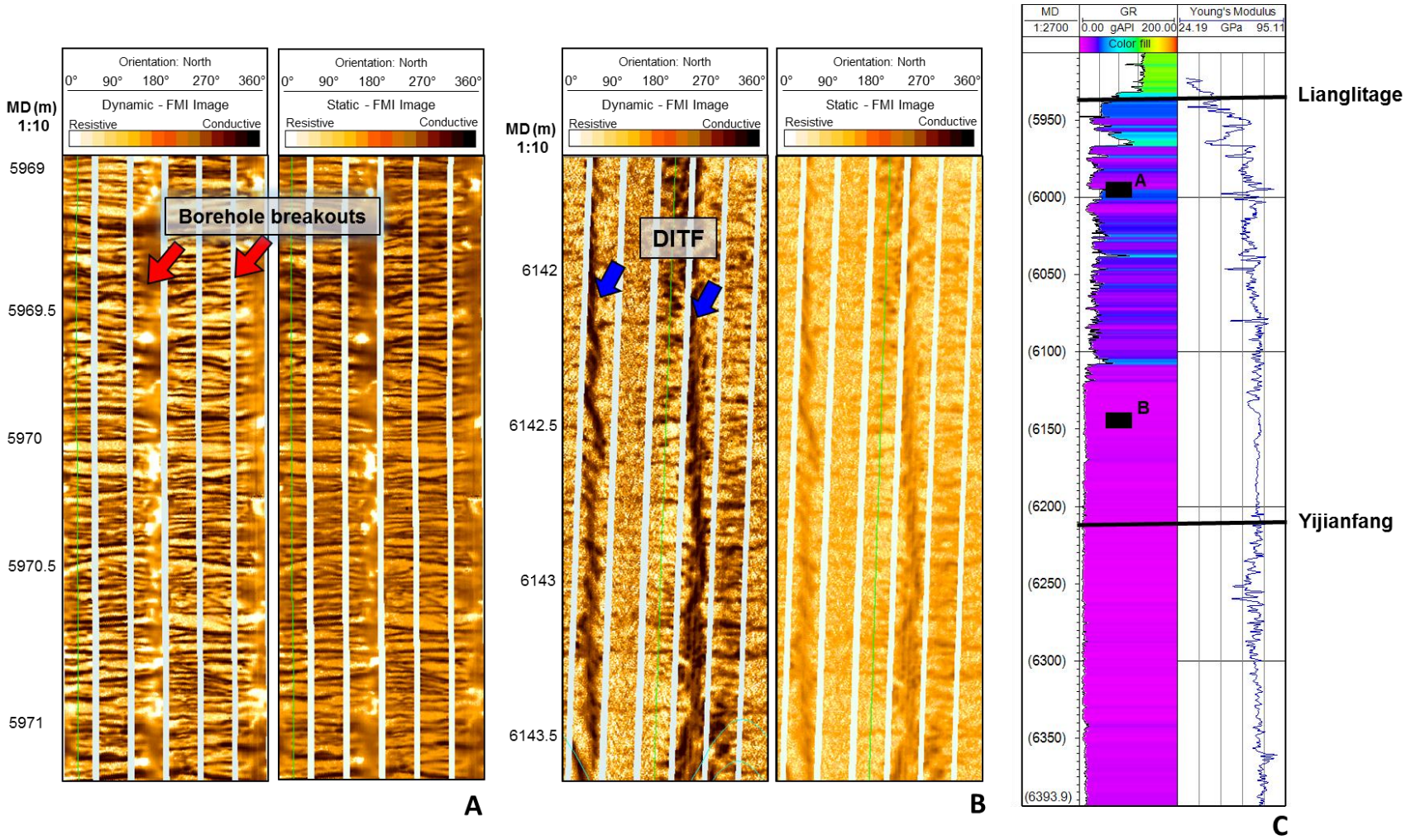

Figure 19: Example of borehole images from well 15 illustrating breakouts and DITF within the Lianglitage Formation. **A**- Unwrapped resistivity image showing the presence of borehole breakouts at 5969 m MD. **B**- Unwrapped resistivity image showing DITF at 6141.5 m MD. **C**- Gamma ray and Young's modulus logs from well 15 displaying the location of the two images. Log illustrates changes in elastic properties and lithology from mudstone (blue) to pure limestone (purple).

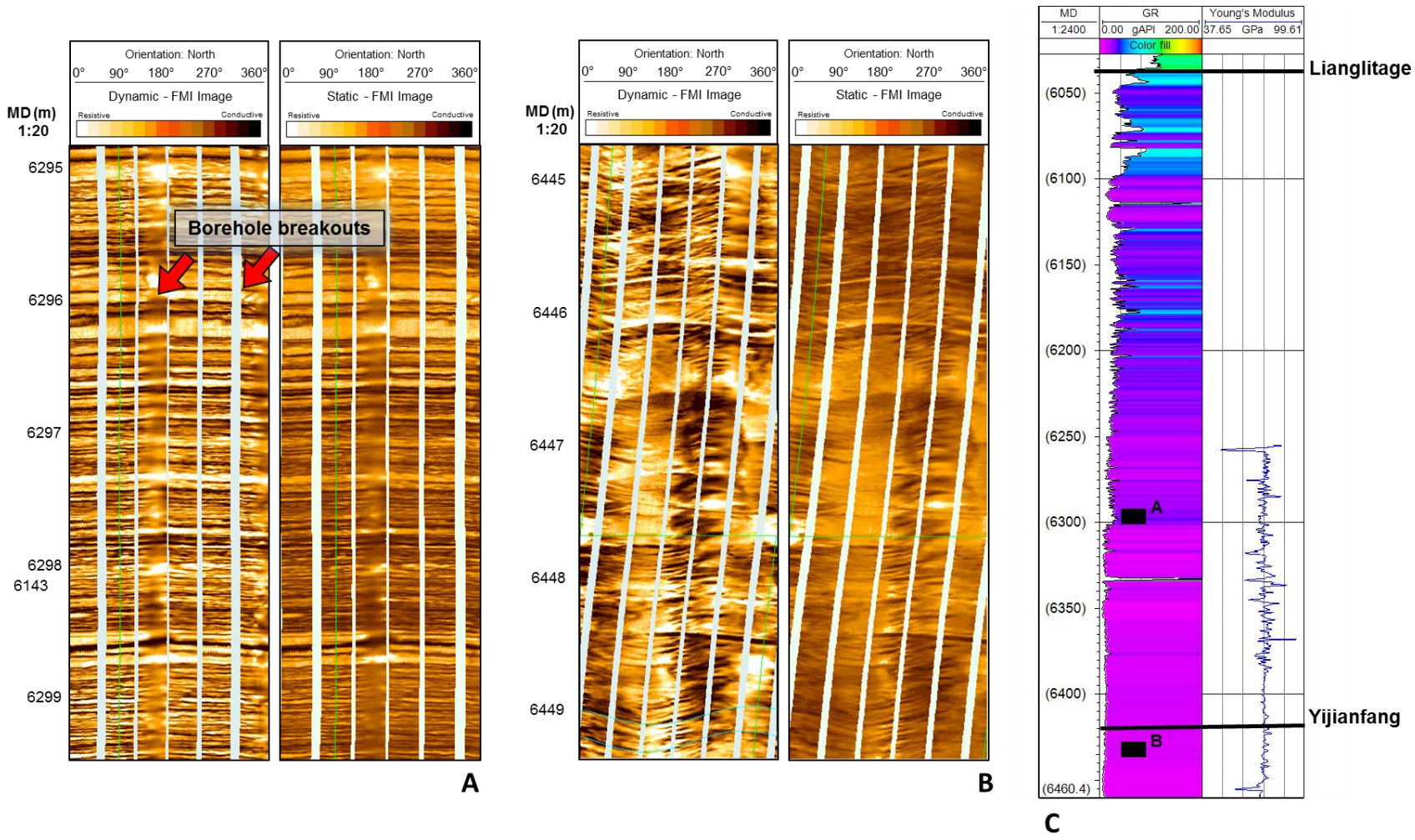

Figure 20: Example of borehole images from well 11 illustrating borehole breakouts. **A**- Unwrapped resistivity image showing the presence of borehole breakouts at 6295 m MD within the Lianglitage Formation. **B**- Unwrapped resistivity image showing the lack of breakouts and DITF at greater depths. **C**- Gamma ray and Young's modulus logs from well 11 displaying the location of the two images. Log illustrates changes in elastic properties and lithology from mudstone (blue) to pure limestone (purple).

Well 26

Well 26 exhibits borehole breakouts at depths between 6110 to 6250 m (MD) (Figure 21). There are no significant variations in the azimuth or width of breakouts with depth. The average azimuth of breakouts is 346°± 5° indicating that the minimum principal stress (S_{hmin}) orientation is 346°± 5° and the maximum horizontal stress orientation is 076°± 5°. The average width of borehole breakouts is 41° ± 6°. As observed in wells 15 and 11, the majority of breakouts are within the Lianglitage formation (Figure 21). No drilling induced tensile fractures were observed.

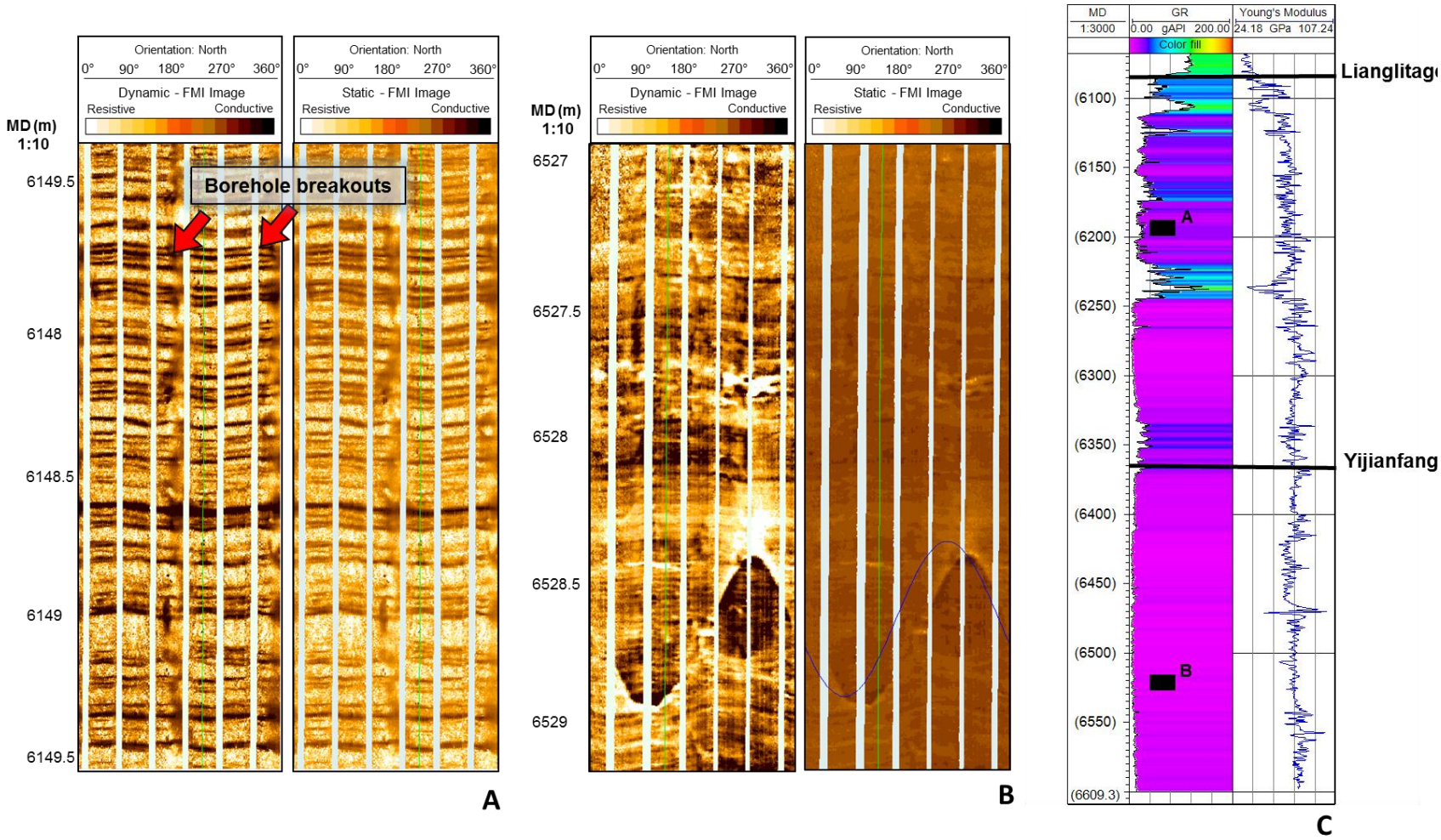

Figure 21: Example of borehole-images from well 26 illustrating borehole breakouts. **A**- Unwrapped resistivity image showing the presence of borehole breakouts at 6149.5 m MD within the Lianglitage Formation. **B**- Unwrapped resistivity image showing the lack of breakouts and DITF at greater depths and the presence of natural fractures. **C**- Gamma ray and Young's modulus logs from well 26 displaying the location of the two images. Log illustrates changes in elastic properties and lithology from mudstone (blue) to pure limestone (purple).

Stress orientation interpretation

While borehole breakouts were observed in all wells containing FMI data, drilling induced tensile fractures were only observed in a few wells. Borehole breakouts were extensive and continuous in some wells and shorter and sporadic in other wells. Overall, the borehole breakouts are common, but not ubiquitous, in the Lianglitage Formation (shallower depths). Borehole breakouts were also observed in lower units (Yijianfang and Yinshan formations) but in lower abundances and, in some cases, these were narrower than breakouts observed in the upper unit.

The orientations of borehole breakouts were consistent for all wells aside from well 15-2 and 163, which showed radically different orientations or relative magnitudes (Figure 22). In general, the azimuth of breakouts is 331° ± 7° (1 excluding wells 15-2 and 163; Figure 22).

Wells 163 and 15-2 have anomalous stress orientations (Figure 22). In well 163 S_{Hmax} is oriented more northerly than the rest of the wells in the field. In well 15-2 the relative orientation of the principal horizontal stresses is similar to the rest of the wells but opposite in relative magnitude (Figure 22). Wells 163 and 15-2 displayed similar drilling parameters (such as pore pressure and formation temperature) than the surrounding wells. It was observed that both wells are adjacent to complex structures. Well 163 was drilled over a dome-shaped structure associated with reticulate coral-reefs and bounded by secondary Ordovician faults. Well 15-2 is adjacent to an Ordovician fault and a graben located around 1200 m from the well (Figure 22). The orientation of S_{Hmax} in well 15-2 appears aligned with the trend of the graben and fault strike. The graben offsets Ordovician to Devonian sediments more than 500 m.

It is likely that the stress deviations observed in wells 163 and 15-2 are caused by local perturbations of the stress field due to the proximity to complex structural features. Furthermore,

the lithologic contrast between the location of the wells and surrounding areas could also be contributing to the difference in stress orientation. For example, well 15-2 is located next to Silurian strata (due to the graben offset). The contrast in mechanical properties between Ordovician carbonate sediments and Silurian siliciclastic sediments could generate a local discrepancy in the stress magnitudes and orientations conveyed across the fault to the Ordovician carbonate unit.

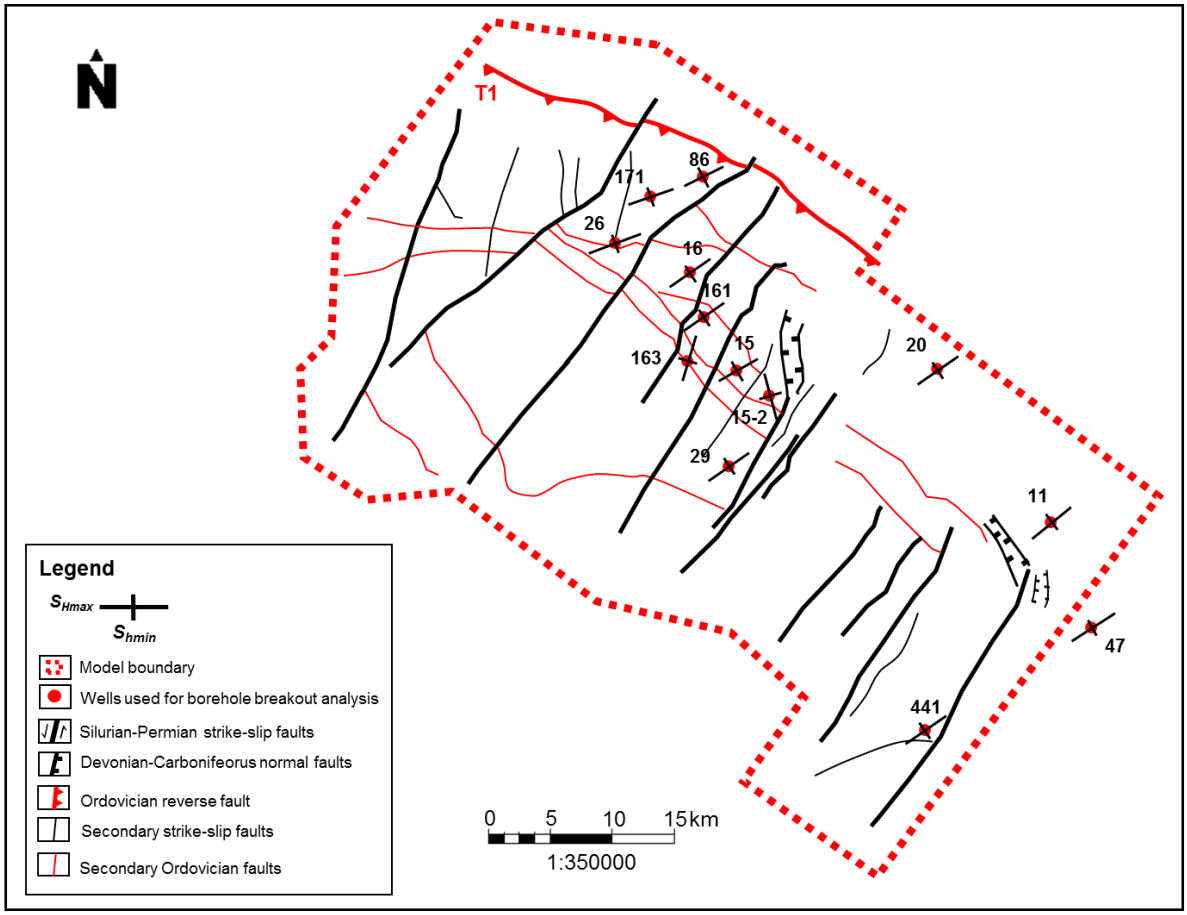

Figure 22: Map of the orientation of the minimum and maximum principal stresses derived from borehole wall failure and relationship to major faults on the study area. The map indicates the maximum horizontal stress is typically oriented northwest with exception of wells 15-2 and 163.

Principal stress orientation measurements obtained from borehole breakouts and drilling induced tensile fractures reveal that within a particular stress regime, the orientation of in situ stresses do not change significantly with depth. The orientation of breakouts and drilling induced tensile fractures (if observed) are constant with depth for all wells. The widths of breakouts are also consistent with depth. Wider breakouts (than average width) were observed at upper units in only a few wells. Table 6 summarizes the average breakout azimuth and width for each well.

Table 6. Azimuth of borehole breakouts and DITF, and borehole breakout widths for all wells.

Well	Depth range [m]	Breakout azimuth	DITF azimuth	Breakout width
86	6402-6645	330° ± 8	085°±15	46° ±9
11	6258-6777	322° ± 2	-	42°±7
15	5950-6620	325° ± 4	058°±5	43° ± 5
15-2	5947-6221	260° ± 6	-	46° ± 6
16	6360-6632	324° ± 7	-	47° ± 9
161	6042-6288	338° ± 6	063°±6	39° ± 6
163	6154-6354	294° ± 7	-	49° ± 6
171	6245-6475	342° ± 4	-	42° ± 8
20	6415-6768	321° ± 2	-	46° ± 2
26	6095-6522	346° ± 5	-	41° ± 6
29	5902-6323	334° ± 9	-	43° ± 6
441	5415-5525	335° ± 5	-	42° ± 8
47	5826-6143	331° ± 6	063°± 3	41° ± 5

The presence of breakouts seems to be lithologically controlled. Well-log data, specifically gamma ray and sonic log, reveal that there is a lithologic contrast between the Lianglitage and Yijianfang and Yinshan Formations (Figures 19,20, and 21). The Lianglitage Formation is characterized by reef and intertidal deposits consisting of laminated carbonate mudstones and limestone. Gamma ray response varies from 25 to 100 API within the carbonate rich mudstone intervals (upper intervals) and from 10 to 25 in limestone intervals (lower units; Figures 19, 20,

and 21). On other hand, the Yingafang and Yingshan Formations consist of more pure limestone and dolomite. Gamma ray log is constant (3-10 API) and indicates the formation contains few radioactive minerals (Figure 19,20, and 21).

The correlation between breakouts and lithology suggest that breakouts are abundant in areas with higher clay content and sporadic in intervals of "pure" limestone and dolomite. There is a general trend of increasing clay content within the Lianglitage formation towards the south-east of the Tazhong Uplift. It was observed that wells with lower clay content in the Lianglitage formation displayed lower amounts breakouts. The absence of breakouts also seems to be correlated with high fracture density. It was often observed that the lack of breakouts was related to the presence of natural conductive fractures (Figure 21).

DISCUSSION

Deformation events, fault reactivation and paleostress in the Tarim Basin

The Tarim Basin underwent a complex tectonic evolution that involved the formation of Paleozoic and Mesozoic fault systems, emplacement of volcanic bodies in the Permian, and the localized structural collapse of Carboniferous, Permian, and Triassic strata. Three fault systems have been identified on the basis of seismic data interpretation: Ordovician reverse faults, Silurian–Permian strike-slip faults, and Carboniferous-Triassic normal faults (Figure 9).

A primary NW-striking reverse fault and a series of secondary Ordovician faults have been identified in the study area (Figure 9). Through forward kinematic modeling of fault trajectory, it is proposed that the T1 fault developed a fault-propagation fold during the Middle to Late Ordovician (Figure 11). Even though no crystalline basement is observed in the seismic volumes analyzed in this investigation, by fitting the main fault geometry with pre-growth and growth horizons, the fault trajectory and fault displacement can be accurately determined (Eichelberger et al., 2015). The structural model suggests that the fault-plane dip is constant into the basement, with no evidence for a listric geometry at depth (Figure 11). Furthermore, thickening of the hanging wall below the Middle Cambrian unit suggests the T1 fault inverted and developed from reverse slip a pre-existing, Middle Cambrian, normal fault (Figure 11).

Several authors have suggested that the main reverse fault T1 has been reactivated from basement structures based on paleomagnetic data (Li et al., 2012; Lin et al., 2012). Rifting and brittle extension of the crust in the Late Proterozoic and Early Paleozoic promoted the development of normal faults and half grabens in the southern and central areas of the basin (Li et al., 2012; Yuzhu and Zhihong, 1996). The Tarim Basin became an active convergent margin in the Early

Ordovician due to the subduction of the Tarim Block under the Kunlun Block, and this change in tectonic setting is a potential driver for tectonic inversion observed in the Tazhong Uplift (Figure 3; Li et. al, 2012; Li et al., 2013; Lan et. al, 2014; Han et. al 2017).

Crustal shortening in the NE direction (perpendicular to T1) caused the development of the NW-striking faults, including the major fault propagation fold (T1) and minor faults associated with reticulate reef growth (Figure 10). In agreement with interpretations of previous studies (Li et al., 2012 and Lin et al., 2015), the tectonic transition from divergence to convergence likely promoted the inversion of the main reverse fault T1. Given the reactivation of normal faults striking NW as reverse faults on the same fault plane, there would not be a change in the principal stress directions between the earlier horizontal extension (rifting) and subsequent horizontal shortening, but a change in the relative magnitudes where the vertical stress S_v changed from being the maximum principal stress (σ_1) to the minimum principal stress (σ_3). If the stress orientations had changed, oblique strike-slip faults would be expected on the reactivated basement normal fault.

Strike-slip faults have been extensively studied in the Tazhong Uplift (Li et al., 2013; Lan et. al, 2014; Han et. al 2017). However, the formation time and evolution of these structures has been debated. The majority of the strike-slip faults deform Cambrian to Devonian deposits, while some extend upward to deform Carboniferous and Permian age strata. The strike-slip faults display two characteristic geometries: NE-striking vertical planar structures in the Cambrian to the Middle-Late Ordovician and N-striking subvertical en-echelon arrays displaying normal separations in the Late Ordovician to Carboniferous (Figure 13). Based on the geometry, thickness estimation, and cross-cutting relationships, it is proposed that strike-slip faults developed in two phases. The vertical faults formed prior the deposition of the Late Ordovician (Sangtamu Formation) but after the deposition of Middle-Late Ordovician (Lianglitage Formation). Segments

of the strike-slip faults cross-cut the Middle-Late Ordovician units and offset the Late Ordovician T1 reverse fault and Middle-Late Ordovician reef deposits, indicating that strike-slip faults were active after the deposition and shortening of Early and Middle Ordovician sequences. The lack of thickness variation associated with strike-slip deformation within Cambrian to Late Ordovician units further supports the relative timing proposed above.

The continental collision between the Kunlun plate and the Tarim block in the Late Ordovician and the closure of the Tianshan ocean in the Carboniferous, caused the uplift of bounding mountain ranges (Figure 3; Lan et. al, 2014; Han et. al 2017). N-directed horizontal shortening likely led to the formation of strike-slip faults in the study area and the creation of right-stepping en-chelon faults and pull-apart basins during the Silurian, Devonian, and Carboniferous (Figure 14).

Based on the geometry and mechanisms of secondary fracture propagation, it is proposed that en-echelon arrays formed in a different geologic time than the main displacement zone. The older planar and continuous strike-slip faults would form in a strike-slip setting with the intermediate principal stress (σ_2) as the vertical stress S_v, and the maximum principal stress (σ_1) at horizontal about 30˚ from the fault plane, i.e,, nearly to the north. The later stage of movement on the strike-slip faults, when the en-echelon arrays formed, also result from a strike-slip tectonic regime, but with σ_1 about 15˚ further west (i.e. NNW), sufficient at reactivating the deeper fault segments but forming en-echelon shears above.

Continent-continent collision continued during the Carboniferous and Permian. A mantle plume generated upwelling of magma and the eruption of multiple volcanoes in the Central Tarim Basin (Figure 3; Yang et al., 2007, 2015). In previous studies (Yang et al., 2007, 2015) it was also observed that segments of strike-slip faults were used as conduits for Permian volcanism (Figure

17). Magma preferentially penetrated particular strike-slip faults segments. Magmatic activity promoted the reactivation and propagation of strike-slip faults into Carboniferous and Permian strata. There is also a preferential distribution of volcanic edifices and collapse structures along the pre-existing strike-slip faults (Figure 18). The presence of volcanic bodies and collapse features have also controlled the mechanical response of overlying sediments. Permian and Triassic normal faults are oriented along the crest and perimeters of the volcanic extrusions (Figure 17 and 18). Similarly, structural collapse generated a series of circular normal faults in Carboniferous, Permian, and Triassic strata. While the majority of these faults are restricted to the vicinity of the igneous bodies and collapsed sediments, some faults propagate for longer distances. Triassic faults also appear to be preferentially oriented in a similar direction as the pre-existing strike-slip faults.

On the basis of this investigation, the formation of the normal faults resulted from the interaction between the stress field and local stress perturbations. Triassic normal faulting occurred when S_v was the maximum principal stress (σ_1). Given the presence of strike-slip faults in older strata, the magnitude of *Sv* must have changed from the intermediate stress (during strike-slip faulting) to the maximum principal stress.

The Tarim Basin evolved to the present-day configuration after the Himalayan orogeny. The Indo-Asian collision led to shortening and escape tectonics (Molnar and Tapponnier 1975; Morley, 2002) during the Late Cenozoic causing the rapid uplift of the Tian Shan, Kunlun Shan, and Altyn Shan orogenic belts and stimulated rapid subsidence of the basin foredeeps (Jia et al.,1998; Sun et al., 2017). The reactivation of tectonic activity 50-55 Ma generated major fault systems in the region including the Altyn and Aheqi fault zones which bound the basin to the southeast and northwest respectively (Jia et al.,1998).

Determination of in situ stress magnitudes in the Central Tazhong Uplift

The orientations of in situ stress in the Central Tazhong Uplift determined from borehole breakouts and DITF document the minimum horizontal stress (S_{hmin}) is generally directed northwest (331° ±7.2°) and S_{Hnax} is northeast (061° ±7.2°) except for wells 163 and 15-2 (Figure 22 and 23).

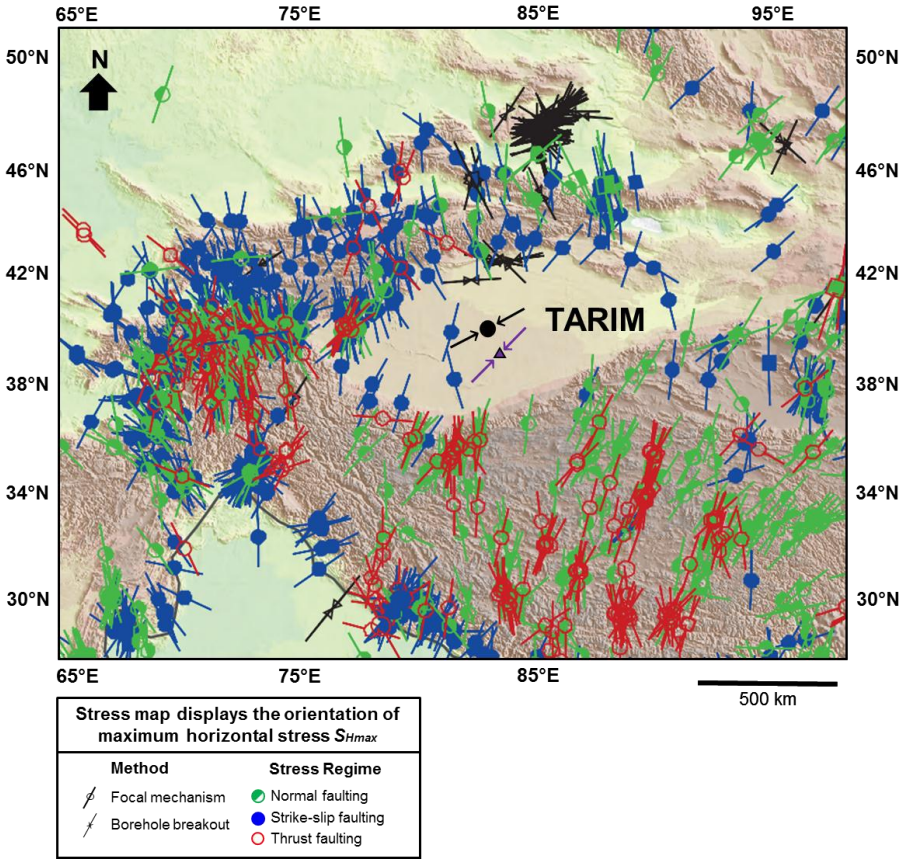

Figure 23: Comparison of the inferred in situ stress state in the Central Tazhong Uplift (this study), results from Sun et al. (2017), and other determinations cataloged by the World Stress Map Project (http://www.world-stress-map.org/casmo/). The orientation of S_{Hmax} determined in this study is indicated by the black dot and arrows. The orientation of S_{Hmax} obtained by Sun et al. is indicated by the purple arrows. The map shows the crustal present-day stress field since 2009, which is largely determined from analysis of earthquake focal mechanisms.

The current situ stress orientations are not consistent with the paleostress states in the Tarim Basin during Phanerozoic tectonic events. The most obvious manifestation of the change in stress is that the sense of slip of the Paleozoic left-lateral strike-slip faults cutting the Central Uplift are opposite to the right-lateral shear imposed by the the current orientation of S_{Hmax} and S_{hmin}; if the pre-existing strike-slip faults were activated by current stress, they would displace in a right-lateral sense.

The magnitudes of the in situ stress at depth in the Central Tazhong Uplift may be determined using information of overburden, fluid pressures, conditions in the borehole while drilling, rock strength, the presence of DITF and breakouts, and the breakout angular widths (Zoback et al., 1985; Zoback et al., 2003; Chang et al., 2010; Sun et al., 2017). Here, the total vertical stress (S_v) is determined from the overburden by integrating the density from the surface to the depth of interest. The vertical stress is given by:

$$S_v = \int_0^z \rho(z) g \, dz \tag{2}$$

where ρ(z) correspond to the rock density as a function of depth, and g is the gravitational acceleration. Density logs were made available only for portion of the Ordovician section; however, the CNPC reports indicate that an average density of 2.4 g/ cm^3 may be assumed for the depth interval above the Ordovician to calculate S_V.

The magnitudes of the far-field S_{Hmax} and S_{hmin} may be determined from breakouts and DITF based on the local stress at the borehole wall and the strength of the rock. Stress concentrations around a vertical well, in an isotropic, elastic medium are modeled using cylindrical

coordinate system and the Kirsch equations, which are derived assuming homogeneous, isotropic, linear elasticity (Zoback et al., 1985; Zoback et al., 2003). The magnitude of the principal stresses at the borehole wall vary with position (θ) as given by:

$$\sigma_{\theta\theta} = S_{hmin} + S_{Hmax} - 2(S_{Hmax} - S_{hmin})Cos2\theta - P_p - (P_m - P_p) - \sigma^{\Delta T} \quad (3)$$

$$\sigma_{zz} = S_v + 2\nu(S_{Hmax} - S_{hmin})Cos2\theta - P_p \quad (4)$$

$$\sigma_{rr} = (P_m - P_p) \quad (5)$$

where S_{hmin} and S_{Hmax} are the minimum and maximum horizontal stresses, θ is the angular coordinate measured from the S_{hmin} direction, ν is the Poisson's ratio, P_p is the pore pressure in the formation, P_m is the mud pressure, and $\sigma^{\Delta T}$ denotes thermal stresses caused by the temperature differential between the formation temperature and the mud temperature and thermal expansion coefficient, $\alpha^{\Delta T}$. Values for the parameters of mud pressure, formation pore fluid pressure, and thermal expansion coefficient are taken from the CNPC drilling reports (Table 7).

Borehole breakouts will form when the local stress concentration at the wellbore wall exceeds the strength of the rock (Zoback et al., 2003). In general, breakout failure involves shear fracture when $\sigma_{\theta\theta}$ exceeds the failure strength, which is often taken as the uniaxial compressive strength. As given by (3), the widths of borehole breakouts indicate the range of θ in which failure occurs, and thus from (3) one can define a relationship between S_{Hmax} and S_{hmin} given the breakout width, W_{bo}, and the failure strength:

$$S_{Hmax} = \frac{\left(C + 2P_p + \Delta P + \sigma^{\Delta T}\right) - S_{hmin}(1 + 2Cos2\theta_b)}{(1 - 2Cos2\theta_b)}$$
$$2\theta_b = 180 - W_{bo} \quad (6)$$

where C corresponds to the unconfined compressive strength, $2\theta_b$ represents the position of the at the edge of the breakout, P_p is the pore pressure, and ΔP is the difference between the formation pressure and mud pressure. As can be seen above, (6) gives a linear relationship between S_{hmin} and S_{Hmax} defining all possible stress value combinations that produce breakouts of a specified width.

A similar relationship may be derived from (3) for the stress conditions that can produce DITF. The condition for tensile fracture in the borehole wall is when the circumferential stress $\sigma_{\theta\theta}$ achieves the tensile strength, which is typically very small relative to compressive strength, and in practice may be assumed zero, i.e. when $\sigma_{\theta\theta} < 0$ (Figure 20). Thus, substituting zero for $\sigma_{\theta\theta}$ and taking $\theta = 0$ in (3) gives the relationship, also linear, between S_{Hmax} and S_{hmin}. In principal, if both DITF and breakouts are formed, then the relationships from DITF can serve as a limiting condition (maximum values) of S_{Hmax} and S_{hmin} to produce the observed breakouts, and if no DITF are present, then the relationship for DITF can serve as a limiting condition (minimum values) of S_{Hmax} and S_{hmin} to produce breakouts.

Anderson's theory of faulting provides an additional constraint on the magnitude of the far field stresses, S_{Hmax} and S_{hmin} assuming that the strength of the crust given by the Coulomb failure criterion is never exceeded for the three permutations of possible stress states represented by thrust, normal and strike-slip faulting (Figure 24; Anderson, 1942; Zoback et al., 2003; Chang et al., 2010). Conventionally, cohesion is assumed zero and the coefficient of sliding friction, μ, is the

proportionality between shear stress and normal stress. Based on this assumption, the limiting condition for stress in the crust may be expressed as:

$$\frac{\sigma_1}{\sigma_3} = \frac{S_1 - P_P}{S_3 - P_P} = \left[\sqrt{(\mu^2 + 1)} + \mu\right]^2 \quad (7)$$

Where σ is the effective stress and S the total stress. Assuming that the vertical stress (S_v) is one of the principal stresses as in Anderson's fault theory, (1) may be written for the failure condition in normal faulting, thrust faulting, and strike-slip faulting as:

Normal Faulting:
$$\frac{\sigma_1}{\sigma_3} = \frac{S_v - P_P}{S_{hmin} - P_P} \leq \left[\sqrt{(\mu^2 + 1)} + \mu\right]^2 \quad (8)$$

Thrust faulting:
$$\frac{\sigma_1}{\sigma_3} = \frac{S_{Hmax} - P_P}{S_V - P_P} \leq \left[\sqrt{(\mu^2 + 1)} + \mu\right]^2 \quad (9)$$

Strike-slip faulting:
$$\frac{\sigma_1}{\sigma_3} = \frac{S_{Hmax} - P_P}{S_{hmin} - P_P} \leq \left[\sqrt{(\mu^2 + 1)} + \mu\right]^2 \quad (10)$$

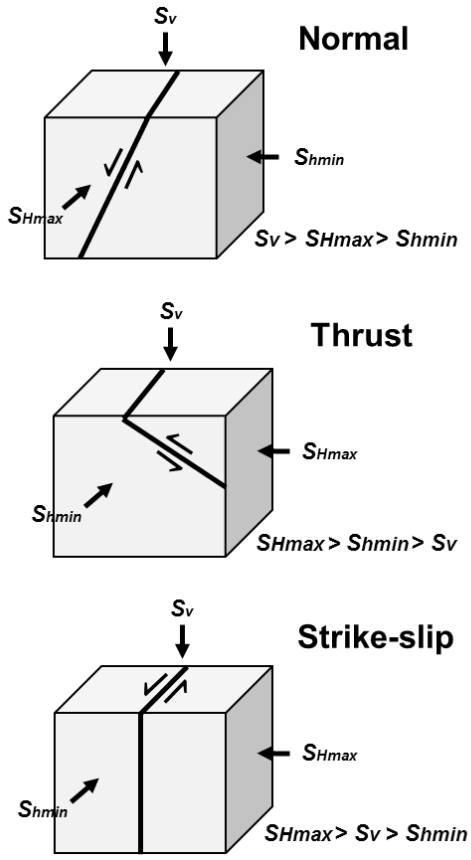

Figure 24: Diagram illustrating the Anderson's theory of faulting in terms of the orientation of relative principal stresses and the associated type of faults predicted for each stress state assuming Coulomb criterion for failure (Anderson, 1951). Note that per Anderson's theory, faults are expected to form at approximately 30˚ to the maximum stress direction and parallel to the intermediate stress direction; however, faults, once formed, may be reactivated by stress at different orientations if the sliding friction law (1) is satisfied (see text).

As shown by Anderson (1942) and Zoback (2010), the relationships (8-10) may be illustrated graphically in S_{Hmax} vs S_{hmin} plots along with the line $S_{Hmax} = S_{hmin}$ for a specified value of S_v to create the stress polygons bounding the possible far-field stress states in the crust, as well as indicate the stress states corresponding to thrust, normal and strike-slip faulting regimes (Figure 24).

Parameter values used in the analysis are presented in Table 7. In addition, the Young's modulus and UCS (unconfined compressive strength) was obtained from experiments conducted on representative samples of the Ordovician carbonates from the depths of the FMI logs analyzed herein (Figure 25). Poisson's ratio was derived from P-wave and S-wave seismic velocities, and the circulating mud temperature and formation temperature were obtained from drilling data, and the coefficient of thermal expansion was obtained from lab measurements by Sun et al. (2017).

Table 7. Parameters used to constrain the magnitudes of the S_{hmin} and S_{Hmax} for wells 15 and 26.

Well	Depth [m]	S_V [MPa]	Pp [MPa]	ΔP [MPa]	Breakout width [°]	Fluid temperature [°C]	Formation temperature [°C]	α_T [e^{-6}/°C]	E [GPa]	ν	μ
15	5969	143	70	2	45	58	130	7	58	0.3	0.6
26	6149	148	71	2	36	63	135	7	58	0.3	0.6

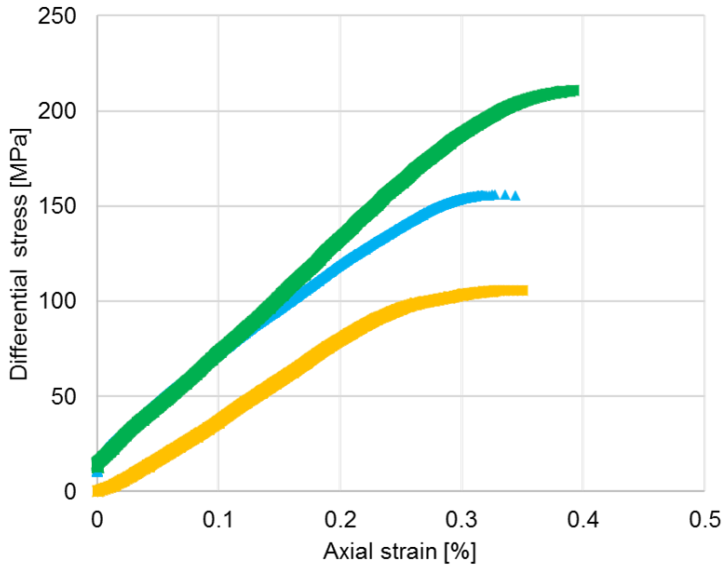

Figure 25: Results of Unconfined Compressive Strength experiments performed on borehole samples from Ordovician units of the study area. UCS magnitude is taken at the peak of the stress-strain curves just before brittle failure (represented by arrow showing loss of load bearing capacity). Yellow curve corresponds to rock intervals containing higher clay content while the blue and green curves correspond to more pure limestone. UCS magnitude is taken at the peak strength just before brittle failure represented by arrow showing loss of load bearing capacity.

The breakouts and DITF for the thirteen wells are overall similar in occurrence, orientation, and width, and show little depth dependence. Thus, the inferred stress directions and magnitudes also will be similar throughout the study area. Accordingly, the stress determination is shown for two representative wells, one containing both breakouts and DITF (well 15) and one containing only breakouts (well 26; Figure 26).

For well 15, where borehole breakouts and DITF where observed, the magnitudes of maximum and minimum horizontal stresses are well constrained within the range bounded by the stress polygon, UCS lines, and drilling induced tensile fracture criterion (Figure 26A). The magnitudes of S_{Hmax} range from 135 to 170 MPa and the magnitudes of S_{hmin} range from 94 to 118 MPa corresponding to the shaded polygon (Figure 26A). Although the magnitude intervals are moderately large, it is clear that the in situ stress falls within the normal or strike-slip regimes. There is a significant variation on the stress magnitudes with rock strength. When S_{Hmax} is lower than 143 MPa, S_v is the maximum principal stress, i.e., in the normal faulting regime (S_v.> S_{Hmax} > S_{hmin}; figure 29). On the other hand, when S_{Hmax} is larger than S_v strike-slip fault environment is favored (S_{Hmax}.> S_v > S_{hmin}; Figure 24).

For well 26, at a depth of 6149 meters (MD), only borehole breakouts where observed and the possible values of S_{Hmax} and S_{hmin} to create borehole breakouts lie within the shaded polygon shown in figure 26 B. The value of S_{Hmax} ranges from 139 to 198 MPa and the value of S_{hmin} ranges from 120 to 195 MPa. In this case, the values of S_{Hmax} and S_{hmin} suggest that the stress regimes are favored for normal faulting, strike-slip faulting or reverse faulting. For a values of S_{Hmax} lower than 148 MPa normal faulting is favored (S_v.> S_{Hmax} > S_{hmin}).

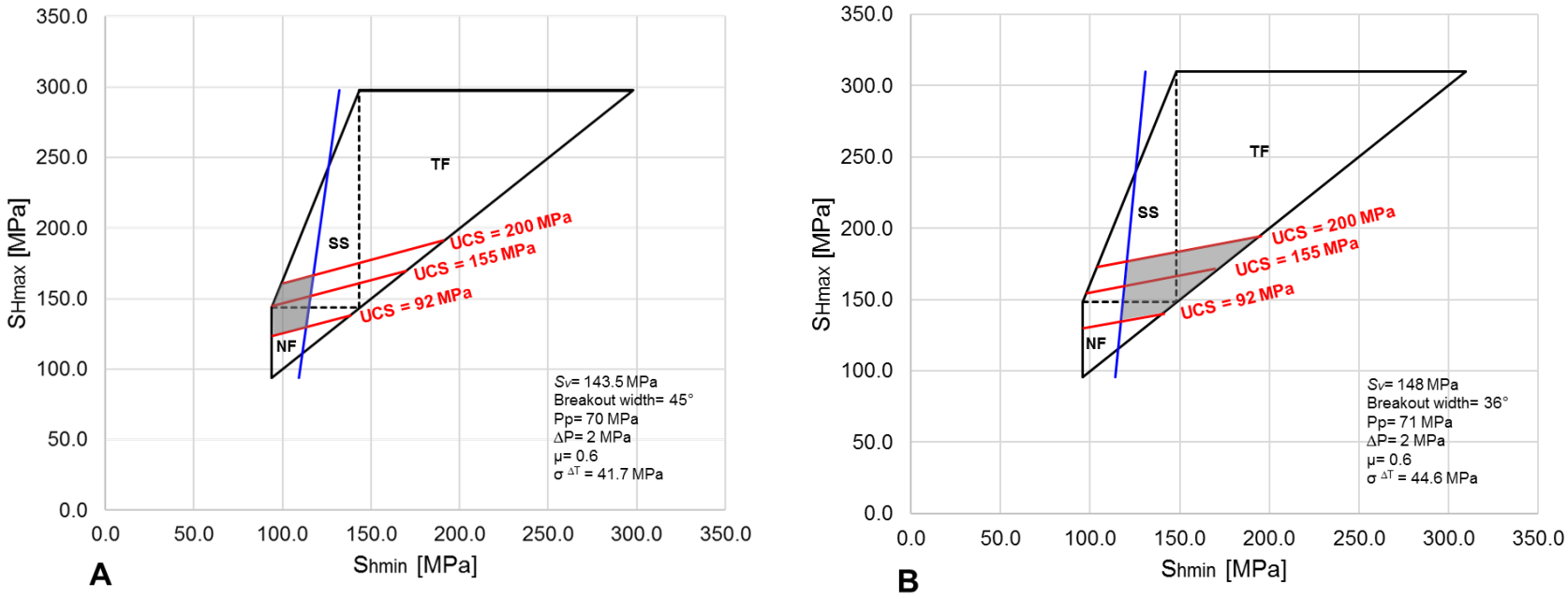

Figure 26: Constraints on the magnitude of horizontal stress at depth in the study area shown in plots of maximum versus minimum total horizontal stress for two representative wells. **A**- Stress state at a depth of 5969 m MD in well 15 where both borehole breakouts and DITF were observed. **B-** Stress state at a depth of 6149 m MD in well 26 where only borehole breakouts were observed. Stress polygons (outlined by solid and dashed black lines) delineate limits of the far-field stress magnitudes assuming Anderson's theory of faulting, a coefficient of sliding friction consistent with Byerlee's Law, and the overburden stress magnitude (see text). The red lines represent possible magnitudes of horizontal stress, S_{Hmax} and S_{hmin}, for representative values of UCS based on the width of observed borehole breakouts (see text). The blue line indicates the limiting stress for the formation of DITF (see text). The shaded polygon represents the range of permissible stress magnitudes on the basis of occurrence and analysis of induced borehole deformation features and theory. NF represents the field of normal faulting, SS represents the field of strike-slip faulting, and TF represents the field of thrust faulting as defined by Anderson's Theory (Figure 24).

For rocks strengths of between 92 and 200 MPa, it is clear that the magnitudes of S_{Hmax} can be higher than S_v; however, S_{hmin} can be lower or higher than S_v indicating predominantly strike-slip faulting regime (Figure 24). Given that DITF are observed in only some wells, overall the stress state in the Central Tazhong Uplift should be close to, or slightly above, the limiting condition for formation of DITF.

In wells 15 and 26, and in the other wells, there is a correlation between borehole breakout occurrence and lithology. Borehole breakouts are prevalent in mud-rich units (Lianglitage Formation) and less abundant to absent in "pure" limestone units (Yijianfang and Yingshan Formations) (Figures 19,20, and 21). This is expected since clay dominated rocks tend to exhibit lower rock strengths than pure limestones. Considering that most of the borehole failure occurred within mud dominated zones, it is likely that the stress determinations for the weaker rocks (UCS between 92 and 155 MPa) may be more representative of in situ stress within the deep portion of the wells overall, and thus in situ stress is best described as a normal or strike-slip fault state.

Current in situ tectonic stress and fault activation in the Tarim Basin

The stress magnitudes and orientations obtained from induced borehole deformation are used to determine if there has been a change in the stress state of the Central Tarim Basin relative to paleostress conditions during past tectonic events inferred from fault formation, reactivation kinematics, and Anderson's theory. Here the stress determination is used to assess if certain pre-existing structures may be reactivated under current in situ stress conditions. It is understood that fault slip will occur when the ratio of shear to normal stress is high enough, i.e., equal to that of the static frictional strength, μ. For carbonate lithologies μ may be relatively high ($\mu \geq 0.7$) based

on direct measurements of the coefficients of sliding friction (Byerlee, 1978). The Mohr-Coulomb failure analysis (e.g., Handin, 1969) assuming a conservative μ = 0.6 is used to evaluate the propensity of a pre-existing fault to slip in the Tazhong Uplift for the inferred in situ stresses.

The strike-slip faults are the dominant set of faults in the Tazhong Uplift, and most suitably oriented to fail under the stress directions observed from borehole analyses; therefore, the reactivation potential of the strike-slip faults is analyzed. The in situ stress obtained from well 15, as well as the shear and normal stress conditions on strike-slip faults (using the average orientation of the faults; Figure 27) are represented with Mohr circles, and the friction failure criterion for a coefficient of sliding friction of 0.6 is also represented (Figure 28).

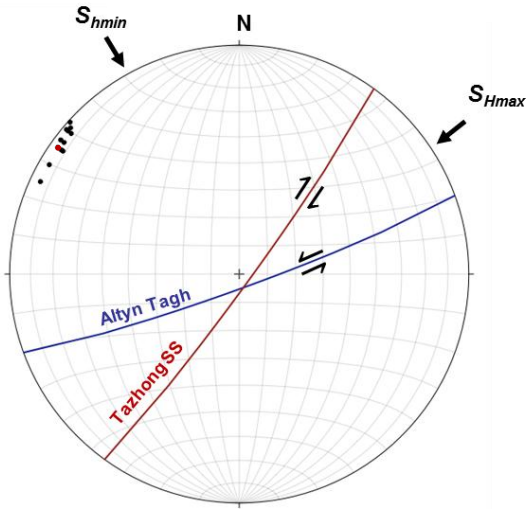

Figure 27: Relationship of in situ stress orientation in the study area to the average orientation of the left-lateral strike-slip faults of the Central Uplift and to the Altyn Tagh fault bounding the southern Tarim Basin. Equal area projection onto the horizontal plane with North at the top of the diagram. Great circles represent the average orientation of the Altyn Tagh fault (blue) and the Tazhong strike-slip fault system (red). Note that the faults are similarly oriented for reactivation under the current in situ stress. Black arrows indicate the current fault slip direction of the Altyn Tagh fault and the expected slip direction for reactivation of the Tazhong strike-slip faults based on the in situ orientation of S_{Hmax} and S_{hmin}. Black dots represent the poles to the twelve main strike-slip faults (with the red dot indicating the best fit pole) observed in the Tazhong Uplift.

Frictional reactivation of the faults under current stress is favored if the shear and normal stress on the faults is equal to (or exceeds) the failure criterion. Based on the relative magnitudes of S_{Hmax} and $S_{hmin,}$ the most likely types of fault reactivation is by normal oblique, right-lateral strike-slip (Figure 26). Accordingly, end member reactivation of pure normal and pure strike-slip are considered to determine reactivation of the pre-existing strike-slip faults (Figure 28).

To reactivate faults with normal slip, the lowest value of the effective minimum principal stresses S_{hmin}' must be around 24 MPa (94 MPa-P_p) and the maximum possible value of S_{hmin}' must be 40 MPa (110 MPa- P_p) (Figure 28 A and B). For a coefficient of friction of 0.6, a pre-existing fault dipping at 85˚ (oriented 05° from $\sigma_1 = S_v$) will not reactivate under the in situ stresses conditions. When S_{hmin}' is high (110 MPa-P_p), the Mohr circle does not intersect the failure envelope (Figure 28 B and D). When S_{hmin}' decreases, the differential stress increases and the Mohr circle intersects the failure line but the fault is not optimally oriented for frictional sliding and does not satisfy the frictional slip criterion (Figure 28 C).

To reactivate the faults with left-lateral strike-slip with $S_{Hmax} > Sv > S_{hmin}$, S_{Hmax} must be equal or higher than 143 MPa but lower than 170 MPa. Similarly, S_{hmin} must be within 94 and 118 MPa. When both S_{Hmax}' and S_{hmin}' are the lowest possible values to promote strike-slip faults, the Mohr circle intersects the failure envelope but again the faults are not optimally oriented for frictional sliding and come close, but do not satisfy the friction criterion (Figure 28 C). As both the minimum and maximum principal stresses increase to the highest possible values within strike-slip faulting regime, the Mohr circle no longer intersects the friction envelope and therefore the faults are far from the condition for reactivation. As indicated by the friction envelopes (using a coefficient of sliding friction of 0.6) the faults in general are not critically stressed or optimally oriented for reactivation under the in situ stress conditions (Figure 28).

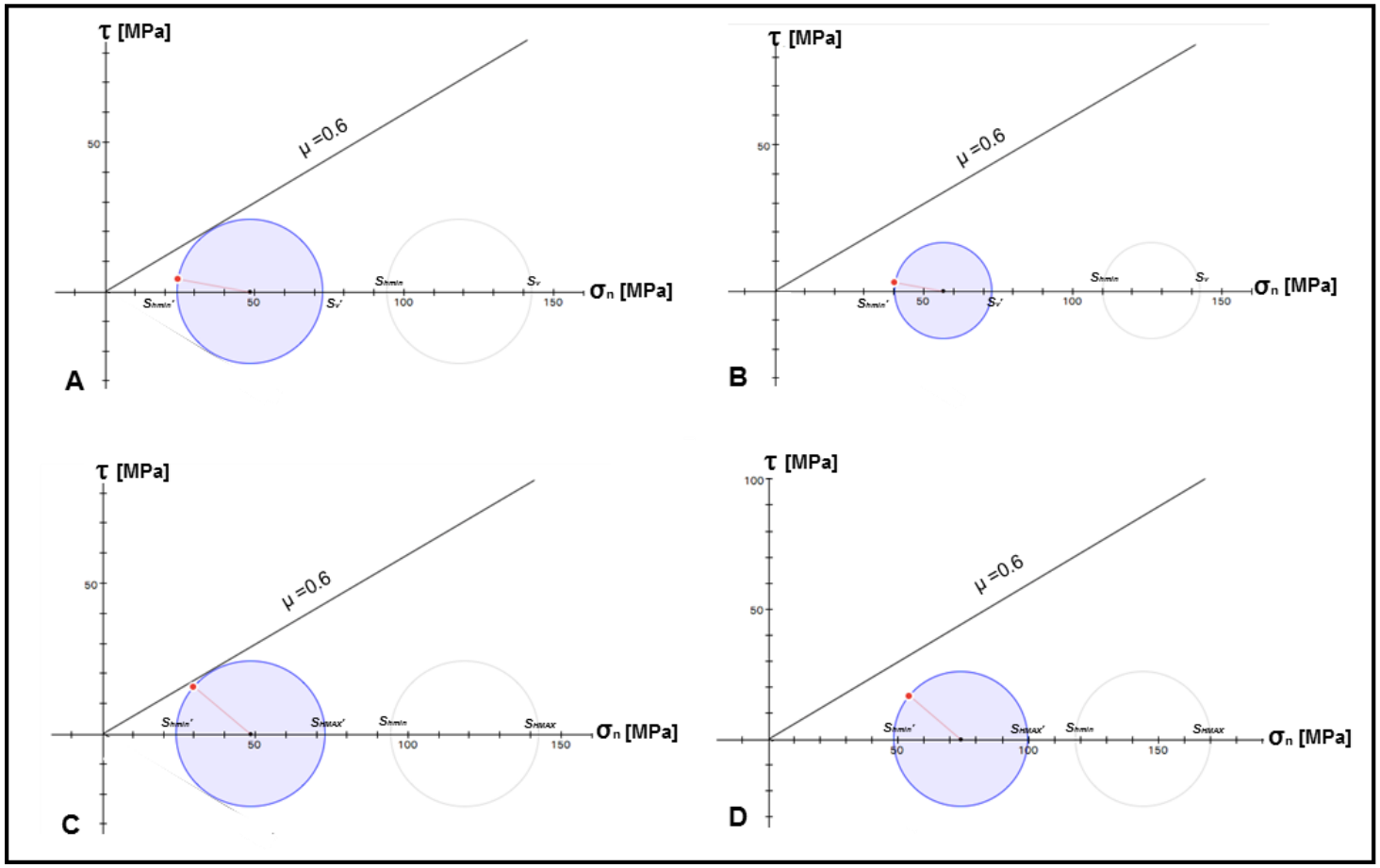

Figure 28: Mohr diagrams showing the possibility of reactivation of the strike-slip faults of the Central Tazhong Uplift for the current in situ stress assuming stress conditions determined from well 15. **A**- Lowest limit of S_{hmin} and S_v for normal faulting. **B**- Highest limit of S_{hmin} and S_v for normal faulting. **C**-Lowest limit of S_{hmin} and S_{Hmax} for strike-slip faulting. **D**-Highest limit of S_{hmin} and S_{Hmax} for strike-slip faulting. In these figures, the possibility of reactivation is greatest if the shear and normal stress on the faults (represented by the red dot) intersects or is above the sliding friction criterion (represented by the black line); accordingly, reactivation is most possible for case C, but overall is unlikely. Frictional envelopes assume a coefficient of sliding friction of 0.6. The light gray circles represent the total stress, and the blue circles represent the effective stress conditions.

The in situ stress determination herein is consistent with other recent analysis of stress magnitude and orientations in the Central Tarim basin well east of the study area (Figure 23; Sun et al., 2017). In Sun et al. (2017) the focus is the use of Anelastic Strain Recovery (ASR) techniques to determine in situ stress at depths similar to those here (Figure 23). The ASR technique has the potential to recover the total stress, and in particular the orientations of the principal stress tensor. Sun et al. (2017) reports that the principal stress directions are nearly parallel and perpendicular to the vertical, supporting the assumption of Andersonian stress states for the Tarim basin, and their determination of stress directions are similar; however, they conclude normal stress faulting environments whereas within the study area it appears that S_{Hmax} and S_v are similar.

Seismicity along the peripheries of the Tarim Basin show in situ stress satisfies frictional failure criteria, the stress in the interior of the basin does not. The clear difference in the current activation of faults may be explained by assuming the differential, in situ stress magnitudes are greater, or the faults are weaker, at the margins of the basin than in the interior of the basin. It is likely that fault strength is different because 1) the interior basin faults apparently have not been reactivated since before the onset of the Indo-Asia orogeny and thus may have frictional strengths greater than predicted by Byerlee's law due to significant healing, 2) the reactivation of the interior faults would involve an opposite sense of shear than past movements, which may be impeded by geometric attributes of the fault surfaces, and 3) that very large faults at the margins of the basin may operate at much lower levels of friction than smaller crustal faults. For example, the Altyn Tagh fault along the boundary of the basin south of the study area is a lithospheric fault approximately 1600 km in length with 400 km left-lateral displacement during the Cenozoic (Shuang DAI et al., 2017). It is widely recognized that such large strike-slip faults (e.g., the San

Andreas continental transform fault) may operate at much apparent frictional strengths much less than predicted from Byerlee's Law (Zoback et al., 1987; Noda et al., 2009). Accordingly, assumption (3) above is investigated using the new information on current stress state in the Tarim Basin.

Using techniques presented above to assess the potential for reactivation of the interior strike-slip faults of the Tarim Basin, stress orientation and magnitude in the study area are extrapolated to the margin where the Altyn Tagh fault is located and displaying seismic activity to determine the apparent friction of the fault (Figure 29). The angle between S_{Hmax} and the Altyn Tagh fault is similar to that of the interior strike-slip faults (though opposite sense of shear) so geometrically they are similarly susceptible for activation (Figure 27). As shown by Mohr-Coulomb analysis, assuming the magnitude of stresses in the basin, and pore pressures of hydrostatic or that observed in the wells at 6000 m MD in the basin, the friction envelope for the Altyn Tagh fault is determined (Figure 29). For several cases the determined frictional strength (coefficient of sliding friction) for the Altyn Tagh fault is noteably low, $\mu < 0.39$ (Figure 29). The results suggest that the Altyn Tagh is potentially shearing at very low frictional strengths is comparable to that determined for the San Andreas Fault in California (e.g., Zoback et al., 1987; Coble et al., 2014).

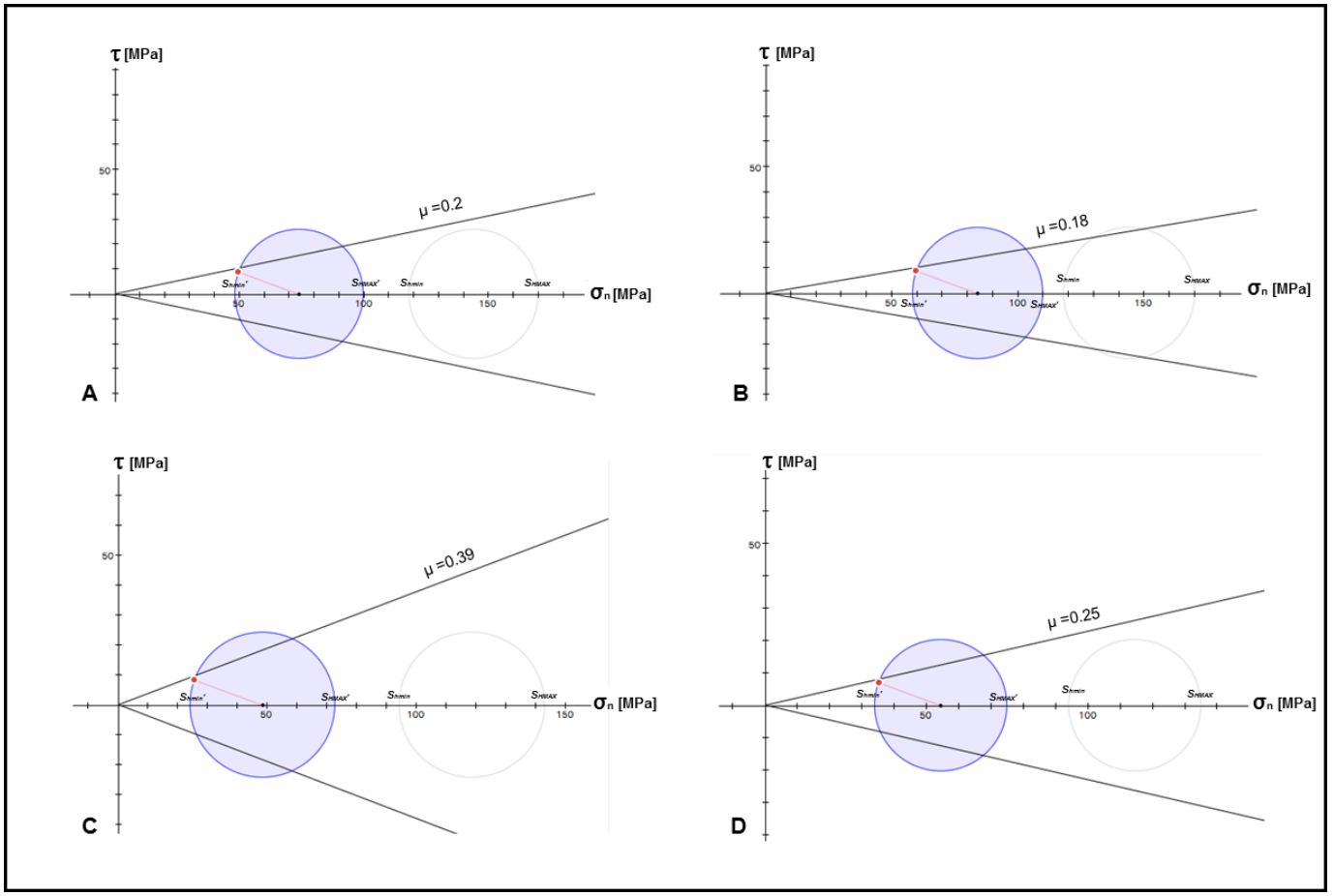

Figure 29: Mohr diagrams showing the estimated coefficient of friction for the Altyn Tagh fault for the current in situ stress assuming stress conditions determined from well 15. **A-** Highest limit of S_{hmin} and S_{Hmax} for strike-slip faulting and a P_p of 70 MPa. **B-** Highest limit of S_{hmin} S_{Hmaz} for strike-slip faulting and hydrostatic P_p. **C**-Lowest limit of S_{hmin} and S_{Hmax} for strike-slip faulting and P_p of 70 MPa. **D-** Lowest limit of S_{hmin} and S_{Hmax} for strike-slip faulting and hydrostatic P_p. The Altyn Tagh is an active fault and therefore the fault plane must intersect the sliding friction criterion (represented by the black line). The light gray circles represent the total stress, and the blue circles represent the effective stress conditions.

CONCLUSIONS

- The Tazhong Uplift is characterized by Paleozoic and Mesozoic fault systems that controlled the depositional and structural evolution of the region. Three characteristic fault systems have been identified: Middle-Late Ordovician reverse faults, Silurian-Permian left-lateral strike-slip faults, and Permian-Triassic normal faults. The development of the fault systems resulted from major tectonic events including Pre-Cambrian to Early Ordovician rifting, Middle Ordovician to Permian convergence and volcanism. Late Mesozoic and Cenozoic age strata is generally undeformed.
- Pre-existing structures have exerted control on the structural development of the Central Tarim Basin since the Late Proterozoic. Evidence for fault reactivation of normal faults and strike-slip fault systems is observed. The spatial distribution of younger deformation events is strongly correlated with the location of older structures. For example, the distribution of igneous bodies and collapse structures preferentially develop near strike-slip fault systems. Pre-existing faults (planes of weakness), as well as, paleostress orientations and magnitudes encouraged selective reactivation and promoted successive deformation events to occur in the northern slope of the Tazhong Uplift.
- Fault zones are only observed in Paleozoic and Triassic sediments; no apparent deformation is present in Late Mesozoic and Cenozoic sediments. Although the Himalayan Orogeny promoted large-scale deformation in the perimeters of the basin, minor deformation is observed in the Central Tarim Basin. The in situ stress orientation determined from borehole breakouts and DITF is consistent for almost all wells, where S_{Hmax} and S_{hmin} are 331° and 061°,

respectively. The current in situ maximum horizontal stress is directed more easterly than during tectonic events throughout the Paleozoic.

- The Himalayan Orogeny promoted large-scale deformation in the perimeters of the Tarim Basin, but no apparent deformation is present in Late Mesozoic and Cenozoic sediments in the Tazhong Uplift. Even though horizontal compressional stress regimes might be expected in the interior if the basin, the present-day magnitudes of S_{Hmax} and S_{hmin} indicate a normal or strike-slip faulting regime (either S_v or S_{Hmax} corresponds to the maximum principal stress). Furthermore, the relative magnitudes of the current maximum and minimum horizontal stresses are not sufficient to cause fault reactivation of the pre-existing faults of the Central Uplift.
- The current activation of faults along the margins of the Tarim Basin evidenced by ongoing seismicity contasts with lack of current deformation within the Basin, which may be explained by the hypothesis that very large faults at the margins of the basin operate at much lower levels of friction than smaller crustal faults in the basin interior. Evaluation of the frictional strength of the major bounding fault, the Altyn Tagh, indicates it operates at an apparent low coefficient of friction ($\mu < 2$) and accommodates a large fraction component of the convergence produced by the Indo-Asian Collision, as well as buffering the stress magnitudes within the Basin.

REFRENCES

Allen, M.B., Vincent, S.J., Wheeler, P.J., 1999. Late Cenozoic tectonics of the Kepingtage thrust zone: interactions of the Tien Shan and Tarim Basin, northwest China. Tectonics 18, 639-654.

Anderson, E. M., 1942. The dynamics of faulting and dyke formation with applications to Britain. Oliver and Boyd.

Busby, C., Pérez, A.A., 2011. Tectonics of sedimentary basins: Recent advances. John Wiley & Sons.

Butler, R., 1989. The influence of pre-existing basin structure on thrust system evolution in the Western Alps. Geological Society, London, Special Publications 44, 105-122.

Byerlee, J., 1978. Friction of rocks, Rock friction and earthquake prediction. Springer, pp. 615-626.

Carroll, A., Graham, S., Smith, M., 2010. Walled sedimentary basins of China. Basin Research 22, 17-32.

Chang, C., McNeill, L.C., Moore, J.C., Lin, W., Conin, M., Yamada, Y., 2010. In situ stress state in the Nankai accretionary wedge estimated from borehole wall failures. Geochemistry, Geophysics, Geosystems 11.

Charvet, J., Shu, L., Laurent-Charvet, S., Wang, B., Faure, M., Cluzel, D., Chen, Y., De Jong, K., 2011. Palaeozoic tectonic evolution of the Tianshan belt, NW China. Science China Earth Sciences 54, 166-184.

Christie-Blick, N., Biddle, K.T., 1985. Deformation and basin formation along strike-slip faults.

Coble, C., French, M., Chester, F., Chester, J., Kitajima, H., 2014. In situ frictional properties of San Andreas Fault gouge at SAFOD. Geophysical Journal International 199, 956-967.

Dai, S., Dai, W., Zhao, Z., Luo, J., Qiang, L., Ma, X., ... & Xu, J., 2017. Timing, displacement and growth pattern of the Altyn Tagh fault: A review. Acta Geologica Sinica (English Edition), 91(2), 669-687.

DeCelles, P. G., Gehrels, G. E., Quade, J., & Ojha, T. P., 1998. Eocene-early Miocene foreland basin development and the history of Himalayan thrusting, western and central Nepal. Tectonics, 17(5), 741-765.

Eichelberger, N.W., Hughes, A.N., Nunns, A.G., 2015. Combining multiple quantitative structural analysis techniques to create robust structural interpretations. Interpretation 3, SAA89-SAA104.

Eichelberger, N.W., Nunns, A.G., Groshong, R.H., Hughes, A.N., 2017. Direct estimation of fault trajectory from structural relief. AAPG Bulletin 101, 635-653.

Gehrels, G. E., DeCelles, P. G., Martin, A., Ojha, T. P., Pinhassi, G., & Upreti, B. N., 2003. Initiation of the Himalayan orogen as an early Paleozoic thin-skinned thrust belt. GSA today, 13(9), 4-9.

Ghisetti, F., Vezzani, L., 2005. Inherited structural controls on normal fault architecture in the Gulf of Corinth (Greece). Tectonics 24.

Han, X., Deng, S., Tang, L., Cao, Z., 2017. Geometry, kinematics and displacement characteristics of strike-slip faults in the northern slope of Tazhong uplift in Tarim Basin: A study based on 3D seismic data. Marine and Petroleum Geology.

Hansen, D.M., Cartwright, J., 2006. The three-dimensional geometry and growth of forced folds above saucer-shaped igneous sills. Journal of Structural Geology 28, 1520-1535.

Heidbach, O., Tingay, M., Barth, A., Reinecker, J., Kurfeß, D., & Müller, B., 2001. World stress map. Naturwissenschaften, 88, 357-371.

Infante-Paez, L., 2018. Seismic expression of igneous bodies in sedimentary basins and their impact on hydrocarbon exploration: Examples from a compressive tectonic setting, Taranaki Basin, New Zealand: PhD. Dissertation, University of Oklahoma.

Infante-Paez, L., Marfurt, K.J., 2017. Seismic expression and geomorphology of igneous bodies: A Taranaki Basin, New Zealand, case study. Interpretation 5, SK121-SK140.

Jaeger, J.C., Cook, N.G., Zimmerman, R., 2009. Fundamentals of rock mechanics. John Wiley & Sons.

Jia, D., Lu, H., Cai, D., Wu, S., Shi, Y., Chen, C., 1998. Structural features of northern Tarim Basin: Implications for regional tectonics and petroleum traps. AAPG bulletin 82, 147-159.

Lan, X., Lü, X., Zhu, Y., Yu, H., 2015. The geometry and origin of strike-slip faults cutting the Tazhong low rise megaanticline (central uplift, Tarim Basin, China) and their control on hydrocarbon distribution in carbonate reservoirs. Journal of Natural Gas Science and Engineering 22, 633-645.

Lan, X.d., Lü, X.x., Yu, H.f., Zhu, Y.m., Yan, B., 2014. Early Palaeozoic carbonate reservoirs from the Yingshan Formation of Well block ZG-43 in Tazhong Low Rise, Central Uplift,

Tarim Basin, NW China: geological features and controlling factors. Geological Journal 49, 256-270.

Lee, K., 1985. Geology of the Tarim Basin with special emphasis on petroleum deposits, Xinjiang Uygur Zizhiqu, Northwest China. US Geological Survey.

Li, C., Wang, X., Li, B., He, D., 2013. Paleozoic fault systems of the Tazhong uplift, Tarim basin, China. Marine and petroleum geology 39, 48-58.

Li, S., Ren, J., Xing, F., Liu, Z., Li, H., Chen, Q., Li, Z., 2012. Dynamic processes of the Paleozoic Tarim Basin and its significance for hydrocarbon accumulation—a review and discussion. Journal of Earth Science 23, 381-394.

Lin, B., Zhang, X., Xu, X., Yuan, J., Neng, Y., Zhu, J., 2015. Features and effects of basement faults on deposition in the Tarim Basin. Earth-Science Reviews 145, 43-55.

Lunn, R.J., Willson, J.P., Shipton, Z.K., Moir, H., 2008. Simulating brittle fault growth from linkage of preexisting structures. Journal of Geophysical Research: Solid Earth 113.

Martel, S.J., Boger, W.A., 1998. Geometry and mechanics of secondary fracturing around small three-dimensional faults in granitic rock. Journal of Geophysical Research: Solid Earth 103, 21299-21314.

Mattern, F., Schneider, W., 2000. Suturing of the Proto-and Paleo-Tethys oceans in the western Kunlun (Xinjiang, China). Journal of Asian Earth Sciences 18, 637-650.

Molnar, P., & Tapponnier, P., 1975. Cenozoic tectonics of Asia: effects of a continental collision. Science, 189(4201), 419-426.

Morley, C. K., 2002. A tectonic model for the Tertiary evolution of strike–slip faults and rift basins in SE Asia. Tectonophysics, 347(4), 189-215.

Noda, H., Dunham, E. M., & Rice, J. R., 2009. Earthquake ruptures with thermal weakening and the operation of major faults at low overall stress levels. Journal of Geophysical Research: Solid Earth, 114(B7).

Pizzi, A., Galadini, F., 2009. Pre-existing cross-structures and active fault segmentation in the northern-central Apennines (Italy). Tectonophysics 476, 304-319.

Rutter, E., Holdsworth, R., Knipe, R., 2001. The nature and tectonic significance of fault-zone weakening: an introduction. Geological Society, London, Special Publications 186, 1-11.

Schlager, W., Purkis, S., 2015. Reticulate reef patterns–antecedent karst versus self-organization. Sedimentology 62, 501-515.

Sibson, R.H., 1985. A note on fault reactivation. Journal of Structural Geology 7, 751-754.

Sibson, R.H., 1990. Rupture nucleation on unfavorably oriented faults. Bulletin of the Seismological Society of America 80, 1580-1604.

Su, B.-X., Qin, K.-Z., Sakyi, P.A., Li, X.-H., Yang, Y.-H., Sun, H., Tang, D.-M., Liu, P.-P., Xiao, Q.-H., Malaviarachchi, S.P., 2011. U–Pb ages and Hf–O isotopes of zircons from Late Paleozoic mafic–ultramafic units in the southern Central Asian Orogenic Belt: tectonic implications and evidence for an Early-Permian mantle plume. Gondwana Research 20, 516-531.

Sun, D., Sone, H., Lin, W., Cui, J., He, B., Lv, H., Cao, Z., 2017. Stress state measured at~ 7 km depth in the Tarim Basin, NW China. Scientific Reports 7.

Sylvester, A.G., 1988. Strike-slip faults. Geological Society of America Bulletin 100, 1666-1703.

Thomson, K., 2007. Determining magma flow in sills, dykes and laccoliths and their implications for sill emplacement mechanisms. Bulletin of Volcanology 70, 183-201.

Tingay, M., Reinecker, J., Müller, B., 2008. Borehole breakout and drilling-induced fracture analysis from image logs. World Stress Map Project, 1-8.

Wu, G., Yang, H., He, S., Cao, S., Liu, X., Jing, B., 2016. Effects of structural segmentation and faulting on carbonate reservoir properties: A case study from the Central Uplift of the Tarim Basin, China. Marine and Petroleum Geology 71, 183-197.

Yang, J., Zhu, W., Guan, D., Zhu, B., Yuan, L., Xiang, X., Su, J., He, J., Wu, X., 2016. 3D seismic interpretation of subsurface eruptive centers in a Permian large igneous province, Tazhong Uplift, central Tarim Basin, NW China. International Journal of Earth Sciences 105, 2311-2326.

Yang, S.-F., Li, Z., Chen, H., Santosh, M., Dong, C.-W., Yu, X., 2007. Permian bimodal dyke of Tarim Basin, NW China: geochemical characteristics and tectonic implications. Gondwana Research 12, 113-120.

Yang, Y., Liu, M., 2002. Cenozoic deformation of the Tarim plate and the implications for mountain building in the Tibetan Plateau and the Tian Shan. Tectonics 21.

Yu, J., Li, Z., Yang, L., 2016. Fault system impact on paleokarst distribution in the Ordovician Yingshan Formation in the central Tarim basin, northwest China. Marine and Petroleum Geology 71, 105-118.

Yuzhu, K., Zhihong, K., 1996. Tectonic evolution and oil and gas of Tarim Basin. Journal of Southeast Asian Earth Sciences 13, 317-325.

Zalan, P.V., 1987. Identification of strike-slip faults in seismic sections, 1987 SEG Annual Meeting. Society of Exploration Geophysicists.

Zhang, Y., Lü, X., Yang, H., Han, J., Lan, X., Zhao, Y., & Zhang, J. (2014). Control of hydrocarbon accumulation by Lower Paleozoic cap rocks in the Tazhong Low Rise, Central Uplift, Tarim Basin, West China. Petroleum Science, 11(1), 67-80.

Zoback, M.D., 2010. Reservoir geomechanics. Cambridge University Press.

Zoback, M., Barton, C., Brudy, M., Castillo, D., Finkbeiner, T., Grollimund, B., Moos, D., Peska, P., Ward, C., Wiprut, D., 2003. Determination of stress orientation and magnitude in deep wells. International Journal of Rock Mechanics and Mining Sciences 40, 1049-1076.

Zoback, M.D., Moos, D., Mastin, L., Anderson, R.N., 1985. Well bore breakouts and in situ stress. Journal of Geophysical Research: Solid Earth 90, 5523-5530.

Zoback, M. D., Zoback, M. L., Mount, V. S., Suppe, J., Eaton, J. P., Healy, J. H., ... & Wong, I. G., 1987. New evidence on the state of stress of the San Andreas fault system. Science, 238(4830), 1105-1111.

APPENDIX

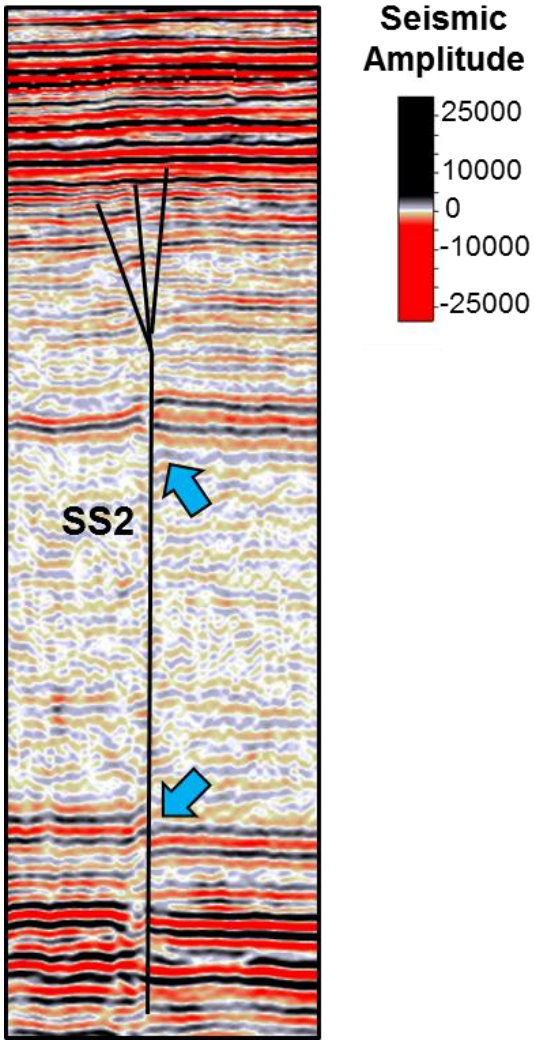

Figure 30: Uninterpreted seismic profile displaying strike-slip fault SS2 in black. Note vertical displacements along the deep, planar portion of the strike-slip fault as indicated by the blue arrows.

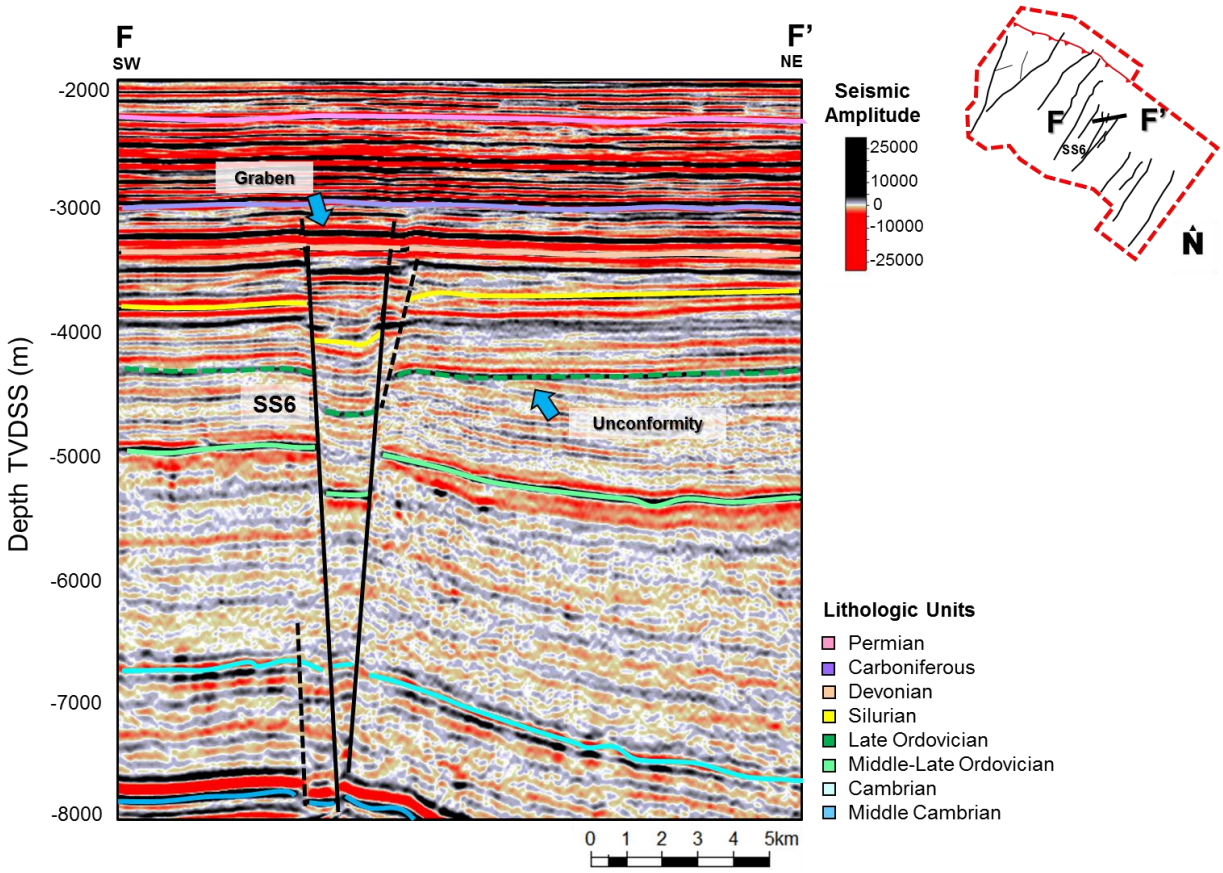

Figure 31: Interpreted seismic profile F-F'. Carboniferous normal faults (black) associated with strike-slip faults are illustrated in black. Dotted lines indicate interpretation uncertainties. Middle Cambrian to Permian formation tops are color coded.

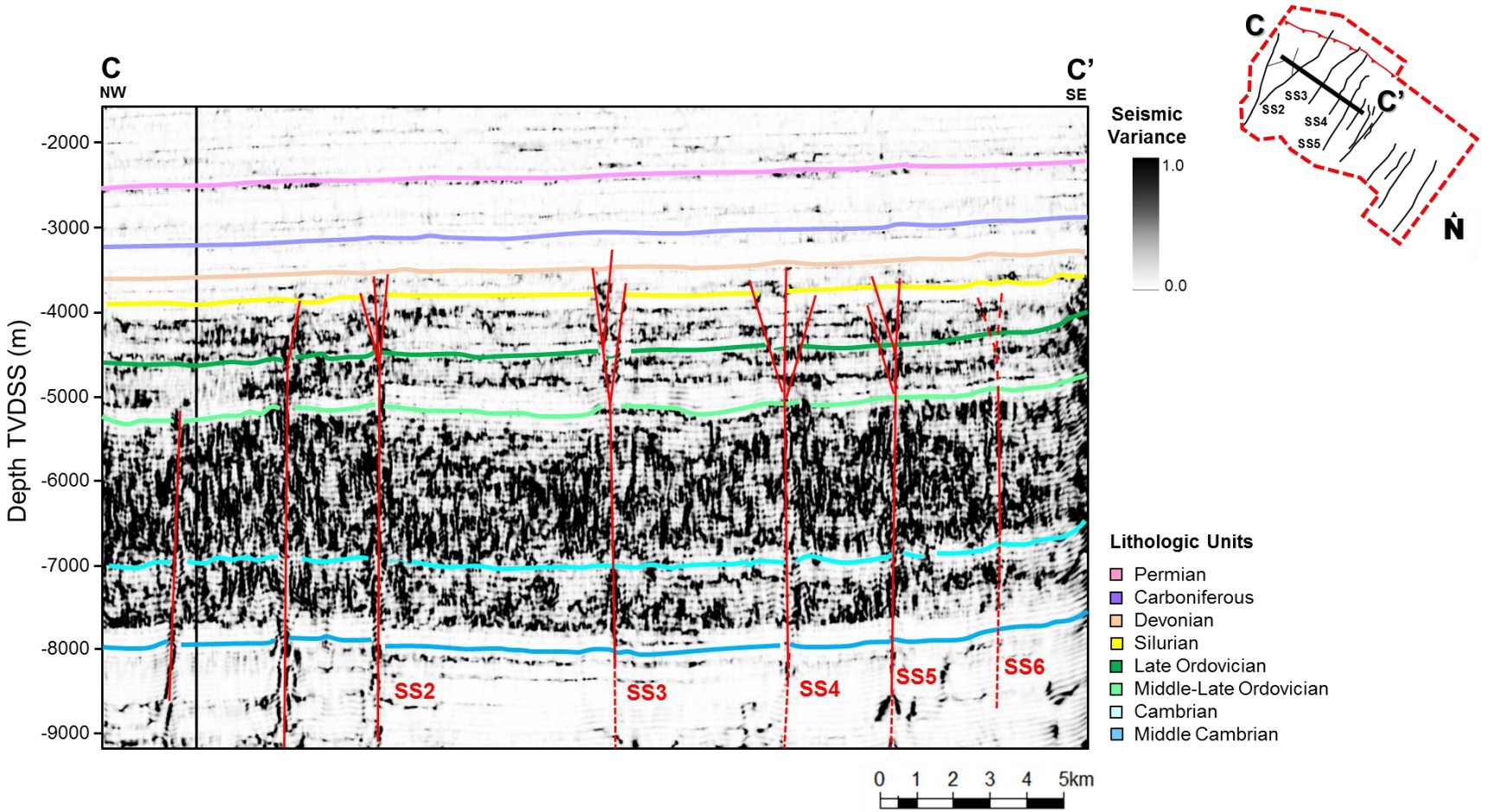

Figure 32: Interpreted seismic variance profile (C-C') through the TZ45 seismic volume. Silurian-Permian strike-slip faults are shown in red. The strike-slip faults exhibit subvertical planar structures in the Cambrian and Middle-Late Ordovician units and flower structures in Silurian to Carboniferous strata. Middle Cambrian to Permian formation tops are color coded.

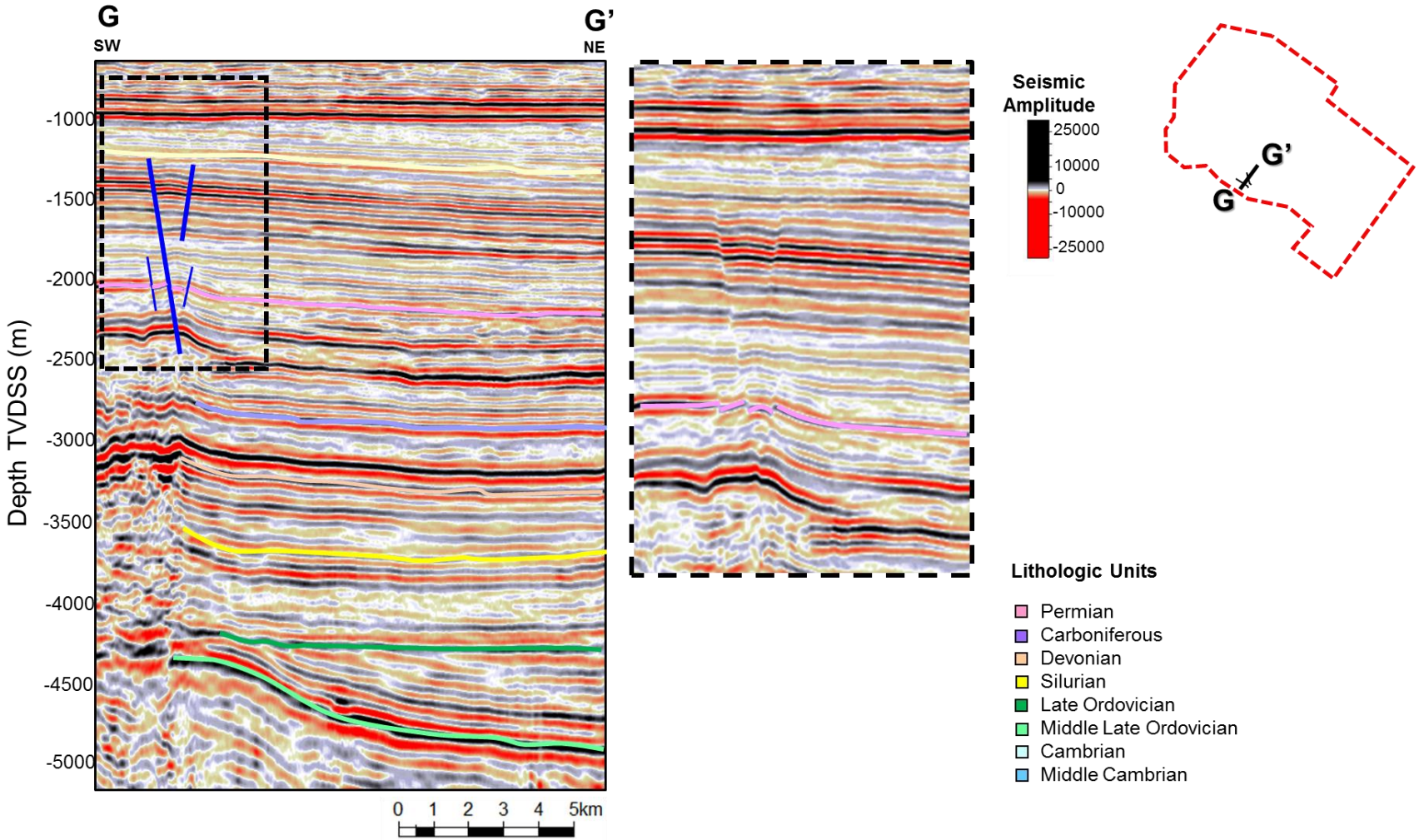

Figure 33: Interpreted seismic profile (G-G') illustrating a Permian volcanic body and associated Triassic normal faults. Dashed lines represent. Middle Cambrian to Permian formation tops are color coded.

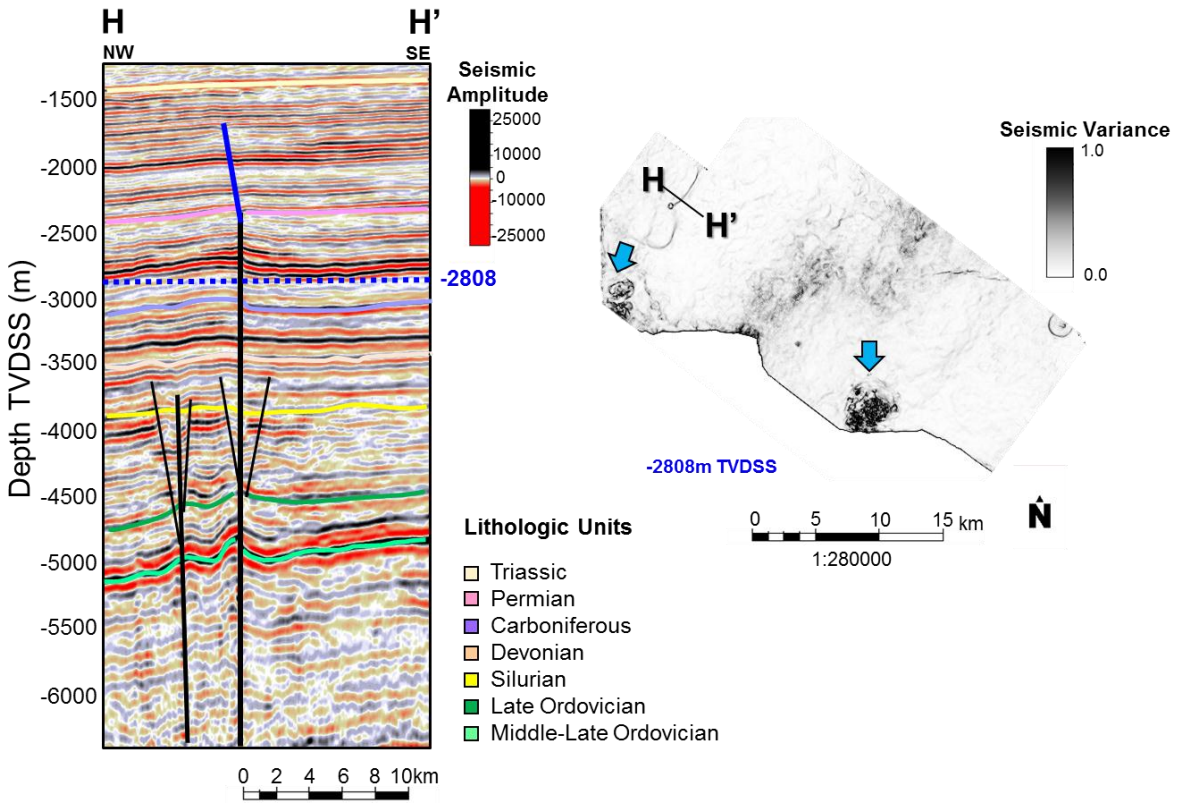

Figure 34: Interpreted seismic profile (H-H') illustrating fault SS1 cutting Permian formations. Black lines in the left panel represent strike-slip faults and black dashed line represent a Triassic normal fault. Middle Cambrian to Permian formation tops are color coded. The right panel is a seismic variance depth slice at -2808 m TVDSS showing two of the Permian extrusions (indicated by the blue arrows) as well as a Triassic fault that is preferentially oriented in the same direction as fault SS1.

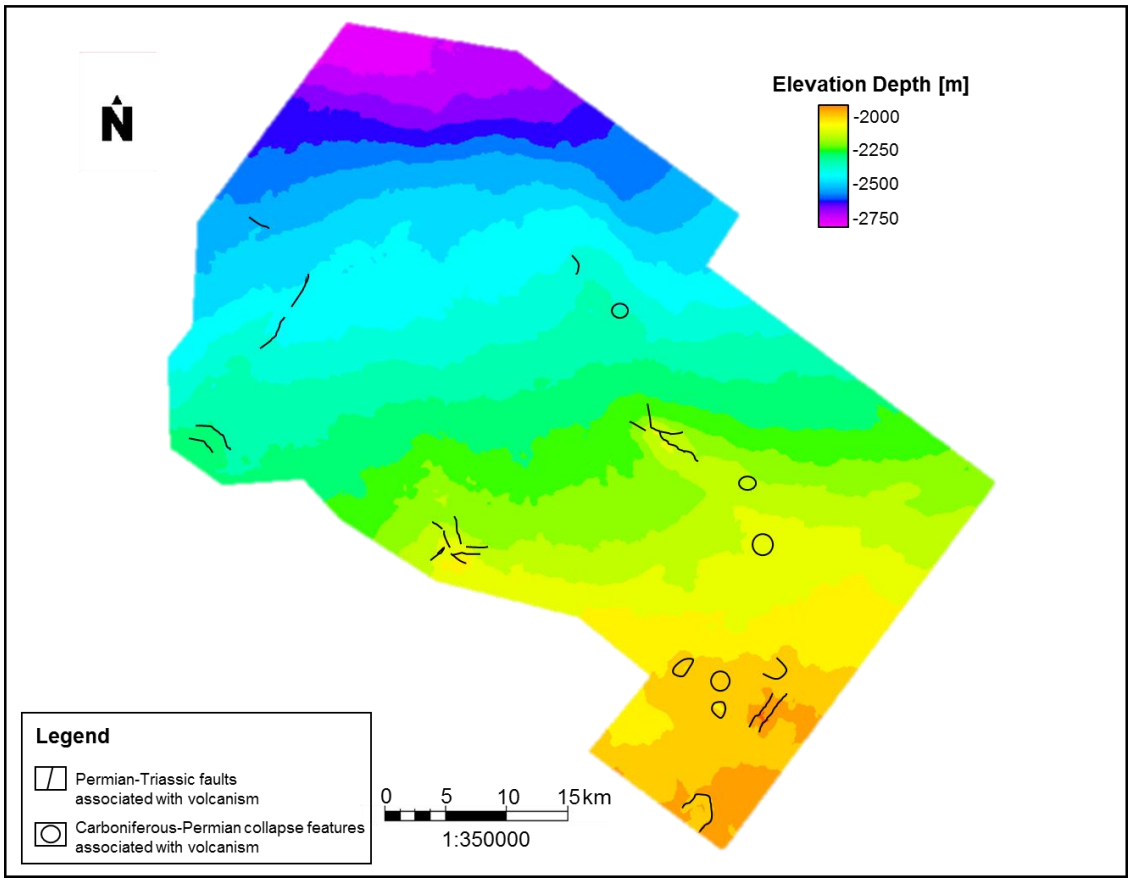

Figure 35: Structure map of the top of the Permian horizon. The structure map displays Triassic faults and collapse structures associated with volcanism.

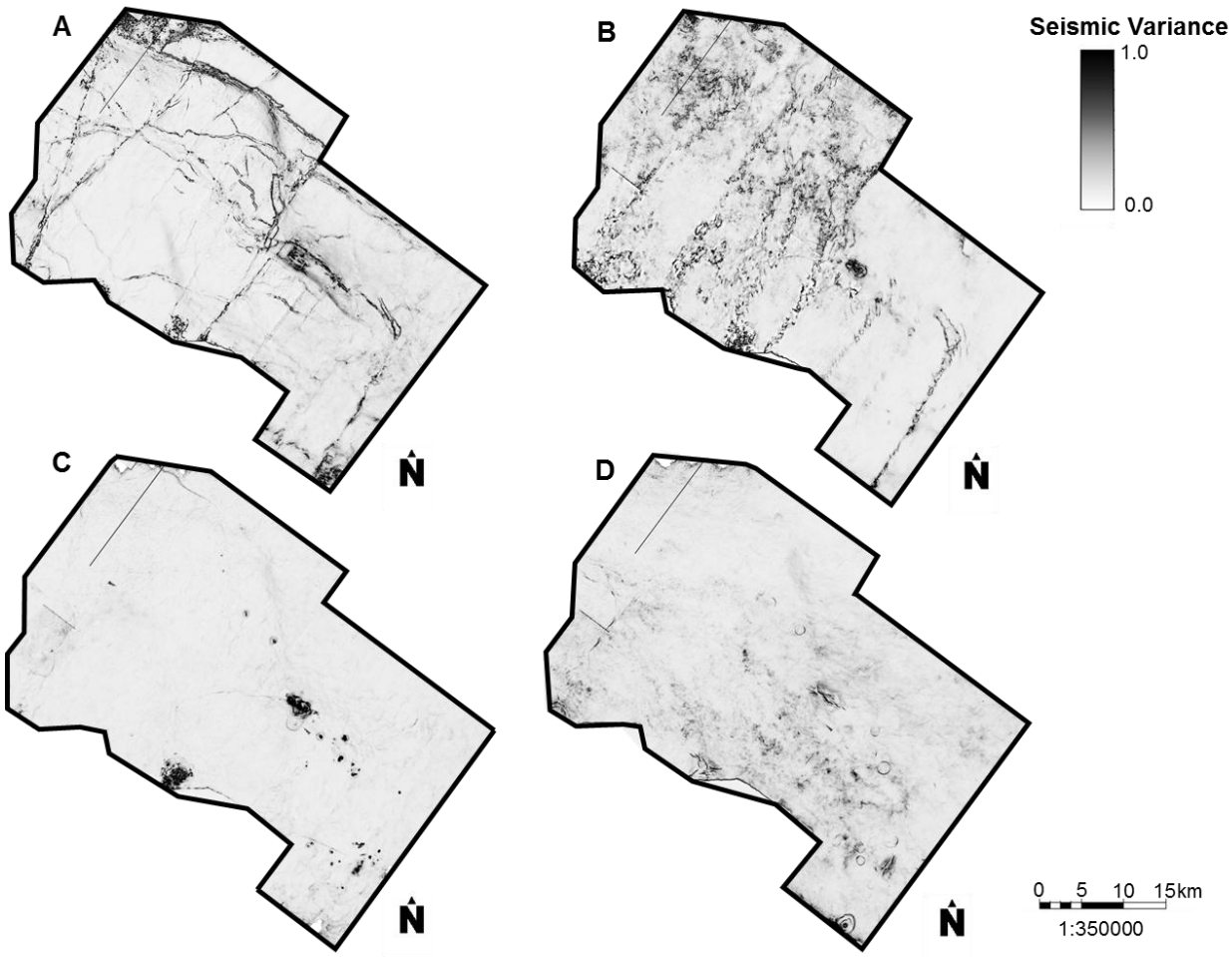

Figure 36: Variance slices extracted along four stratigraphic horizons. **A**- Variance slice extracted along the top of the Middle-Late Ordovician illustrating the planar geometry of strike-slip faults. **B**- Variance slice 80 m below the top of the Silurian illustrating array of secondary faults. **C**- Variance slice extracted the Carboniferous displaying extrusions and collapse structures. **D**- Variance slice extracted along the top of the Permian displaying faults associated with collapse features and Permian volcanism.

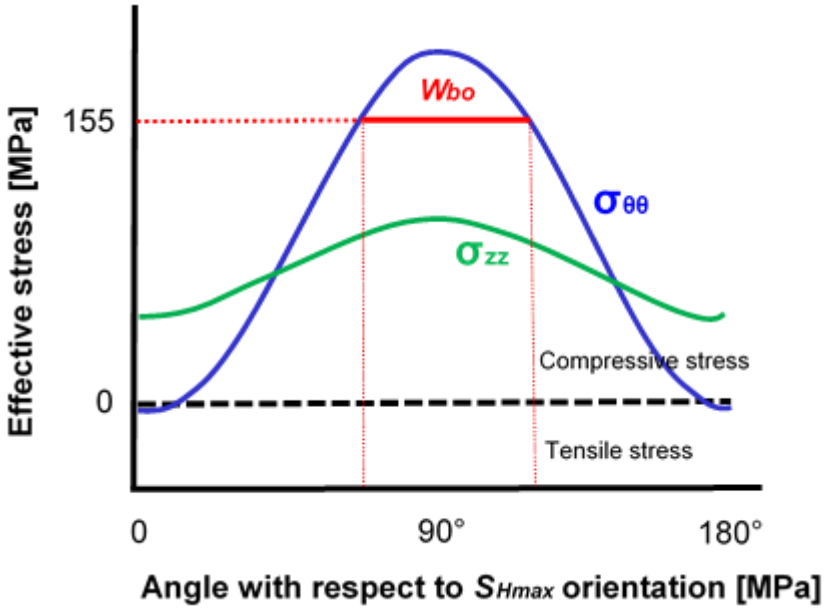

Figure 37: Plot of the variation in magnitude of the local circumferential and axial effective-stress components at the wellbore wall. The angle is measured from the direction of S_{Hmax}. The circumferential stress $\sigma_{\theta\theta}$ and vertical stress σ_{zz} are plotted in blue and green respectively. A hypothetical borehole breakout width (W_{bo}) for a rock strength of 155 MPa is shown in red.

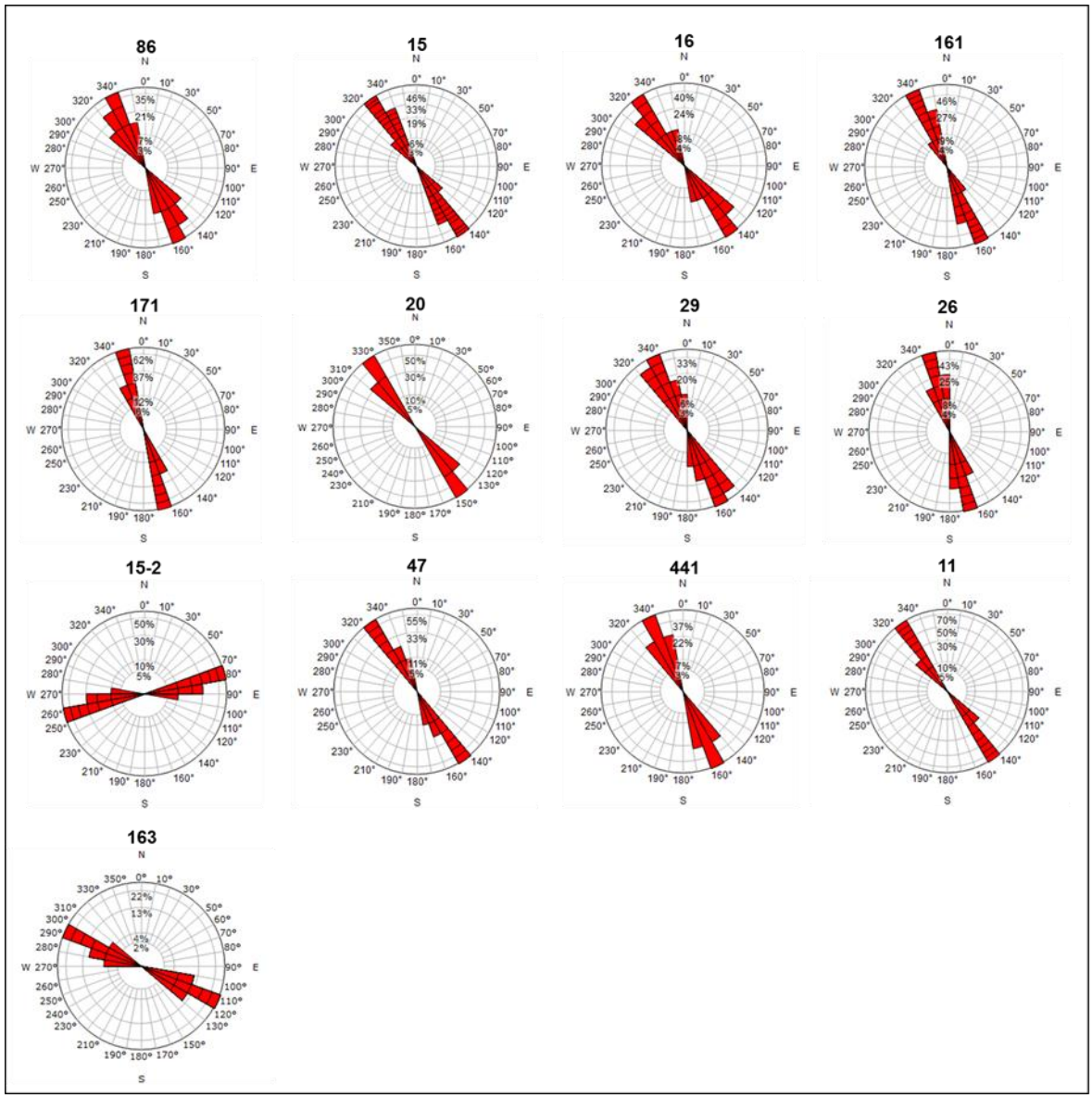

Figure 38: Rose diagrams displaying the S_{hmin} orientations for all wells in the study area. Bin size is 15°.

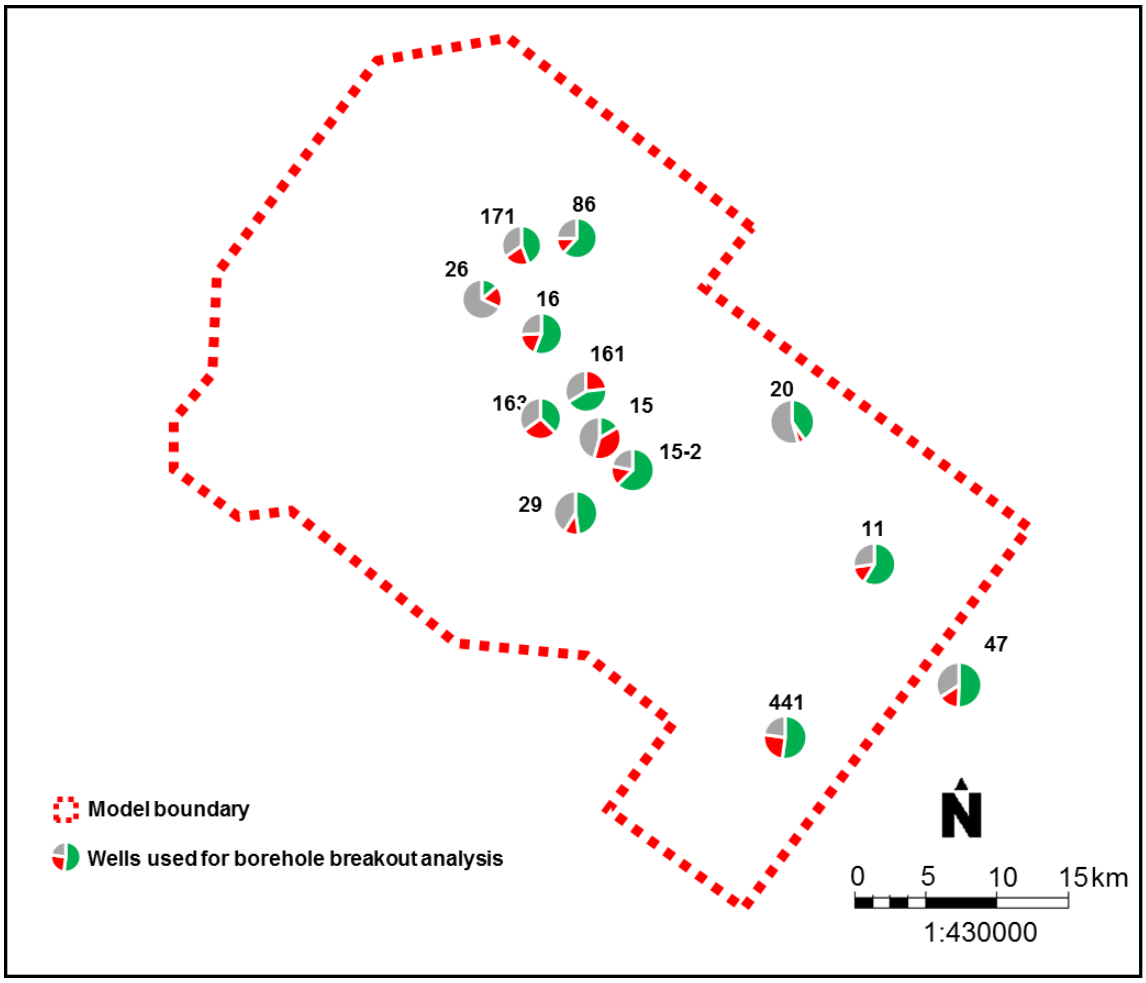

Figure 39: Quality of borehole image data and relative frequency of occurrence of induced deformation observed in all wells. Pie diagrams illustrate the presence of breakouts within the depth interval (green), the absence of breakouts in the borehole (gray), and intervals of poor data quality restricting observations (red).